Losses and Depolarization of Stored Ultracold Neutrons on Diamond-like Carbon

---

Dissertation

zur

Erlangung der naturwissenschaftlichen Doktorwürde

(Dr. sc. nat.)

vorgelegt der

Mathematisch-naturwissenschaftlichen Fakultät

der

Universität Zürich

von

Peter Fierlinger

aus Österreich

Promotionskomitee:

Prof. Dr.	Ulrich Straumann (Vorsitz, Leitung der Dissertation)
Dr.	Reinhold Henneck
Prof. Dr.	Helmut Rauch

Zürich, 2005

Abstract

In this work a novel apparatus for the investigation of wall reflection and depolarization properties of coating materials suitable for ultracold neutron (UCN) storage has been designed and built. The main component of the apparatus is an UCN storage volume consisting of a vertical tube, closed by a magnetic field on the bottom and by gravity on the top. The material to be investigated forms the inner wall of the bottle. This simple geometric shape is favorable for producing high quality coatings. It eliminates mechanical connections and slits that can cause large systematic effects. Closing the bottom of the bottle with a magnetic field means that fully polarized UCN are stored and hence, that for the first time a simultaneous measurement of both the loss probability and the depolarization probability can be made. This is especially interesting for the search on the so-called "anomalous" losses of UCN from material traps. First measurements of diamond-like Carbon (DLC) showed storage times inside the trap of up to 340 s at 70 K, which is a very promising result. For the analysis of the measured data, a Monte Carlo package integrated in the GEANT4 environment was developed, that can handle all physics processes relevant for UCN. The extracted loss coefficient per wall collision of DLC on a polyethylene foil at 70 K becomes $\eta = (7 \pm 1) \cdot 10^{-5}$. In similar experimental conditions, the storage properties of DLC exceed the commonly used material, Beryllium, significantly. The lowest measured depolarization probability per wall collision is $\beta = (7.5 \pm 1) \cdot 10^{-7}$. The parameter η showed a temperature dependency, whereas β was constant. For both parameters no energy dependence could be observed. The data can be qualitatively described in a model using the scattering properties of Hydrogen. These results allow for using the new material DLC in the ultracold neutron source at the Paul Scherrer Institut.

Zusammenfassung

Im Rahmen dieser Arbeit wurde ein Apparat zur Messung von Wandstoss- und Depolarisationseigenschaften von ultrakalten Neutronen (UCN) an Schichten, die zur Neutronenspeicherung verwendet werden, gebaut. Die Hauptkomponente des Apparats ist ein vertikales Rohr, in welchem Neutronen von unten durch ein Magnetfeld und von oben durch Gravitation gespeichert werden. Die zu untersuchende Schicht ist auf die Innenseite des Rohrs aufgebracht. Aus technischen Gründen ist die Geometrie der Speicherflasche möglichst einfach, um systematische Fehler, wie mechanische Verbindungen und Schlitze, zu vermeiden. Das Prinzip der magnetischen Flasche erlaubt es, ein vollständig polarisiertes Ensemble von Neutronen zu speichern. Dadurch ist es erstmals möglich, die Depolarisation gleichzeitig mit den Wandverlusten zu bestimmen. Dies ist insbesondere interessant für die Suche einer Erklärung der sogenannten "anomalen" Verluste gespeicherter Neutronen. Erste Messungen mit dem neuen Speichermaterial "diamantartiger Kohlenstoff" (DLC) zeigten vielversprechende Speicherzeiten von bis zu 340 s bei 70 K. Zur Analyse dieser Daten wurde ein Monte Carlo Programm entwickelt, welches in GEANT4 integriert ist und die für UCN relevanten physikalischen Prozesse beinhaltet. Der resultierende Verlustkoeffizient für DLC auf Polyethylen (PET) bei 70 K beträgt $\eta = (7 \pm 1) \cdot 10^{-5}$. Unter ähnlichen experimentellen Bedinnungen übertrifft DLC damit das am häufigsten verwendete Material Beryllium. Die niedrigste gemessene Depolarisationswahrscheinlichkeit ist $\beta = (7.5 \pm 1) \cdot 10^{-7}$. Für η konnte im Gegensatz zu β eine Temperaturabhängigkeit festgestellt werden. Beide Parameter zeigten keine Energieabhängigkeit. Die Daten können qualitativ mit einem Modell, basierend auf der Streuung an Wasserstoff, beschrieben werden. Aufgrund der vielversprechenden Resultate kann DLC in der neuen UCN Quelle am Paul Scherrer Institut eingesetzt werden.

Contents

Chapter 1

Introduction

The goal of this work was to investigate novel materials used for the storage of ultracold neutrons (UCN) in the context of the new PSI UCN source. The parameters that are relevant to specify such materials are the loss probability per wall collision, the depolarization probability per wall collision and the Fermi potential. The investigation method, the apparatus which was built, measurements and the results are discussed.

1.1 Motivation

The storage of UCN was predicted by Zel'dovich et al. in 1959 [1]. Experimentally this has been realized the first time by Lushikov et al. [2] in 1969 and Groshev et al. [3].

UCN can be trapped in experiments and observed for long times, almost up to the lifetime of the free neutron which is in the order of 900 s. This unique feature makes them an interesting tool for testing fundamental parameters, like the neutron electric dipole moment (nEDM) [4,5], the lifetime of the free neutron (see e.g. ref. [6]), or the correlation coefficients A, a, B and D [7] in the β decay of the free neutron. A basic requirement for experiments which store UCN is to achieve long observation times in a neutron trap with low losses. For many experiments and projects, as for the PSI source and the nEDM at PSI, the trap is made of reflecting material walls. The motivation for this work is to find the optimum solution for such walls and develop test facilities to measure its performance.

1.1.1 Ultracold Neutrons

Neutrons with energies less than the Fermi potential of Beryllium, 258 neV, corresponding to temperatures below 3 mK are usually referred to as UCN. This corresponds to velocities lower than 6.8 m/s. If they hit a material surface, they will interact in a coherent way with an effective potential because of their long wavelength $\lambda > 50$ nm. Based on this, one can define optical properties for such neutrons by using an effective potential, called the Fermi potenial. If such neutrons reach the surface of a material with a high Fermi potential, like Beryllium or diamond (304 neV), they will be reflected under any angle of incidence. They are strongly affected by gravity; the potential energy for a neutron per meter in height is 102.57 neV. The interaction with magnetic fields is defined by the scalar product of the magnetic moment of the neutron with the field vector and is ± 60.31 neV / T.

With this knowledge, one can build traps for neutrons using reflecting surfaces, gravity and magnetic fields. A more comprehensive discussion, based on the common literature in this field, is given in chapter 2.

1.1.2 The Measurement of Neutron Electric Dipole Moment

The discovery of the violation of charge and parity (CP) in the K^0 system [8] implies also a violation of time-reversal (T) symmetry, in such a way that the symmetry of the combination of CPT is conserved [9]. Electric dipole moments (EDM) of fundamental particles are well suited to investigate this in more detail. A fundamental particle will only show an EDM if it is sensitive to interactions, which violate parity (P) and time reversal (T) symmetries [10]: In its rest frame a particle in a non-degenerated state can be described by its angular momentum vector. The absence of additional possible quantum numbers forces the EDM to be only parallel or anti-parallel to this vector. By applying a parity transformation the EDM as a polar vector changes sign, whereas the magnetic moment does not [11].

The experiments at PNPI [12] and ILL [13] used the Ramsey-resonance technique [14] with trapped UCN in order to reach the required sensitivity. This technique is based on a spin precession measurement, where the rotation frequency in a field is given by the Larmor frequency $\omega_L = \mu B/\hbar$. The Larmor frequency is also affected by the value of the EDM, $\mathbf{d}$, as it can be seen in the (simplified) Hamiltonian of the system:

$$H = \pm\mu \cdot \mathbf{B} - \mathbf{d} \cdot \mathbf{E} \tag{1.1}$$

By applying an electric field, H will be changed according to $\mathbf{d}$. The sensitivity is reached by accumulating a phase during the precession for 10^2 s in a very homogeneous magnetic field of $1\,\mu$T and an angular frequency of the spin of 183 Hz. If the same measurement is performed with a reversed electric field, there will be a phase difference after the precession time according to the value of the EDM. A major issue in such an experiment is the stability and homogeneity of the fields, which is an experimental challenge. Up to now all measurements of the EDM of the neutron show values consistent with zero, the currently most precise value is $(-1 \pm 3.6) \cdot 10^{-26}$ e·cm [13]. A non zero EDM is expected by super-symmetric models in the range of 10^{-25} to 10^{-28} e·cm or about 10^{-31} e·cm in the Standard Model of Particle Physics (see e.g. [15], p. 111ff).

The measurement of the nEDM is the major experiment at the PSI UCN source [16]. It has the goal to increase the sensitivity by about two orders of magnitude. A more comprehensive description of this experiment and more detailed information can be taken from ref. [17]. For the measurement procedure one uses polarized UCN which are trapped inside a storage chamber where the $1\,\mu$T magnetic field, the resonance field and the electrical field are applied. During this time the neutrons make a large number of wall collisions, where the spin should be conserved. Spin flip on wall collision typically happens due to any kind of incoherent interaction on the walls. This effect is investigated in our experiment quantitatively.

1.1.3 The UCN Source at PSI

The PSI UCN source (see fig. 1.1) is based on a spallation principle and a solid Deuterium (sD_2) UCN-converter. A detailed description of the source parameters can be found in ref. [16]. The essential elements of the source are a pulsed proton beam with an intensity of $I_p \geq 2$ mA, a low duty cycle of $\sim 1\%$, a heavy-element spallation target and a large moderator system of about $4\,m^3$ of heavy water at room temperature. UCN production is done in a sD_2 converter with a volume of $30\,dm^3$ at low temperatures (~ 6 K). The source is operated in pulsed mode to hold the sD_2 at low temperatures, despite the large power deposition during the pulses.

The number of neutrons that are produced in the spallation process depends on proton energy and target material. In the PSI source about 10 neutrons per proton are produced. These neutrons are moderated to thermal energies in the surrounding heavy water.

In a conventional neutron moderator the neutron velocities are Maxwell distributed. For the case of very low neutron velocities, the density of UCN in an energy range from 0 to V

Material	**Potential [neV]**	$\eta \cdot 10^{-5}$
Be	252	0.027
^{58}Ni	335	8.85
Fe	210	7.51
Cu	168	13.60
Diamond	304	0.013
Al	54	1.86
Fomblin oil	120	0.2
Ti	-48	-

Table 1.1:

Some materials that are typically used in UCN experiments. The values are calculated using only the potential and the absorption cross section.

simplifies to [18]

$$\rho_{UCN} = \frac{2}{3}\frac{\Phi_0}{\alpha}\left(\frac{V}{k_B T_n}\right)^{3/2} \tag{1.2}$$

with $\alpha = (2k_B T_n/m)^{1/2}$. For a neutron temperature $T_n = 300\,\mathrm{K}$, an upper energy limit of V = 250 neV and an incident flux of $10^{15}\,/(\mathrm{s{\cdot}cm^2})$ the density of UCN becomes $10^2/\,\mathrm{cm}^3$.

In a super-thermal source one uses a different method to further increase the density of neutrons: the thermal neutrons are decelerated by inelastic interactions with the scattering medium. In the case of sD_2 at low temperatures ($\sim 6\,\mathrm{K}$), rotational states in the converter are excited. By cooling the converter, less excited states are occupied and therefore the up-scattering probability on such an excitation is lower. The cross section for gaining energy due to up-scattering is

$$\sigma_{up} = \frac{E_{UCN} + \Delta}{E_{UCN}} \cdot e^{-\frac{\Delta}{k_B T}} \cdot \sigma_{down} \tag{1.3}$$

with Δ the excitation energy. The principle of a super-thermal sD_2 source was tested at a reactor [19] and at spallation sources [20–22]. Experiments on the performance of sD_2 have been carried out at PSI, from which the design and operation parameters can be extracted [23, 24].

To store the neutrons that are extracted from the solid Deuterium source, the walls of the guide to the container and inside the container itself are an important issue for the performance of the source. In order to optimize this, the wall reflection properties need to be studied carefully.

1.2 Storage Materials Research

In 1971 first measurements of UCN storage were performed [3]. Soon it was found that the losses from the traps were much higher than expected and many experiments and hypotheses followed. Table 1.1 shows the Fermi potential (eq. 2.5) and the loss coefficient for a few common materials used in the research with ultracold neutrons.

The loss coefficient η is the ratio of the real part of the Fermi potential and the imaginary part, and corresponds roughly to the loss probability per wall collision, as it is shown in chapter 2. The choice for a material used is always a compromise between the Fermi potential and the loss cross section. The isotope ^{58}Ni for example has a very high potential (335 neV),

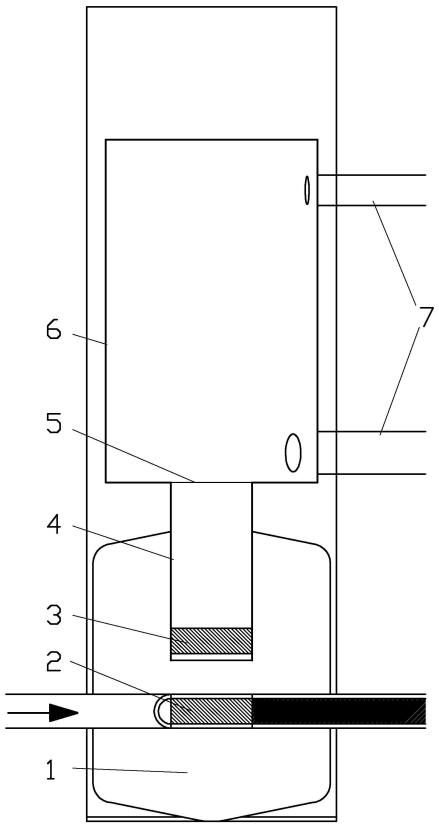

Figure 1.1:

The PSI source. The proton beam is denoted by the arrow. [1] heavy water moderator, [2] Lead spallation target, [3] solid Deuterium UCN converter at 5 K, [4] vertical neutron guide, [5] UCN shutter, closed for storage, open for production, [6] 3 m^3 neutron storage volume with a storage time of ~ 500 s [7] neutron guides to the experiments. The total height of the setup is about 6 m.

but a too large absorption and is also magnetic, whereas Fomblin oil has low losses but also a low potential.

The intensity of UCN source spectra is typically increasing linearly with energy, which makes the height of the potential important to gain density of stored neutrons. Beryllium has a low absorption and a high potential. Nevertheless it is toxic and thus difficult to handle and machine. Diamond would be a much more favorable material. Its Fermi potential exceeds that of Beryllium and is therefore much more suitable than amorphous Carbon. The reason for the difference between Diamond and Carbon is simply the density ("scattering length density"), which depends on the type of orbitals used for the chemical bonds. For amorphous bonds the structure is based on sp^2 orbitals [25], which form covalent bound layers. These layers are only weakly connected via Van der Waals bonds, which are responsible for the mechanical properties. In the case of Diamond the bonds are based on sp^3 orbitals, which are covalent and form a face centered cubic (fcc) structure due to the tetragonal shape of the bonds. There are materials in between these extreme cases, and it is common to define Carbon with high content of sp^3 as DLC. Diamon-like Carbon has many applications and it is possible to produce it quite cost-effectively with surfaces in the order of square-meters.

The values for the loss cross section consists of the nuclear absorption cross section and a contribution from temperature dependent up-scattering, based on the total scattering cross section. One can define an energy independent parameter to describe the loss probability per wall collision for each temperature (eq. 2.18). This value is a factor of 50 to 100 smaller in theory than experimentally observed[1]. This phenomenon is commonly referred to as anomalous losses, and there are several approaches to explain this problem. When the theoretical values of the loss coefficient η are discussed, this is usually done for low temperatures.

As mentioned above, already in the beginning of the research on neutron storage it was found that the measured losses exceed the theoretical expectations. A list of hypotheses is given in refs. [28, 29] and ref. [30] p. 175ff. Some effects proposed for the explanation of the losses on solid surfaces are

(i) acoustic vibrations of the surface: there was no experimental hint for such an effect and an upper limit is given in ref. [30] with $7 \cdot 10^{-11}$ eV per wall collision.

(ii) surface roughness and pores in the surface: the upper limit of roughness can be estimated with an increase of the loss probability of about 25 % [18].

(iii) inelastic scattering: temperature dependent inelastic scattering is caused by phonon de-excitation. This effect is a known contribution to the losses, it is discussed in chapter 10.

(iv) scattering on impurities or surface films: this hypothesis remains unsolved because of the large amount of impurities needed and the expected temperature dependence which was not observed experimentally. However, if one considers contamination with Hydrogen it is possible to create scenarios to explain the observed values [31].

(v) loosely bound clusters of atoms: clusters with a size in the order of 60 Å can vibrate with frequencies up to 10^{10} Hz and transfer energy to the neutron [30].

From the variety of experiments that were performed to investigate this loss-problem in more detail, we pick out a few milestones from the last thirty years.

In an experiment with thin Copper walls, surrounded by ^{3}He-detectors it could be found that the neutrons were inelastically up-scattered and could therefore escape [32], the energy was found to be in the range between 1-10 meV.

The investigations continued with Beryllium as a wall material [33], which resulted in much better storage properties, but nevertheless the deviations from theoretical predictions remain unclear.

An experiment by Ageron et al. [31] found a temperature dependence of the loss probability, which indicates that Hydrogen impurities near the surface are responsible for the increased losses. This result was questioned later by ref. [30]. The concentration of Hydrogen on the surfaces was measured by e.g. refs. [34, 35]. A review of research on this topic is given by ref. [36].

The best values for the loss probability of Beryllium that was measured is about $3 \cdot 10^{-5}$ per wall collision [37] at $T < 30$ K. Recently further investigations of the so-called low energy heating effect have been done by refs. [38, 39]. An effect of 10^{-5} to 10^{-8} eV energy change for such events was observed [40], and the explanations reach from surface states [38], i.e. neutrons could be temporarily adhered on material surfaces, to the interaction with nano particles [41] on the surfaces.

It seems obvious that one can observe spin flips during neutron storage if one considers Hydrogen, where neutrons scatter incoherently [42]: The cross section for spin flip scattering is proportional to the incoherent cross section, it is assumed to be $2/3 \times 80$ barn here. The up-scattering cross sections $\sigma_{up} = (4-7)$ barn $\cdot 2200/v$ (m/s) depends on the chemical bonds of the Hydrogen atoms on the surface. From this a ratio of depolarization to up-scattering of

[1] An exception is Fomblin oil at low temperatures, which has a loss coefficient of $2 \cdot 10^{-6}$ per wall collision and is only about a factor of 10 above theoretical predictions [26, 27].

about $(1.5 - 3) \cdot 10^{-2}$ is expected. Other reasons for depolarization are the interaction of the neutron with paramagnetic atoms or other magnetic domains on the surfaces.

In this work we focus on DLC surfaces, which combine high Fermi potentials with low losses and low depolarization. The Fermi potentials of different DLC samples from the Fraunhofer Institut Institut für Werkstoffkunde und Strahlführung IWS in Dresden and from the Virginia Polytechnic Institute were measured using neutron reflectometry [43] at SINQ (see sec. 9.5). The results were promising and we decided to investigate the storage properties of such materials further. First experience with high density DLC coated surfaces already existed [44–46], which gave an idea of the storage properties of these materials. An apparatus to produce such coatings is currently being built at PSI [47].

The most important test on the quality of a coating is the measurement of storage properties using UCN. The two parameters that we are interested in are the loss probability per wall collision and the depolarization probability per wall reflection. Therefore we decided to build an experiment to determine the values for both parameters in the same experiment at the same time.

In the following the physics involved in this experiment is described (chapter 2). For the simulation a Monte Carlo package (chapter 3) was developed. The major part of this work will be the description of this experiment (chapter 4), the measurements (chapter 5) and the analysis of the measured data (chapters 6-8). Tests on various systematic effects (chapter 9) and finally a discussion of the results (chapter 10) are shown.

Chapter 2

UCN Physics

In this chapter the relevant interactions of neutrons with materials and fields are discussed. As done usually in books about neutron scattering, e.g. [18, 30, 48, 49], we start first with the situation of a single scattering center, then we go to many scatterers and derive from this the general case taking into account also thermal vibrations of nuclei. The second section gives an outline of the interaction of the neutron with fields.

2.1 Interaction with Materials

2.1.1 Scattering from a Single Nucleus

Ultracold neutron scattering on a single scattering center can be described as an incident wave function and a reflected part of the wave with a parameter describing the dependence on angle and incident momentum.

$$\psi_{i,f} = e^{ikr\cos\theta} + f(\theta, k)\frac{e^{ikr}}{r} \tag{2.1}$$

The parameter f is the scattering amplitude. The probability of scattering into a solid angle element is

$$dP = v|f(\theta, k)|^2 d\Omega \tag{2.2}$$

with v the incident neutron velocity, which is equivalent to the quantum mechanical current density. From this we get

$$d\sigma = |f(\theta, k)|^2 d\Omega \tag{2.3}$$

The parameter f can be simplified for UCN since the particle wavelength λ is significantly larger than the range r_0 of the strong interaction potential responsible for scattering. Following [50] the energy dependence can also be neglected and it can be written as a convention

$$f(\theta, k) = -a \tag{2.4}$$

where a is called the scattering length, which does not take into account the interaction with spins different from zero.

Fermi Potential

Scattering of neutrons on nuclei is usually approximated using the first Born approximation. This approach is not valid here because the energy of the nuclear potential is much higher than the kinetic energy of an UCN. Nevertheless, by using a potential that is valid for the low energy limit in the Born approximation, which is usually referred to as Fermi potential [51,48],

$$V_F = \frac{2\pi\hbar^2 a}{m}\delta(\mathbf{r} - R_i) \tag{2.5}$$

one obtains proper results for scattering for an individual scattering center at the position R_i. By averaging over many scattering centers, the density of scattering centers replaces the δ function and the scattering length is replaced by the bound coherent scattering length. This leads to the next section.

2.1.2 Neutron Scattering from a Group of Scattering Centers

When many scattering centers are involved coherent effects appear. Sears [48] defines absolute coherence as a wave interfering with itself while it undergoes a reflection, and this is therefore also elastic. Relative coherence is the case for waves scattered from different atoms interfering with each other, but not necessarily with the incident wave. This is what we will use as a definition of coherence. The interaction of the neutron wave with a single scattering center causes a loss of the phase correlation between the incident and the outgoing wave and is therefore called incoherent.

This allows for a division into a coherent and incoherent scattering cross section [50]:

$$\sigma_{coh} \sim \left(\sum_i a_i \right)^2 \sim N^2 \sigma_i \tag{2.6}$$

It means that the amplitude of the resulting wave is the sum of all amplitudes scattered from different centers. For incoherent scattering

$$\sigma_{inc} \sim \left(\sum_i a_i^2 \right) \sim N \sigma_i \tag{2.7}$$

the cross section is just the sum of the individual scattering cross sections. This kind of scattering occurs because of different scattering lengths of the target atoms and by spin incoherence.

The total scattering cross section can be split up into four terms, the incoherent elastic cross section, the incoherent inelastic cross section, the coherent elastic cross section and the coherent inelastic cross section.

Neutron Optical Properties

Ultracold neutrons have wavelengths much larger than typical distances of atoms, which can lead to interference effects caused by the scattering on many scattering centers. If the Fermi potential is used to describe such an averaged interaction, the scattering length a_B used for the calculation of this potential is the bound coherent scattering length, represented by

$$a_B = \frac{m}{\mu} a \tag{2.8}$$

with the reduced mass μ. This is used for the description of neutron optical phenomena. The averaged potential is

$$U = V - iW = \frac{2\pi\hbar^2}{m} N (a_B - i a_{Bi}) \tag{2.9}$$

where N is the density of scatterers and a_{Bi} the imaginary part of the scattering length. Spin interaction here is taken into account only via the (phenomenological) magnetic scattering length. The interaction with a material boundary can result in reflection or transmission with an index of refraction smaller than one. The relevant parameter is the normal component of the neutron velocity incident on the boundary relative to the critical velocity $v_c = \sqrt{2V/m}$. This process can be shown as a one dimensional quantum mechanical wave incident on a

potential step V with a kinetic energy E perpendicular to the step smaller than V. The wave outside the potential barrier is

$$\psi_{out} = e^{i\mathbf{k}x} + Re^{-i\mathbf{k}x} \tag{2.10}$$

with R the amplitude of the reflected wave. The energy incident on the potential is

$$E = \frac{\hbar^2\mathbf{k}^2}{2m}. \tag{2.11}$$

If this is larger than V, the wave will enter the material and only the perpendicular component E will be changed by the potential:

$$\frac{\hbar^2\mathbf{k}'^2}{2m} = E - V \tag{2.12}$$

with $\mathbf{k}'$ the wave number and

$$\psi_{in} = Te^{i\mathbf{k}'x} \tag{2.13}$$

the wave inside the barrier. T is the amplitude of the transmitted wave. In the three dimensional case we are interested in the perpendicular components to the surface. Assuming that the wave-function at the boundary position is smooth the reflection coefficient becomes

$$R = \frac{|\mathbf{k} - \mathbf{k}'|}{|\mathbf{k} + \mathbf{k}'|} = \frac{\sqrt{E_\perp} - \sqrt{E_\perp - V}}{\sqrt{E_\perp} + \sqrt{E_\perp - V}} \tag{2.14}$$

The reflection coefficient is $|R|^2 < 1$ for $E_\perp > V$, whereas for $E_\perp < V$ the reflection probability is 1. For the transmitted wave one gets an exponential decay, which corresponds to the entering depth inside the material in the order of 100 Å. The penetration depth

$$d = \lambda_c/2\pi \tag{2.15}$$

with an assumed wavelength λ_c is in the order of 100 to 1000 Å. This gives us a rough estimate of the number of scatterers, which the neutron can interact with during scattering, in the order of 10^3.

The imaginary part of the scattering length causes a complex (opaque) optical potential (eq. 2.9), which is used for the solution of the Schrödinger equation, resulting in an expression for the absorption in materials:

$$1/\tau_{abs} = \frac{\hbar}{2}\sum_i N_i\sigma_l^{(i)}v \tag{2.16}$$

The cross section σ_l contains absorption and inelastic scattering, both dependent on $1/v'$, with v' the velocity inside the material. By comparing eq. 2.16 and eq. 2.9 we also see the application of the optical theorem.

$$a_{Bi} = \frac{\sigma_l k}{4\pi} \tag{2.17}$$

The loss cross section combined with the fact that the wave enters the material on reflection is also the reason for a loss probability on reflection. For storage experiments it is common to define the parameter

$$\eta = \frac{W}{V} = \frac{\sigma_l k}{4\pi a_B} \tag{2.18}$$

The reflectivity R (eq. 2.14) becomes then

$$|R|^2 = 1 - \mu(E, \theta) \tag{2.19}$$

with the energy dependent loss parameter

$$\mu(E,\theta) = 2\eta \left(\frac{E\cos^2\theta}{V - E\cos^2\theta} \right)^{1/2}. \tag{2.20}$$

For the case of stored UCN this equation can be integrated over all angles of incidence, according to ref. [18], p. 25.

$$\overline{\mu}(E) = 2\eta \left[\frac{V}{E} \sin^{-1}\left(\frac{E}{V}\right)^{1/2} - \left(\frac{E}{V} - 1\right)^{1/2} \right] \tag{2.21}$$

This parameter $\overline{\mu}$ is the commonly used loss probability per bounce.

2.1.3 Inelastic Scattering

The inelastic scattering cross section is calculated based on the formalism derived from ref. [52]. A detailed discussion of this problem is shown in e.g. ref. [18], Appendix 3. The Van Hove scattering functions S are

$$\begin{aligned} \left(\tfrac{d^2\sigma}{d\Omega d\omega}\right)_{coh} &= \tfrac{\hbar}{N}\tfrac{k_f}{k_i} \textstyle\sum_{n_i,n_f} P_{n_i} a_{coh}^2 \ \left| \sum_i a_i \langle n_f \left| e^{i\mathbf{Q}\cdot\mathbf{R_i}} \right| n_i \rangle \right|^2 \delta(E_f - E_i - \hbar\omega) \\ &\equiv a_{coh}^2 \frac{k_f}{k_i} S_{coh}(\mathbf{Q},\omega) \end{aligned} \tag{2.22}$$

and

$$\begin{aligned} \left(\tfrac{d^2\sigma}{d\Omega d\omega}\right)_{inc} &= \tfrac{\hbar}{N}\tfrac{k_f}{k_i} a_{inc}^2 \textstyle\sum_{n_i,n_f} P_{n_i} \left| \sum_i a_i \langle n_f \left| e^{i\mathbf{Q}\cdot\mathbf{R_i}} \right| n_i \rangle \right|^2 \delta(E_f - E_i - \hbar\omega) \\ &\equiv a_{inc}^2 \frac{k_f}{k_i} S_{inc}(\mathbf{Q},\omega). \end{aligned} \tag{2.23}$$

For ultracold neutrons no coherent scattering in the sense of Bragg-scattering can occur. Nevertheless there is still coherent interaction. The description of scattering is treated in the so called incoherent approximation. In this approximation it is assumed that the scattering cross section consists of a coherent and incoherent part and is therefore

$$\sigma_{el} = \sigma_{inc} + \sigma_{coh}. \tag{2.24}$$

Following ref. [30], p. 174, the scattering formalism from sec. 2.1.3 can be written as

$$\sigma_{ie} = \frac{\sigma_{el}}{M}\frac{p_f}{k_i} \tag{2.25}$$

where M is the mass ratio of the neutron and the atom, p is the momentum of the scattered neutron. The momentum of the scattered state is

$$p_f = \int_0^{\omega_D} d\omega \sqrt{\omega} g(\omega) n(\omega,T) e^{-W(\omega,T)} \tag{2.26}$$

The density of states $g(\omega)$ is approximated by the Debye spectrum

$$g(\omega) = \frac{3\omega^2}{\omega_D^3} \tag{2.27}$$

with $\omega_D = \Theta_D \hbar / k_B$ the Debye frequency. The parameter Θ_D is the Debye temperature. The Planck distribution for bosons is

$$n(\omega,T) = \left(e^{\hbar\omega/k_B T} - 1 \right)^{-1}. \tag{2.28}$$

The Debye-Waller factor $W(w,T)$ describes the displacement of the atoms due to their thermal oscillations.

$$W(\omega,T) = \hbar\omega \int_0^{\Theta_D k_B} dE \frac{g(E)}{4ME} coth\left(\frac{E}{2k_bT}\right) \tag{2.29}$$

with the Debye spectrum $g(E)$ in terms of energy and ω the energy transfer used for the integration of eq. 2.26.

2.2 Interaction with Fields

2.2.1 Gravity

As all matter, neutrons interact with the earth's gravitational field: The potential is

$$V_g = m_n g h \tag{2.30}$$

with the potential $V_g = 102.57\,\text{neV}$ corresponding to 1 m height, which is quite significant compared to typical UCN kinetic energies. The mass of the neutron is $m_n = 1.67492728(29) \cdot 10^{-27}\,\text{kg}$ [53]. To refer to the Fermi potential of Beryllium, the maximum height of a material bottle made of Beryllium is then $\sim 2.5\,\text{m}$.

2.2.2 Magnetic Interaction

The motion of a neutron in a magnetic field is described by the two coupled equations [54]:

$$\frac{d^2\mathbf{r}}{dt^2} = -\frac{\mu_n}{m_n}\nabla(\sigma_\mathbf{n} \cdot \mathbf{B}) + g \tag{2.31}$$

with the magnetic moment of the neutron $\mu_n = -60.307694\,\text{neV/T}$ [53], and

$$\frac{d\sigma_\mathbf{n}}{dt} = \gamma\sigma_\mathbf{n} \times \mathbf{B}. \tag{2.32}$$

The force on the neutron depends on the field gradient and the projection of the spinor vector σ_n on the magnetic field. In this general description also gravity is included by the coefficient g. The treatment of the spin can be done using a classical three dimensional polarization vector $\mathbf{P}$ [55], consisting of the expectation values of the spinor matrices.

$$\langle\sigma_i\rangle = \langle\chi|\sigma_i|\chi\rangle = P_i \tag{2.33}$$

where χ is the spinor wave function, and σ_i the spinor matrices. In a field, the quantization axis is parallel the field lines and usually called z. Relative to this quantization axis only two orthonormal states are possible

$$|\chi\rangle = a|\uparrow\rangle + b|\downarrow\rangle \tag{2.34}$$

with the probability amplitudes

$$|a|^2 + |b|^2 = 1 \tag{2.35}$$

Then one can write the components of the polarization vector as linear combinations of a and b.

$$\begin{aligned} P_x &= a \cdot b + b \cdot a \\ P_y &= i(a \cdot b - b \cdot a) \\ P_z &= |a|^2 - |b|^2 \end{aligned} \tag{2.36}$$

By convention we call the angle between P and the quantization axis θ, and ϕ the angle on the xy-plane. The relation between these angles and the parameters a and b is:

$$\begin{aligned} a &= \cos\frac{\theta}{2} \\ b &= e^{i\phi}\sin\frac{\theta}{2}. \end{aligned} \tag{2.37}$$

In the case of UCN we are typically in the so-called adiabatic limit (see ref. [30] p. 234ff), where the Larmor-precession is much faster than the time dependence of the field seen by the neutron moving through the inhomogeneous field.

$$\omega = \frac{|\mu_{\mathbf{n}} \cdot \mathbf{B}(\mathbf{r})|}{\hbar} \tag{2.38}$$

No precession of the polarization vector can be observed in this case as the polarization is oriented parallel (or anti-parallel) to the magnetic field. Since the particle is neutral and the interaction is via its magnetic moment the equation of motion is similar to that used for gravity. The force acting on the neutrons is then given by ref. [18]:

$$\mathbf{F} = -\nabla \mathbf{V_m} = -\nabla|\mu_{\mathbf{n}} \cdot \mathbf{B}(\mathbf{r})| = \pm\mu_{\mathbf{n}} \cdot \nabla\mathbf{B}(\mathbf{r}) \tag{2.39}$$

A field with an absolute value of 1 T corresponds to a potential of 60.3 neV. The equation of motion can be simplified to

$$\frac{d^2\mathbf{r}}{dt^2} = \pm\frac{\mu_{\mathbf{n}}}{m_{\mathbf{N}}}\nabla|\mathbf{B}| + g \tag{2.40}$$

Chapter 3

Monte Carlo Simulations

For the transport and storage of UCN, accurate knowledge of the particle tracks may be required. The tracks of the particles are typically not easily accessible in such experiments and have to be calculated.

An interesting parameter, especially in our experiment is the flux of stored UCN on the surface of the storage volume, depending on neutron energy and height. If we assume the neutrons in a quasi statistical equilibrium similar to an ideal gas, the volume to be spherical, and the particles can reach every position of the surface with the same probability, i.e. neglecting gravity and the influence of magnetic fields, we can apply a kinetic theory approach [18]. The flux on the surface is then

$$\nu(dS) = \frac{1}{4} v \rho dS \tag{3.1}$$

where S represents a surface element, v the mean velocity and ρ the UCN density (see e.g. ref. [56]). This simple situation is an approximation as there will never be equilibrium due to the limited storage times of the neutrons and the effect of gravity and other fields, which can be large.

3.1 GEANT4

We decided to use Monte Carlo simulations to study the behaviour of the particles of interest. In the following, the Monte Carlo package used for the simulation of the experiment is discussed. A principle assumption is that we can calculate trajectories of individual particles without any influence of the particles on each other. We decided to use a standard code from the particle physics field, which appeared well suitable for our problem. It is called GEANT4 [57] and we adapted it to the simulation of UCN experiments. GEANT4 is a versatile, widely used toolkit for the simulation of the passage of particles through matter. Its applications include high energy and nuclear physics experiments, medical, accelerator and space physics studies. As such, it can handle many physically possible processes, including decay and particle production. The latter property is particularly interesting since it allows to combine the trajectory tracking of both, the "parent" UCN as well as the "daughter" decay products, e.g. in neutron decay experiments. It therefore appeared very tempting to exploit the GEANT4 advantages - versatility, completeness, easy geometry implementation and professional maintenance - and extend it to the case of UCN [58]. The code version used as a basis for the changes is GEANT4.4.6.p01.

The simulation of the experiment described in this work uses tracking of a UCN in a combined gravitational and magnetic field, which can be switched on and off with time, and different material boundary interactions. The modifications of the code concerning the relevant physics involved in our experiment are described and testcases with other programs are shown

to prove the results. Examples for the transmission through a neutron guide and for the storage inside a material bottle are shown.

3.2 GEANT4 Modifications

The additions to the code concern mainly the following areas: sec. 3.2.1, new forces (gravity and time-varying, inhomogeneous magnetic fields for UCN), sec. 3.2.3, new processes (UCN-specific reflection and scattering) and sec. 3.2.4, new geometries (shutters).

3.2.1 Forces

Forces can be included easily, since GEANT4 makes provision for new forces through the specification of potentials. Although neutrons are of course treated in the standard GEANT4 package we have nevertheless introduced UCN as a new type of particle, being the only species to be affected by gravity. Gravity is implemented in analogy to a constant homogeneous electric field. The magnetic interaction is implemented for the adiabatic case for even strongly inhomogeneous, time-varying magnetic fields. The force acting on the neutron can be written as $\mathbf{F} = \pm\mu \cdot \nabla|\mathbf{B}(\mathbf{r})|$ [59]. Arbitrary fields can be user defined and entered using functions for the calculation of the field strength in space and time. This allows field gradients to change arbitrarily and can cause inaccuracies if the field changes strongly within one step. If one uses field coordinates as an input, the interpolation between the field points is done linearly in space and time. The propagation of a neutron in an arbitrary magnetic field taking into account its polarization vector causes increased calculation times and is done inside a GEANT4-process by integrating the Bloch equation, which can be used on demand.

3.2.2 Tracking of the Spin Precession in Fields

As mentioned in sec. 2.2, we use the adiabatic assumption to calculate the trajectory of the neutron in the combined gravitational and magnetic field.

During the storage of neutrons in our experiment the polarization can also change due to low field transitions, not only due to wall collisions. Strictly speaking this is not depolarization but only re-orientation of the spin. This is the case for regions with a strong gradient and a low strength of the magnetic field, as here the adiabatic assumption is no longer valid. On demand, a process to track the spin can be applied to follow the polarization vector. The spin is here described similarly to a classical dipole precessing in a field (see sec. 2.2). The probabilities of an eigenvalue of the spin parallel or anti-parallel to the chosen quantization axis are given by the angle θ between the polarization vector and the field line. The development of this vector with time can be described using the Bloch-equation

$$\frac{\mathbf{dP}}{dt} = -\gamma \mathbf{P} \times \mathbf{B} \tag{3.2}$$

with the polarization vector $\mathbf{P}$. This equation is integrated using a Runge Kutta fourth order (RK4) algorithm (ref. [60], p. 710) with adaptive step size, performed at the end of each geometrical step along the trajectory of the particle. The integral of the field along the path is done according to ref. [61] using a RK4 algorithm. This algorithm is slightly changed to angular coordinates instead of Cartesian coordinates. The adaptive step size is determined in between the boundary of the geometrically limited steps given from the trajectory calculation. This allows for simulating e.g. the behaviour in a Ramsey resonance apparatus, see e.g. ref. [14]. However this is not including the influence of the classically changing spin vector on the trajectory.

3.2.3 Processes

Following the Fermi potential approach, material interactions can be described in an averaged form. Coherent and incoherent scattering effects can be observed. The main implemented processes can in principle be separated into material boundary processes (reflection) and bulk material processes (scattering and absorption).

We first discuss reflection. Whether an UCN is reflected from the material depends on the neutron energy E, its angle of incidence θ and the Fermi potential V. The latter can be calculated from the chemical composition of the material or - which is more efficient - be implemented as a parameter by the user. From this the critical velocity v_c of the material is calculated (corresponding to the maximum velocity for total reflection at normal incidence) and compared to the normal velocity component v_n. If $v_n < v_c$ the neutron will be reflected and different reflection models can be applied. We have implemented specular and diffuse reflection and the user can specify the probability for either process to happen. For diffuse reflection we employ the usual cosine distribution for the reflected intensity, e.g. ref. [18], p. 101. The fact that even for total reflection there is a tiny probability for the neutron to get "lost" is implemented via the material dependent loss factor η. The latter is connected to the loss probability per wall collision μ which is a function of E, θ and V and is here written in terms of the normal component of the velocity on the surface v_n:

$$\mu(v_n) = 2 \cdot \eta \left(\frac{v_n/v_c}{\sqrt{1-(v_n/v_c)^2}} \right) \tag{3.3}$$

(see e.g. ref. [18], p. 25ff). Other parameters useful for the simulation of storage experiments like e.g. the probability for "spin flip per wall reflection" β (independent of E, θ and V) are implemented. Of course, β could be easily made energy and angle dependent. The loss and spin flip probability parameters are material properties and have to be implemented explicitly since theoretical approaches for the description of these phenomena could not be verified experimentally so far.

If the normal velocity component is larger than v_c, the particle enters the material and can be elastically scattered, absorbed or up-scattered, i.e. inelastic scattering to energies above the UCN regime. The absorption is calculated in the usual way via an exponential attenuation law with the absorption cross sections proportional to $1/v'$. Here v' is the velocity inside the material, where the normal component of the velocity vector is changed due to the index of refraction. Forces acting on a particle inside a material change its velocity and direction, which affects e.g. the mean free path inside the material. Thermal up-scattering is neglected here (but can be easily implemented), since for storage in material bottles the observed losses are not consistent with theoretical predictions [18]. Nevertheless user defined scattering laws can be implemented. Elastic scattering is treated by calculating a mean free path for the particle using scattering cross sections. The corresponding angular distributions can be user defined. The index of refraction in the material is calculated by changing the component of the velocity normal to the surface using energy conservation (see ref. [18], p. 24).

3.2.4 Geometries

The new implemented features are geometries that have time varying properties. An example is the definition of shutters, which are volumes that can change their material composition, as specified in a macro file. For instance, an arbitrary volume made of massive Beryllium can change its properties to "vacuum" and in this way simulate a mechanical UCN valve, a shutter or a chopper.

3.3 Code Tests

3.3.1 Comparison with Analytical Trajectory Calculations

A stringent test for the accuracy of the trajectory calculation is the comparison with analytical calculations. Within GEANT4, a particle is propagated inside a field by integrating the equation of motion using a stepping algorithm. The advantage of such a method is that many problems that are difficult to integrate analytically can be solved much easier and it is therefore much more versatile. Examples are the propagation of a particle in a complex geometry, in a complicated field, or the proper behaviour inside a material when forces are taken into account. The drawback for the versatility is a longer calculation time compared to a fully analytical trajectory calculation. Of the various algorithms provided in GEANT4, Runge Kutta 4 turned out to be reasonably fast and stable. In order to optimize the tracking accuracy inside complicated geometries we use the "miss-distance" parameter Δ_{miss}, which is one of the standard accuracy parameters in the GEANT4 package. The trajectory of the particle is broken up into short linear segments with the length of the segments constrained by Δ_{miss}, which is the maximum allowed deviation of the linear track segment from the "real" trajectory. The "real" trajectory is estimated using the convergence of the stepping algorithm. For a given Δ_{miss} the linear path segment becomes shorter if the curvature of the trajectory is strong. A smaller Δ_{miss} increases the accuracy, but leads to longer calculation times. For the simulation of our experiment an accuracy parameter inside the magnetic field of $1 \cdot 10^{-7}$ mm deviation per meter flight path was chosen. The maximum step length in the gravitational field is in the order of 10 mm, which is mainly limited by the geometry of the experimental setup.

In complicated geometries the step size can be adapted by the user in specified volumes, such as thin foils, without reducing the step size for the whole application.

3.3.2 Tests against Conventional Monte Carlo Codes

Here we discuss the comparison with conventional Monte Carlo codes. Since there is no widely-used standard conventional code we compare with the code of one member of our collaboration (A. Fomin) which has been used in many applications. This code starts from an initial distribution of neutrons and calculates the track of each particle analytically until it reaches a material boundary, where the geometries are limited to regular shaped volumes. At each wall collision the loss and reflection probability is calculated, resulting in a new direction to calculate the trajectory until the next boundary is reached. The surfaces are limited to flat, cylindrical and ellipsoidal. The neutron decays with a lifetime of 888 s (for this comparison). For the tests we used the same initial distributions, diffusion- and loss parameters.

- In the first test case we compare the velocity spectrum transformation through a simple guide system with 140 x 140 mm^2 cross section. It consists of a 2 m straight, horizontal section, followed by a 90° bend (1 m radius) and a 2 m straight, vertical section. The relevant parameters are: $v_c = 7.8$ m/s with no loss for $v_n \leq v_c$ and total loss for $v_n > v_c$, 0.7 % diffuse reflection probability, incident velocity components v_{axial} are linearly distributed from 0 to 15 m/s and v_{radial} has a constant probability between 0 and 7.8 m/s normal to the guide wall at the entrance. The results are shown in fig. 3.1.

  The velocity spectrum transformation was defined as the number of UCN in a given total velocity bin (e.g. at 5 m/s) after transmission through the system divided by the number of UCN in the same total velocity bin (i.e. again at 5 m/s) at start. Within statistics the agreement between both predictions is good.

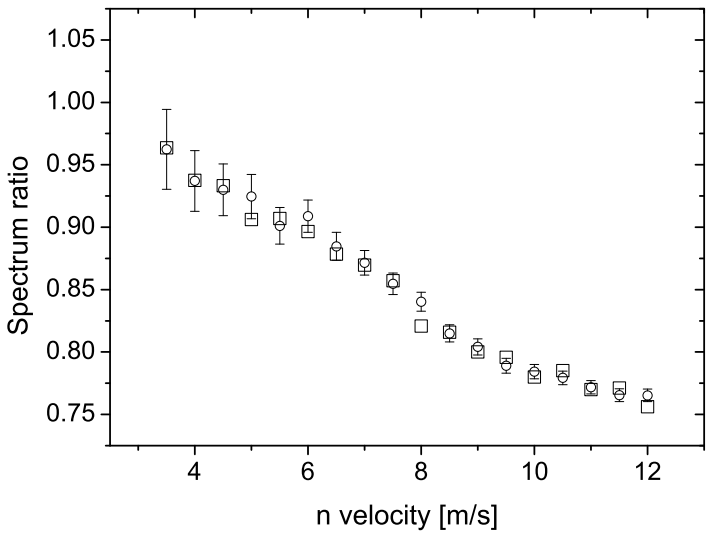

Figure 3.1:

Transmission through a neutron guide. Comparison of two guide "transmission" calculations. The total velocity spectrum transformation through the guide is described in the text, calculated by GEANT4 (open circles) and by the code of A. Fomin (squares).

- In the second example UCN are stored inside a cylindrical Beryllium bottle of radius 250 mm and height 2700 mm (v_c = 6.8 m/s). The neutrons are produced uniformly at the bottom within a circular area with 200 mm radius around the center. The UCN are mono-energetic (131 neV, corresponding to v = 5 m/s or a height of 1.29 m) and are started with a certain angular distribution.

  We consider two cases with the wall reflections either being completely specular or 90 % diffuse and 10 % specular. In fig. 3.2 the distribution of wall collisions along the vertical direction is plotted for the two cases. Each curve involves the tracking of 10^5 neutrons. The agreement between both calculations is perfect. Physically, the two curves represent two extreme cases: with 90 % diffuse reflection probability the directions of the neutrons get immediately randomized. Under these conditions the neutrons can be adequately described by kinetic gas theory with inclusion of gravity and the wall collision frequency is linearly decreasing with height [18]. With purely specular reflection on the other hand, the UCN "memorize" the initial angular distribution to some extent and the wall collision frequency depends on the details of the geometry and of the initial angular distribution. When the wall collision frequency is large as it is the case for our simulation, the diffusion is not relevant for the storage calculation, as long it is non-zero, which is the case in any realistic situation.

The approach of describing wall reflection with this simplified model is chosen due to the lack of knowledge of the surface morphology. Especially for the case of storage calculations the sensitivity on the diffuse scattering probability is low and does not influence the calculations. For statistical processes and time averaged or probabilistic quantities like storage time, wall collision frequency, spin flip probability per wall collision etc. this approach is suitable. In the case of a guide tube for transporting neutrons different models are discussed in literature

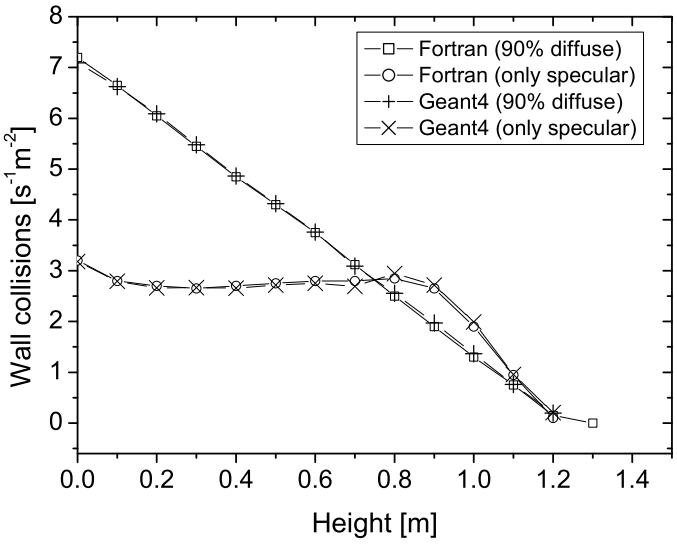

Figure 3.2:

Wall collision distribution. Wall collision frequency as a function of height, calculated with GEANT4 and with the code of A. Fomin. Two different reflection conditions were considered: specular reflections only (open circles and x-crosses)and 90 % diffuse and 10 % specular (open squares and +). For further detail see text.

based on diffusion models and Monte Carlo, as shown in ref. [30], p. 102 ff. In our case, this is only treated by the method of tracking specularly and diffusely scattered neutrons. Using this method one has to tune the parameters of the simulation to measured data [62], which gives satisfying results for most applications.

Chapter 4

Surface Investigation Experiment

The experiment for the measurement of the loss- and depolarization probability per wall collision [63, 64] on DLC and Be surfaces was set up at the beamline PF2-DIFF at the PF2 ultracold neutron source. A short overview of the neutron source is given and the experiment is described.

4.1 The Neutron Source at ILL

The neutron source is a 58 MW research reactor with a cold source [65] for the production of cold neutrons. The cold neutrons are extracted vertically and further decelerated in a neutron turbine [66]. A schematic cross section through the reactor is shown in fig. 4.1.

The fuel element is placed in the middle of the reactor. The neutron production is controlled by a Lithium rod from below. Neutron moderation is done by D_2O, which surrounds the fuel element. Thermal neutrons are extracted by neutron guides from here. Inside this heavy water tank two cold sources are placed. The vertical cold source, which is used for the production of UCN, consists of 20 dm^3 of liquid D_2. The cooling power needed during operation is 6 kW, corresponding to the γ-heating at this position. The source volume is made from Aluminium and has a safety window on the top. A vertical neutron guide is connected to this window. Cold neutrons are extracted via this 12.8 m long bent neutron guide, which is leading the neutrons vertically through the D_2O tank through the H_2O shielding. The curvature of the guide helps to remove faster neutrons which are not totally reflected from the walls of the Ni coated glass plates covering the inside of the guide. The vertical extraction leads to a deceleration of the neutrons due to gravity.

Neutrons that pass through the guide enter the turbine and are Doppler-shifted to the ultracold neutron range. The turbine consists of a 1700 mm diameter wheel with 690 bent and polished Copper mirrors. The mirrors are rotating in the flight direction with a velocity of 25 m/s, which causes a velocity shift. Four beamlines are connected to this rotating wheel. One beamline has a continuous beam ("TES"), whereas the other three beamlines ("MAM", "DIFF", "EDM") share the beam by moving a neutron guide inside the turbine vessel connecting the copper mirrors with the individual beamline exits. At the turbine exits, safety windows made of 100 μm thick Aluminium are mounted. The energy spectra at the beamlines are an instrument property, the low energy cut-off is given by the limiting velocity of the Aluminium windows, the intensity increases linearly with energy with a maximum at approximately 10-15 m/s with a shape similar to a Maxwellian spectrum. Typical spectra measured have a maximum intensity at 10-15 m/s, depending on the beamline. Maximum densities that can be stored are about 50 UCN/ cm^3.

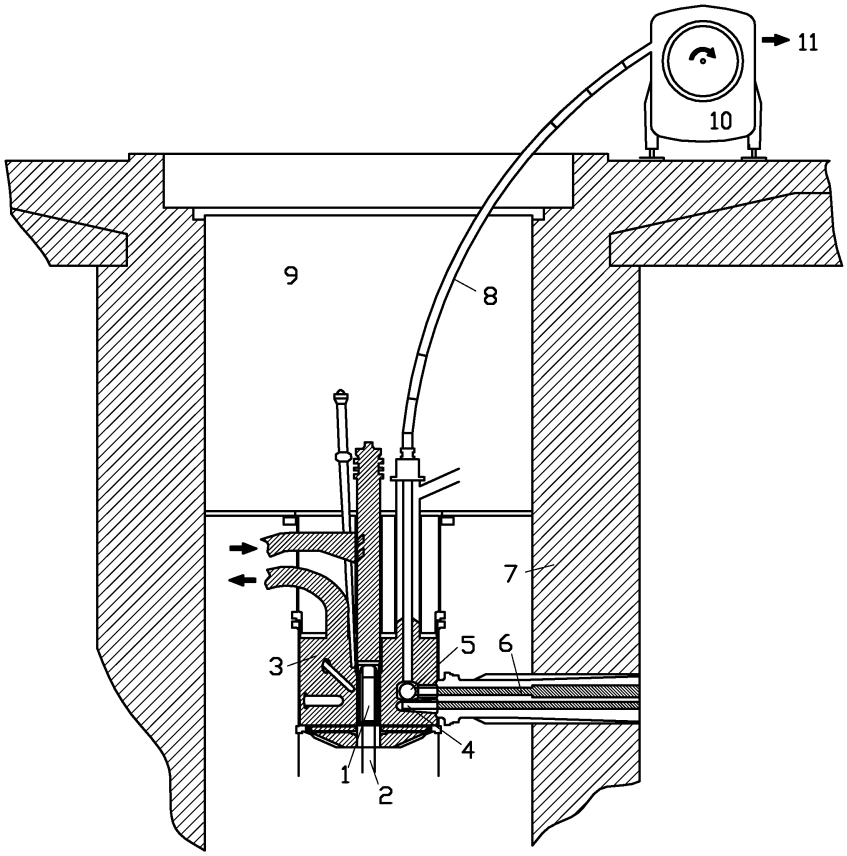

Figure 4.1:

The ILL neutron source. A cross section through the reactor at the Institut Laue-Langevin in Grenoble. [1] Fuel element, [2] control rod, [3] heavy water, [4] horizontal cold source, [5] vertical cold source, [6] neutron guides, [7] concrete, [8] bent neutron guide, [9] light water, [10] neutron turbine, [11] neutron guides to experiments.

4.2 Description of the Setup

Our experiment was located at the beamline "DIFF". The experiment itself was mounted on the iron frame of the platform which was already existing at this beamline. All controls were done from below the platform. A schematic view of the setup is shown in fig. 4.2, a description of the setup is given in the following.

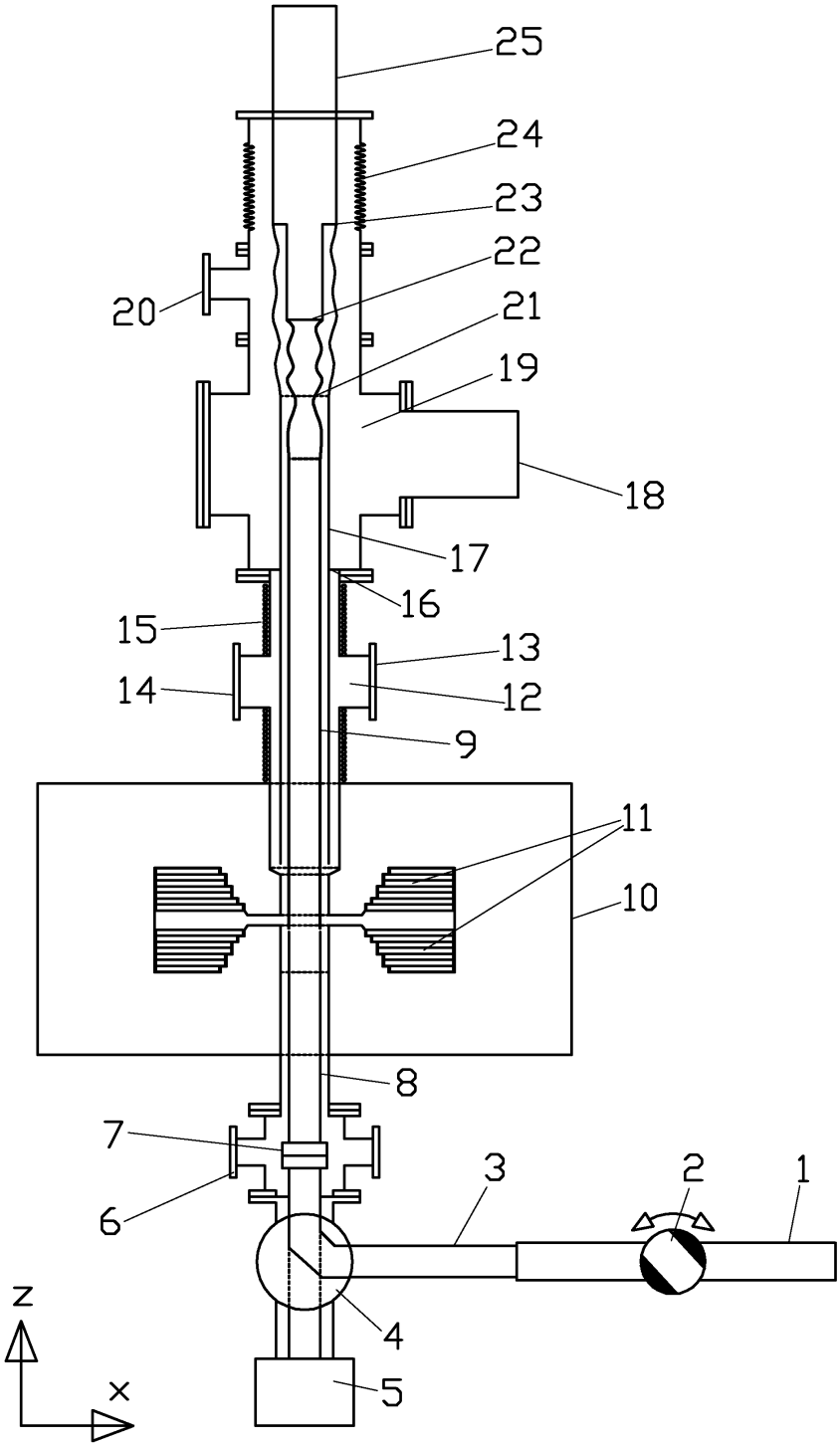

Figure 4.2:

Setup of the experiment. [1] Ni coated neutron guide from the turbine, [2] beamline shutter, [3] stainless steel neutron guide, [4] switch, [5] detector, [6] pumping access, [7] vacuum separation foil, [8] vertical guide, [9] sample, [10] magnet yoke, [11] magnet coils with poles (horizontal), [12] insulation vacuum, [13] pumping access, [14] sensor feed throughs, [15] holding field coils, [16] vacuum separation membrane, [17] thermal shield (Copper), [18] vacuum pump, [19] clean sample vacuum, [20] sensor feed through, [21] flexible thermal copper connections, [22] 8 K stage, [23] 77 K stage, [24] vibration decoupling, [25] cooling machine.

The setup consists mainly of a vacuum system containing the sample, which is inserted into a dipole magnet from above. Below the magnet a feeding neutron guide, a mechanical neutron valve ("switch") and a detector are mounted (see fig. 4.2).
The neutrons enter the system via the feeding guide [*item* 1] and are reflected upwards by a stainless steel mirror in the switch [*item* 4]. On the upper end of the switch housing, a vacuum separation foil is mounted [*item* 7]. It consists of a 7.5 μm thick Mylar foil with a stainless steel support grid structure (93 % transmission) on both sides. A vertical guide tube [*item* 8] is put onto this foil holder and reaches up to the lower end of the sample tube [*item* 9] which reaches below the magnetic field maximum. The sample tube is coated with the sample surface that is investigated or it contains the sample surface that is mounted inside. The typical ID of the neutron guide tubes and the samples is 70 mm, the height of the sample tube is 1080 mm. The parts of the setup are listed in the following section.

- The feeding neutron guide.
  The neutrons are transported from the turbine in Ni coated stainless steel guides with 80 mm diameter [*item* 1]. The height had to be adapted by 250 mm upwards, this is done by using two 20° bends. The guide for the last 600 mm before the entrance of the experiment [*item* 3] has a reduced diameter of 68.1 mm with a stainless steel surface. The flange that connects the 80 mm and the 68.1 mm guides was used for vacuum pumping. In fig. 4.3 the feeding guide from the turbine is shown.

- The beamline shutter.
  In the beamline from the neutron turbine [*item* 1] to the experiment a shutter [*item* 2] is mounted. The shutter is a polyethylene (PE) cylinder with an 80 mm thick neutron guide mounted normal to its rotation axis. The PE cylinder can be rotated by 90° using a pneumatic actuator. The Hydrogen atoms inside PE absorb or up-scatter all incident neutrons. The shutter is closed during all storage measurements to avoid neutrons from the incident guide leaking into the detector through the neutron switch. It is driven pneumatically, controlled by an electromagnetic valve.

- The vacuum system.
  The vacuum system is built from stainless steel using CF type and ISO type flanges. It is separated into a clean sample vacuum [*item* 19] with CF type flanges, an insulation vacuum [*item* 12] and the vacuum inside the switch and feeding neutron guides with ISO type flanges. All turbo pumps and pre vacuum pumps are oil-free. The separation of the insulation and sample vacuum from the neutron guide vacuum is vacuum "tight" to 1 bar difference, the separation of the sample vacuum to the insulation vacuum is tight below $1 \cdot 10^{-3}$ mbar. The insulation vacuum is in cold conditions typically in the 10^{-7} mbar range, the sample vacuum $1 \cdot 10^{-9}$ mbar at 70 K sample temperature. All parts connected to the sample vacuum are sealed with CF type flanges, the insulation vacuum with ISO type flanges and Viton O-rings. The vacua are separated via a stainless steel membrane [*item* 16] and a Teflon ring. Another critical position for vacuum separation is the connection of the sample tube with the vertical neutron guide from below. The connection has to assure that neutrons do not escape to the insulation vacuum outside the tubes and must at the same time have a bad thermal contact. The sample can be cooled, whereas the neutron guide is at room temperature. This is realized with a circular cutting edge on the vertical neutron guide made from stainless steel, where the sample rests with its weight and closes the vacuum connection below 10^{-3} mbar.

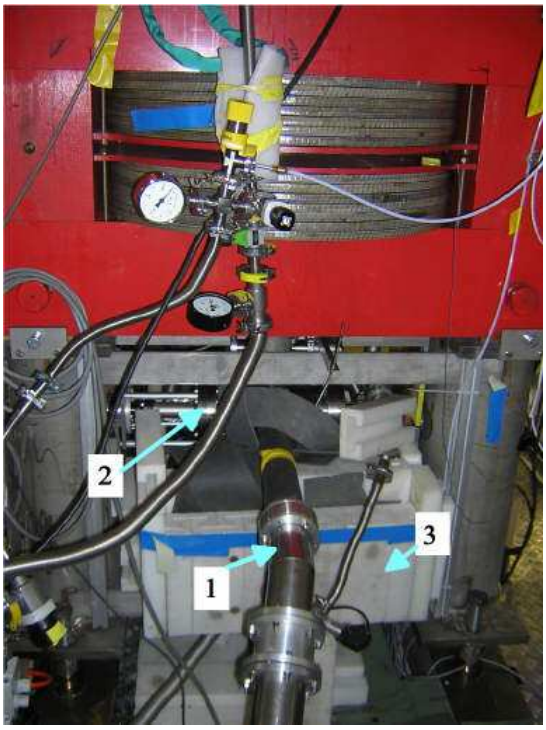

Figure 4.3:

The feeding neutron guide. [1] The neutron guide from the neutron-turbine, [2] the neutron switch, embedded in borated palstic, [3] detector shielding.

The connection is done below the middle of the magnet gap, which cannot be reached by neutrons during storage. Monitoring is done using Pfeiffer Cold Cathode and Full Range gauges. A quadrupole mass spectrometer (QMS) is built in directly at the upper end of the sample tube. Pumping is done using two turbo molecular pumps (TP) at positions [*items* 6, 13] for the insulation vacuum, and a CF-160 TP [*item* 18] with an included drag pump and a pumping power of 600 l/s for Hydrogen. In cold conditions the cryo insert with a large surface also acts as a pump, directly on the top of the sample volume. Cables for temperature sensors and heaters are fed through the insulation vacuum [*item* 14]. To obtain good vacuum condition, all parts were cleaned with washing detergent to remove hydrocarbon containing materials. The neutron guide parts are rinsed with demineralized water afterwards. The decision if the cleaning was good or not was taken by looking by eye at the surfaces after rinsing: if the water did not form drops on the surface but made a film on the whole area, oil and fat substances have been removed. For drying, the parts were protected from dust using clean room tissues as cover of the flanges and holes of the parts. Handling was done with gloves if possible.

- The neutron switch.
  The switch [*item* 4] has two positions, one is filling, where neutrons can enter the system and are reflected upwards via a polished stainless steel mirror. The Fermi potential of stainless steel is 194 neV, whereas the vertical distance of the mirror to the upper end of the sample is 1750 mm. The second position is a vertical neutron guide (dotted lines) that connects the vertical guide with the detector [*item* 5] without large mechanical slits allowing neutrons to fall down directly in the detector. A CAD picture of the switch is shown in fig. 4.4. The ID of the tubes is 71.0 mm for the vertical guide sections,

the horizontal parts have an ID of 68.1 mm. The diameters were chosen in such a way that neutrons, falling down from the sample, always enter a guide with a slightly larger diameter to avoid losses and additional reflections on mechanical connections.

The switch is driven with a pneumatic cylinder, controlled by an electromagnetic valve. It is not completely tight for neutrons, there is small leakage from the feeding guide to the detector.

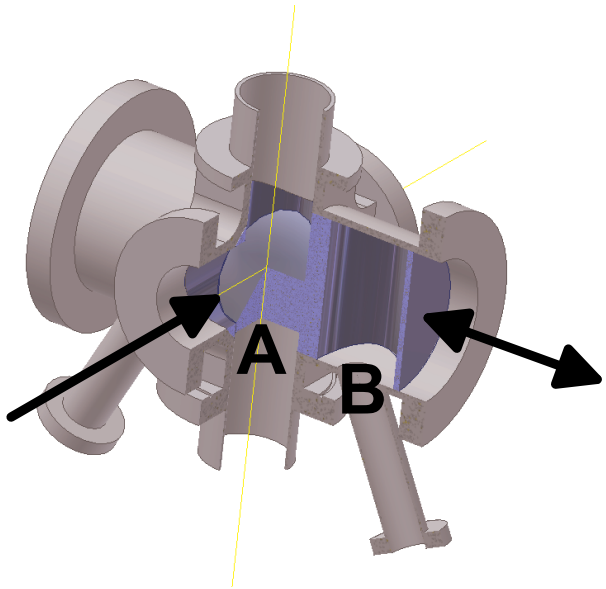

Figure 4.4:

The neutron switch. The direction of the incident neutrons is shown by the arrow (left), the feeding guide tube to the sample is connected on top, the detector on the bottom flange. The dark blue part can be moved in two positions, as indicated. Position A is a stainless steel mirror to feed neutrons in the volume, position B is a vertical connection from the vertical guide to the detector.

- The vacuum separation foil.
  A 7.5 μm Mylar^{TM} foil is mounted in a foil holder to separate the vacuum of the neutron guide and the neutron switch from the sample vacuum [*item* 7], which reaches down to this position (see fig. 4.5). To sustain a pressure difference of at least 1 bar from both sides of the window two honeycomb support structures of stainless steel with 0.2 mm thickness is used with an area of 7 % of the beam cross section on both sides of the window. Outside the foil holder and the vertical tube is the insulation vacuum. UCN transmit the foil during filling and during emptying, therefore it is important to have a high transmission and a low Fermi potential. The chemical composition of Mylar is $C_{10}H_{10}O_4$, it has a density of 1.35 g/cm^3 and a Fermi potential of 54 neV.

- The vertical guide tube.
  The vertical guide tube [*item* 8] is a honed and electro-polished stainless steel tube with 70 mm ID, it has a cutting edge on the top, where the sample tube rests on. On the bottom it is mounted in the foil holder with a Viton O-ring.

- The sample tube.
  Different sample tubes [*item* 9] were used for the measurements. They consist of an

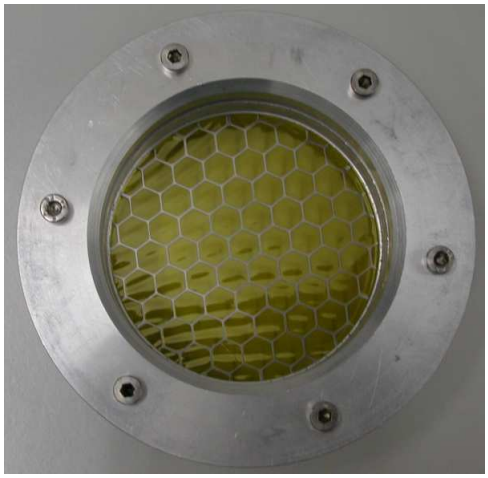

Figure 4.5:

Vacuum separation foil. The foil is mounted between two honeycomb support structures, the flanges press on the support structures with O-rings, between the foil and the structures are no additional vacuum seals.

Aluminum tube with 10 mm wall thickness for heat condutivity, with a reduced wall thickness to 1.5 mm for the lower 20 cm to fit into the magnet bore. The sample is connected via flexible Cu strips [*item* 21] to the cooling machine [*item* 22] and centered inside the thermal shield [*item* 17] with 2 centering rings made from Teflon. A detailed description of the samples is given in sec. 4.4

- The cryogenic system.
  On the top of the vacuum system a two stage CRYOMECH Gifford-Mc Mahon cooling machine [*item* 25] driven by a He compressor is mounted with a minimum temperature at the cold stage [*item* 22] (without additional heat load) of 8 K and a power of 10 W at 10 K. To decouple the sample from vibrations, the cold stage of the cooling machine is connected to the top of the sample via flexible Copper fibres [*item* 21] with a total cross section of 500 mm^2. The vacuum system is connected via flexible bellows to the cooling machine. The cooling machine is mechanically supported by a frame mounted on the magnet return yoke.

  The connections are done with Chromium coated brass screws and springs and a layer of Indium in between the surfaces that are mounted together. To be able to cool down to lower temperatures a Copper tube [*item* 17] is put around the sample tube as a thermal shield, wrapped with Aluminum foil and aluminized Mylar. It is connected to the 70 K stage of the cooling machine [*item* 23] also with flexible fibres for vibration decoupling. The mounting is done outside (see fig. 4.6). It is put into the vacuum housing from the top using a crane. The sensors for temperature control were Cernox^{TM} sensors for the operation in strong magnetic fields with 4 Kapton^{TM} - insulated wires each, connected to a vacuum feed through [*items* 14, 20]. Sensors were mounted on the cooling machine, the top, middle and bottom of the sample.

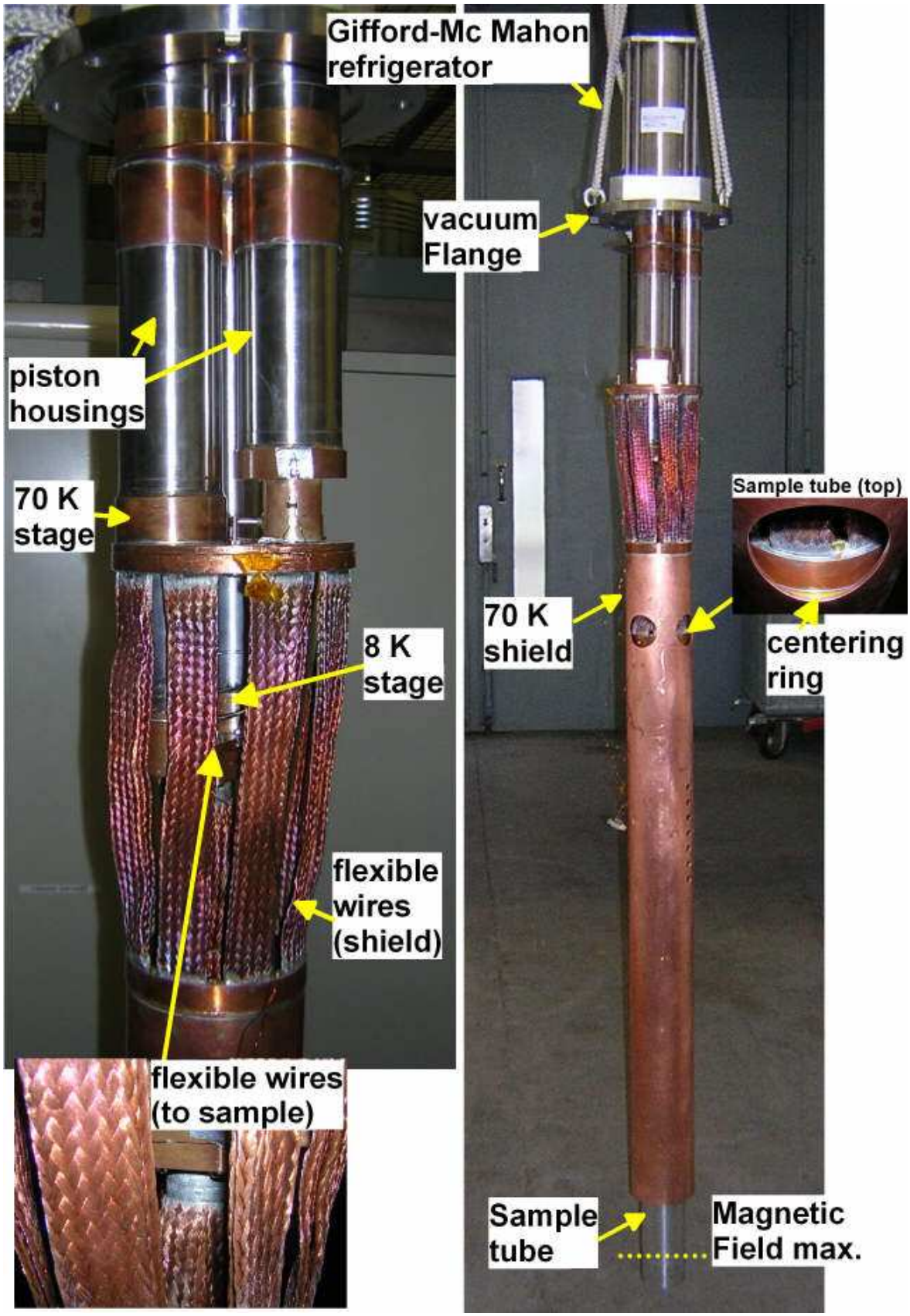

Figure 4.6:

Right: the cryogenic insert. On the top is the cooling machine. Flexible Copper fibres connect the thermal shield and the sample tube (inside) to the cooling machine. Left: the connection of the 8 K stage to the sample tube via Copper fibres.

- The magnetic shutter.
  The magnetic shutter is a conventional H-type dipole magnet [*items* 10, 11] with a bore for the vacuum housing of the storage tube in axial direction referred to the coils. The hole with 81 mm diameter is a compromise between a large diameter, which is preferable for neutron transport, and a small diameter, which allows for a higher field strength. The coils are made by copper leads with a quadratic cross section with OD = 8 mm and ID = 6 mm.

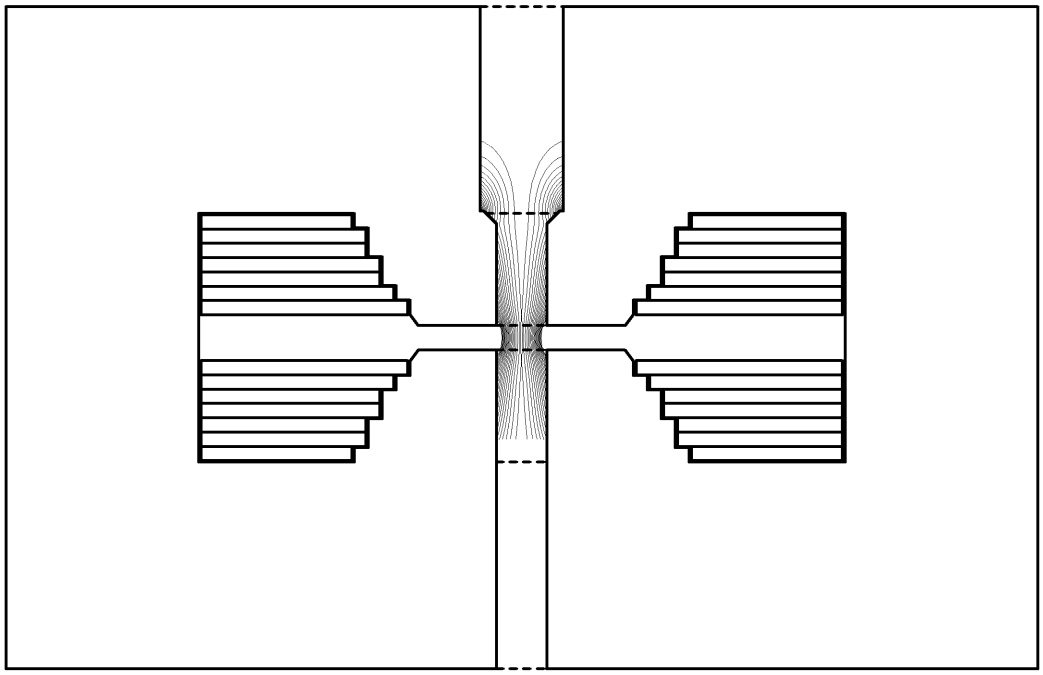

Figure 4.7:

Field lines of the magnet in the bore. The hole in the middle area is the bore for the vacuum system containing the sample. Field lines in the relevant part for storage are shown. In the middle are the poles of the magnet, surrounded by the coils. The big part around is the iron return yoke, its height is 80 cm.

The resistance of the coils is 0.582 Ω, which defines together with the inductivity and the power supply the maximum raising and lowering time of the magnetic field. The coils are cooled with 12 bar water at room temperature, exiting with a maximum temperature of 55°. The return yoke is made from iron with a weight of 3.5 t. The magnet current is 300 A with 200 V, connected via two 195 mm^2 Cu cables coming from the magnet power supply, located below the experimental platform. The field in vertical direction are shown in fig. 4.8 and the field lines in fig. 4.7, hysteresis effects are small. The magnetic field is measured on axis with a Hall-sensor [67] in vertical direction, denoted with z, the radial component if the field is always 0. The coordinate z is in upwards direction of the sample tube, it is 0 at the position of the geometrical center of the magnet. The field was calculated using Poisson Superfish 7.12 [68], which is in good agreement with the measured field values. The field values off-axis are calculated values, where the maximum deviation to the real field should be on the order of 1 % or less [69].

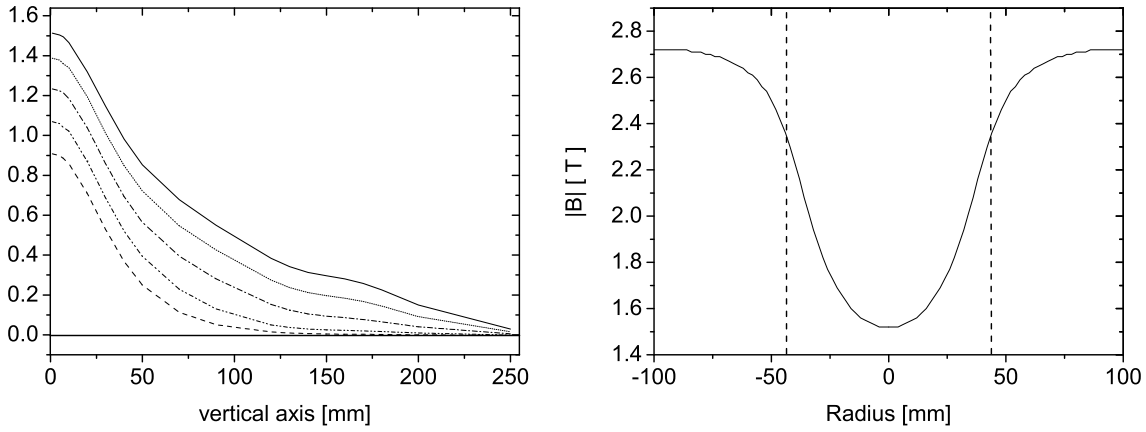

Figure 4.8:

The left picture shows the measured field strength in z direction, starting from the middle of the magnet gap (z = 0). The curves denote different magnetic field levels with different currents, as they were used for measurements. The right graph shows the calculated field strength at z = 0, in dependence of the radius. The field strength reaches a minimum at radius r = 0, corresponding to the center of the tube.

- The holding field coils.
  The holding field [*item* 15] is produced by a coil around the vacuum system. The current is typically in the oder of 10 to 20 A, corresponding to a field of $55 \cdot 10^{-4}$ T to $85 \cdot 10^{-4}$ T. The diameter of the coil wires is 1.5 mm, fixed with epoxy. During continuous operation the working temperature of the coils was 360 K.

- The detector.
  The detector was supplied by the Frank Laboratory of Neutron Physics in Dubna, [*item* 5]. It is a ^{3}He counter with a 100 μm Aluminum window at the entrance and an Aluminum support structure, see fig. 4.9. Aluminum has a critical energy of 54 neV, therefore the detector has to be mounted at least 540 mm below the experiment so that the neutrons have a sufficient energy to enter. Neutron detection is based on the nuclear reaction:

$$^3He + n \rightarrow p + t + 780keV \tag{4.1}$$

  The detection volume is filled with 18 mbar ^{3}He for neutron absorption, 12 mbar CO_2 and 1070 mbar Argon. The low He pressure and the thickness of about 20 mm makes it practically insensitive to thermal neutrons. For ultracold neutrons the attenuation length is in the range of 10 mm. On the bottom of the gas volume a wire electrode with +1000 V collects the charges. The signal is preamplified internally.

  The geometry of the detector and the low gas pressure reduce the sensitivity to thermal neutrons further. The level of γ rays is low at the detector position and no issue for the measurement. Shielding is done using borated plastic and Cadmium as an innermost layer around the detector. Around this, polyethylene bricks in several layers are put with a total thickness of more than 200 mm. Only the direction upwards to the neutron guide cannot be shielded. The typical background rate with shielding was 4.8 $\pm$ 0.3 mHz.

Figure 4.9:

The detector with an Aluminum entrance window with support structure. The neutron guide is connected on the top, below is the sensitive volume with the collecting electrode. The preamplifier with connectors for the signals are on the bottom.

- Mechanical support structure.
  The total weight of the experiment on the platform is about 4000 kg which is near the limit of the platform structure. The magnet yoke, to which all parts are connected is placed on a table with screws for horizontal fine-adjustment. The table of the magnet has adjustable feet. The height was adjusted to place the neutron entrance of the experiment 250 mm higher than the neutron guide from the turbine.

Figure 4.10:

Picture of the experiment. The photograph was taken when the setup was mounted for tests at PSI.

4.3 Data Acquisition and Slow Control

The experiment was controlled from below the experiment platform. The power supplies, temperature and pressure readout, detector readout, turbine communication, experiment control, online analysis and data storage are done at this position.

All controls are connected to one DAQ-PC. The PC has two cards built in: one digital IO card NI^{TM} 6711 PCI, which supplies the 0-10 V signal for the magnet operation and several digital IOs. The pulses from the detector are counted with a NI 6602 PCI card. For the operation a Labview^{TM} program is used. The software consists of two packages:

- The slow control (see sec. 4.3.1), which is responsible for the readout of temperatures, pressures, any changes of measurement parameters and status information.
- The measurement control (see sec. 4.3.2), containing the manual and automatic operation of the experiment and the readout of the detector counts, online display and data storage.

4.3.1 Slow Control

The slow control regulates the

- Magnet and magnet power supply status
- Pressures, mass spectrometer
- Temperatures
- Turbine feedback
- Shutter positions
- Automatic filenames
- Log files for temperature and pressure
- Log files for any parameter changed by the measurement program
- Data storage
- PID controller for temperature stabilization.

The schematic layout of the experiment control is shown in fig. 4.11. All digital IOs and the analog output signals are controlled via a NI 6711 PCI card, which can be directly controlled by the LabVIEW program.

Temperature and Pressure Readout

The temperature sensors on the cooling machine and the sample tube are read out via a Lakeshore^{TM} 340 temperature controller, for the sensors a calibration curve is programmed in the controller. The controller is connected to the DAQ-PC via a IE488.2-USB converter cable, the readout is done using the LabVIEW program. Also heaters on the sample tubes (2 resistors with 50 W) are controlled with this temperature controller using a built PID algorithm, the parameters are set and controlled by the LabVIEW program.

The pressure sensors (sample vacuum, insulation vacuum and switch vacuum) are read out by a Pfeiffer Maxi Gauge controller, which is connected to the DAQ-PC via a RS 232c connection and read out by the LabVIEW program [70].

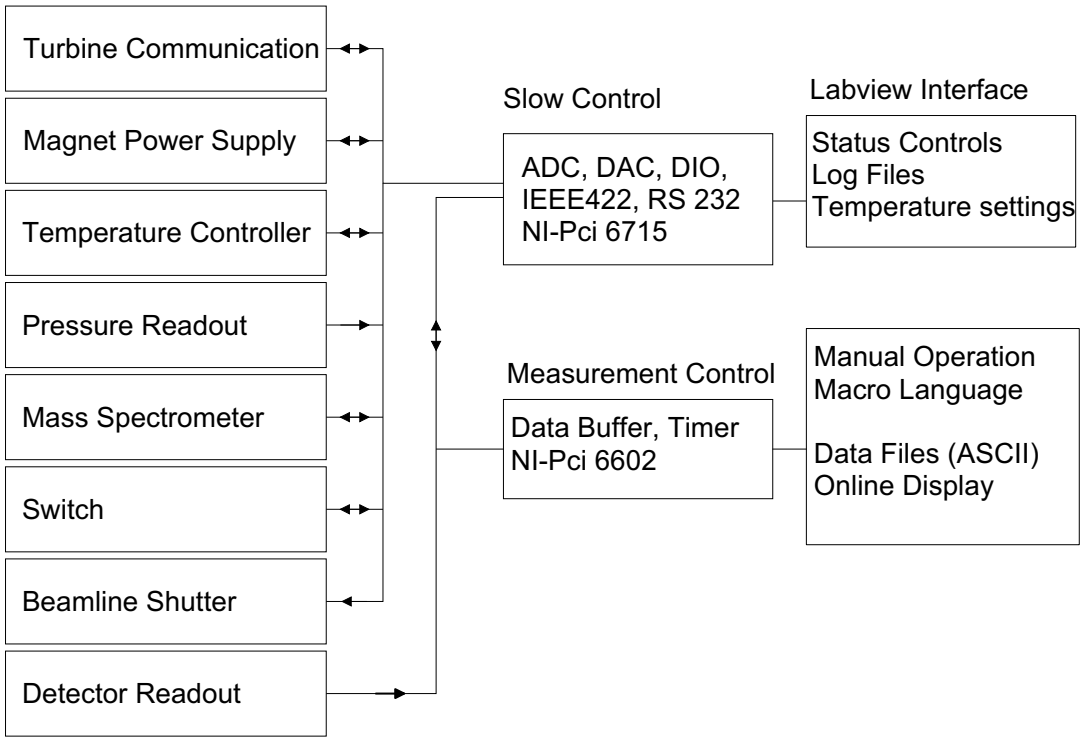

Figure 4.11:

Schematic layout of the experiment control. All devices (left column) are connected via various interfaces to the DAQ-PC, where the signals are processed in a LabVIEW program, consisting of the slow control and the measurement control.

Magnet Operation

The magnet is operated via the power supply, which has been modified to allow for fast switching times of the magnetic field. It uses an analog input for a voltage signal, which is connected to the analog output of the PC, producing a voltage level between 0 to +10 V. This controls a current from 0 to 300 A, which depends strictly linearly on the input signal. The ramp time can be chosen arbitrary. If the ramp time is shorter than 3 s, a shortest possible internally programmed ramp is used. The maximum field is reached with 300 A coil current, the dependence of the maximum field strength on the magnet axis is shown in fig. 4.12. The internal ramp of the power supply can be reproduced with a negligibly low uncertainty. The time ramp of the magnetic field using the internal ramp of the magnet is shown in fig. 4.13. The power supply was adapted to allow for fast operation of the magnet currents. Additional capacitors in the power supply reduce hysteresis effects from the magnet iron to a negligible level. If the magnet is turned off using the (fastest possible) internal ramp, the field is reduced to 5 % in 2 s. The residual field decreases slower; this is not relevant for our application.

The water cooling from magnet and power supply, the water pressure and the temperature of the magnet, as well as several control functions are bundled and read out by the slow control by a "Magnet OK" and a "Power OK" signal.

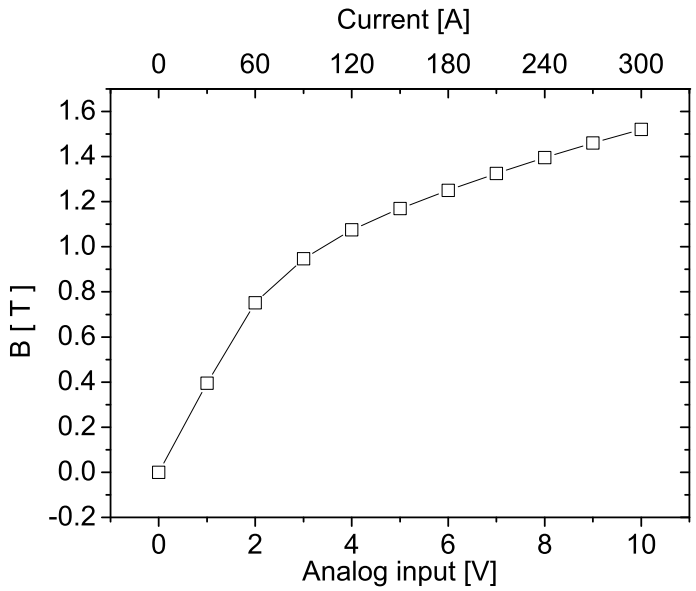

Figure 4.12:

The measured magnetic field strength at x = 0, z = 0 as a function of the voltage used to control the magnet power supply, the corresponding coil current, which is linear to the input voltage, is shown on the top.

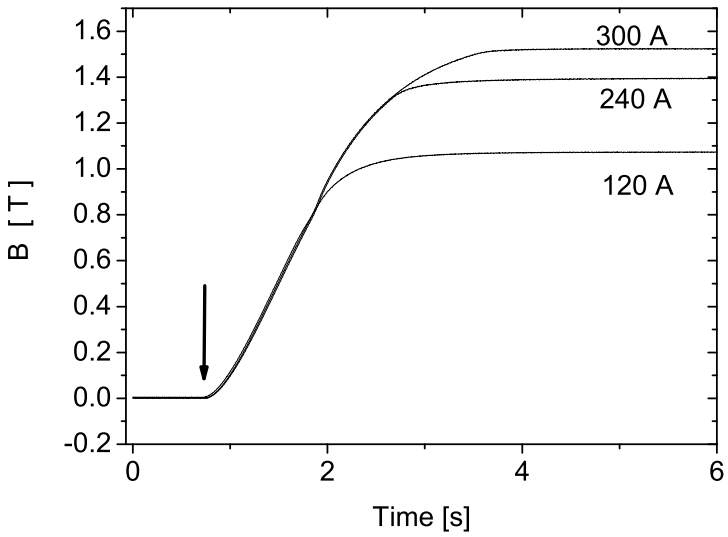

Figure 4.13:

The measured ramping of the field to different values using the internal ramp of the magnet power supply. The ramp starts at the position of the arrow.)

Turbine Communication

The turbine is operated as an user instrument. All control functions are provided in an interface which can be accessed by the users.

We share the neutron beam for the experiment with two other experiments, one of them is the nEDM experiment, which is the "master". Inside the turbine is a stepping motor controlled neutron guide which connects the UCN "beam" from the turbine-wheel to one of the three beamlines. The setting can be controlled via a communication interface consisting of three signals.

- Turbine request: A 5 V signal applied by the user informs the turbine to move the internal guide to the beamline, where the request comes from, if there is no veto signal from another user.
- Turbine veto: to avoid, that another user moves away the beamline during the filling of one's experiment, on can set a veto signal. The signal can be overwritten by the nEDM control PC.
- Turbine OK: If the beam is on a distinct beam position, a 5 V signal is delivered from the turbine. This signal is produced by a mechanical contact switch and corresponds directly to the position of the guide inside the turbine.

4.3.2 DAQ Program

The measurement program controls the whole experiment. Shutters, magnet, turbine communication, temperature stabilization and detector readout can be controlled in manual mode or in macro mode. When a parameter is changed, a notification is sent to the corresponding og file.

In macro mode a simple "language" is used, which was written especially for this experiment. It contains all commands that can be carried out in manual mode. The tasks that have to be done and the actions that have been carried out are listed in a text file with a time label in the beginning of each line. The commands are separated with a tab symbol, each time a task is called, a notification to the log file is sent. The commands used are

- Beamline open / close: opens or closes a shutter in the beam line between the turbine and the neutron switch via one digital output and a magnetic relay to operate the pneumatic actuator.
- Switch fill / empty: moves the switch between "fill" and "empty" position using two digital outputs where one is set 0 and the other one 1 or reversed.
- Magnet 0 V 7 V 3 s: This command switches the magnet current from 0 to 7 Volts with a linear ramp of 3 seconds. The magnet current is maximum 300 A, corresponding to 10 V output from the analog output of the DIO card (16 bit resolution, corresponding to $\Delta V = 1.5 \cdot 10^{-5}$). The magnet characteristics are shown in fig. 4.12.
- Delay time 2 s: stops the timer that operates the experiment for 2 seconds.
- Delay TurbineOK: stops the timer until the turbine sends back an OK signal, i.e. the neutron beam is now directed to the experiment (see sec. 4.3.1).
- Turbine request on / off: A signal from the digital output to request the neutron beam can be sent to the turbine.

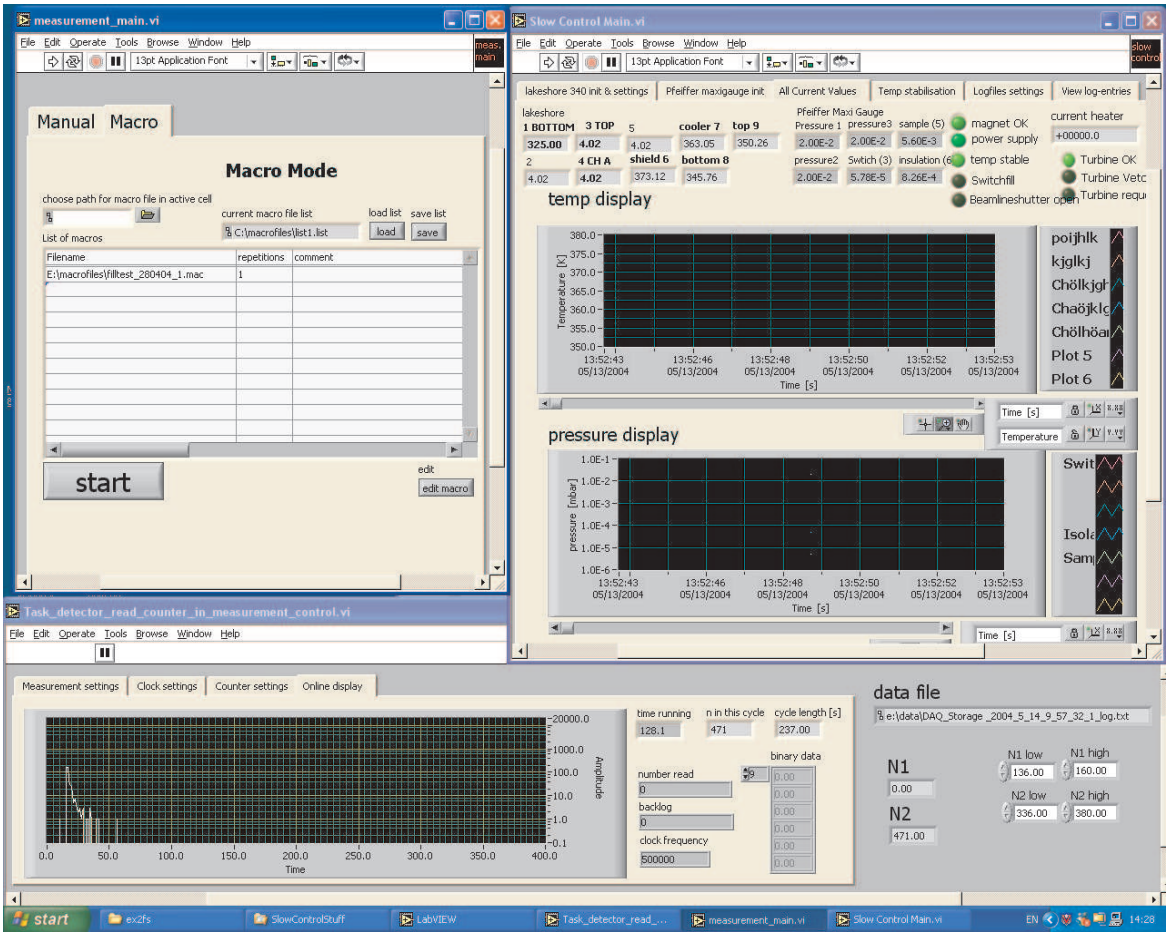

Figure 4.14:

Screen shot of the LabVIEW user interface. The upper right window is the slow control, where the status, the temperatures and the pressures can be read. The upper left window controls the measurements. In macro mode a list of macro files is done, in manual mode the individual controls can be operated by pressing buttons. The lower window is the online display for the current measurement, which is started and reset by the measurement control. The counts from the detector are shown as a histogram on a time axis with 1 s bin width.

- Turbine veto on / off: A veto signal can be sent to the turbine to avoid that an other experiment moves away the beam while it is used in the experiment.
- Detector measurement-type cycle-length s: measurement-type can be "manual" for the case of single measurements that are controlled manually, where the detector readout is activated by a button, "depol" or "storage" for typical automatic measurements and "test" for tests outside data taking. The cycle-length is a number in seconds, chosen equal to or shorter than the total macro file length. This option also starts the online display and the detector readout. The option is written into the header of the data file.

An example of a macro file is shown below (150504_cleaning_N1.mac) :

1	Beamline	open
1.01	Switch	fill
1.02	Turbine	request on
1.03	Delay	TurbineOK
1.04	Turbine	veto on
1.05	Turbine	request off
2.0	Detector	Storage 237 s
2.01	Beamline	open
14	Magnet	0 8 3
17	Beamline	close
17.01	Switch	empty
17.02	Turbine	veto off
117	Magnet	8 10 1
137	Magnet	10 0 1
240	Beamline	close

This sequence controls one measurement. The left column is the time stamp in seconds after the beginning of the measurement, the second column the command and the third line the parameter of the command. A list of different macro files can be entered in a list file with a number of iterations for each of these files. In manual mode the user can use all these commands in a similar way by pressing buttons and choosing input values in text fields in the LabVIEW window. Every action is logged into the parameter change log file, both from manual mode and macro mode.

4.3.3 Detector Readout

The detector signal is preamplified inside the detector electronics. The outgoing signal is +200 mV in the peak, which is further amplified in an ORTEC delay amplifier. The resulting pulse is positive with about 1 V height and a length of 3 μs. The preamplified pulse is also connected to a discriminator. In the discriminator the noise is removed by a suitable threshold. The outgoing TTL signal is stretched to fit to the length of the pulse in a delay trigger module. The amplified analog signal and the stretched rectangular pulse go to the pulse height analyzer card. The rectangular pulse is in coincidence with the analof signal and is used as gate. The rectangular pulses are also used for data acquisition, connected to the counter input of the NI 6602 card of the DAQ-PC. A typical pulse height spectrum is shown in fig. 4.15.

The time resolution is limited to about 300 kHz according to the length of the detector pulses. The count rates are typically much less than 20 kHz, in storage mode between mHz and kHz. Any dead time corrections can be therefore neglected due to the low count rates.

The detector readout program uses the scaler and clock functions of a NI 6602 PCI card. The card has four channels, which can be configured as pulse output or as a counter. Channel zero is configured as a clock output and produces a 500 kHz TTL pulse sequence, channel one works as a counter with a 32 bit resolution. The clock output is fed into the source input of the counter. Every time a gate signal from the detector electronics comes to the gate, the current number of the clock input is written down in continuous appending mode into a hardware buffer memory (see fig. 4.16). The buffer memory is read every second by the LabVIEW program and the contents is written to a file.

This allows for arbitrary binning of the counter entries in the offline analysis, since every neutron has its own time stamp with 2 μs resolution. For the 32 bit counter this allows a maximum measuring time of 8600 s without resetting the timer to zero, which is by far more

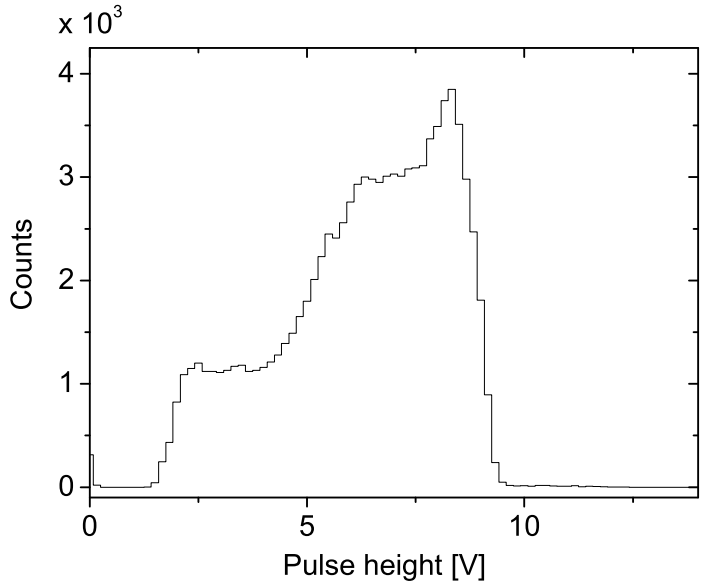

Figure 4.15:

The pulse height spectrum of the detector after amplification in the ORTEC delay amplifier. It is determined by the energy of the nuclear reaction, the lower energy part is due to wall effects. In offline tests the detector was refilled and it was found that these lower pulseheights are wall effects due to the Helium pressure. The signal is gated using a digital pulse from a discriminator. This signal has a threshhold of 2 V to cut low energy noise.

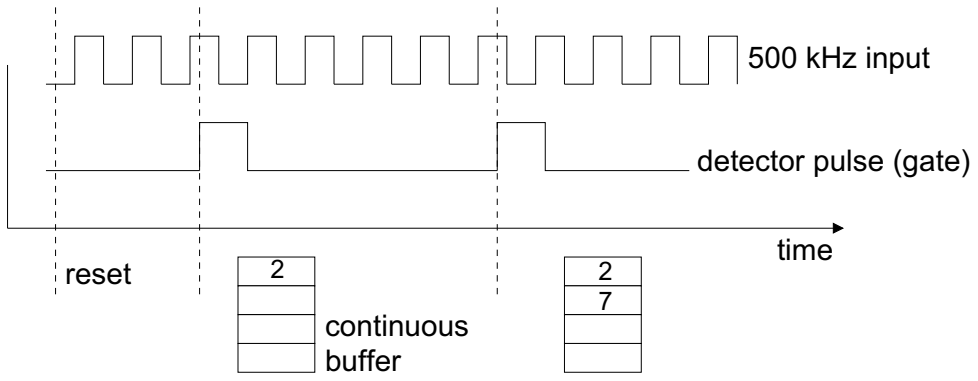

Figure 4.16:

Detector readout. The distance between the 500 kHz clock signals is shorter than the detector pulse length. The maximum count rate expected is 20 kHz, for storage mode < 1 kHz. The list entries below the pulses show the time stamps of the individual events in the hardware buffer.

than the typical measuring time. Configuration and readout are done by means of a LabVIEW detector readout program. For each measurement a unique filename is generated, containing a header with the time, run length, measurement type and the macro file name, all measured counts with their time label and a footer. In parallel the same dataset is written but the data is here binned in 1 s bins for the simplification of online analysis.

4.3.4 Data Storage

All data is stored on a so-called RAID drive. A RAID drive is an array of (at least) two hard disks which are used in mirroring mode, i.e. the data is written on both disks at the same time. This reduces the probability of data loss if a disk would get damaged. In our case we use a two times 120 GB unit from FirewireDirect^{TM} which is connected via USB 2.0 to the DAQ-PC in an external housing.

Detector Data

The filenames of the datafiles are generated automatically in the LabVIEW program. The format is ASCII, with a header and a footer containing the macro file name, start and end time/date, total counts and sample temperature. The file is generated twice. One file contains a time stamp for each event counted in the detector with a resolution of 2 μs, one event per line. The second file contains the same data but binned in one second bins. The format is in two columns, the first column contains the time in seconds, the second column contains the corresponding number of events at this time. The files are always written on the disk at the end of each individual measurement, i.e. when the specified time for the detector readout ends. An example of a typical data file is shown here:

```
Measurement type: Storage , 15.05.2004, 01:04
Clock speed = 500000 Hz, Temp = 3.096110E+2 K,
Cycle length237 s, comment: no
Macro: E:\macrofiles\storage_030504_cleaning_N1.mac.
0.661210
4.504308
5.147564
5.681610
6.462618
8.628712
9.010298
10.315900
11.390634
11.505690
12.198366
14.501700
....
157.674103
167.468613
Total time running = 237 s, Total counts = 28420
End of measurement 15.05.2004, 01:04.
```

Slow Control Log files

The log files are generated automatically for each date. As mentioned before the log entries are written on the RAID drive. There are three different kinds of log files: The temperature log, where every 30 s the reading from the temperature sensors is put in one line with a time stamp, always appended to the file with the current date in the filename. The pressure log is similar, the third log file is the parameter-change log. In the parameter-change log file, all changes, like commands for the measurement and response from the devices are written.

4.4 Samples

Our experiment focuses on the comparison of Beryllium (Be) coated surfaces with diamond-like Carbon (DLC) coated surfaces. To store neutrons it is enough to cover the uppermost layer of a surface with a neutron reflecting material according to the penetration depth of UCN into surfaces (cf. eq. 2.15), which is in the order of 10-100 Å. Carbon and Be are practically the only (solid) materials suitable for long UCN storage due to the combination of a low absorption cross section combined with a high scattering length density.

Carbon of high density is called DLC, it is obtained by special mechanisms of film deposition. The so-called diamond-likeness is a relative number describing the ratio of chemical bonds as in diamond to those typical for amorphous Carbon (graphite). The terms for the chemical bonds are sp^3 hybrid orbitals for diamond and sp^2 for graphite. The sp^3 orbitals allow for a higher packing density and therefore a higher density of the material. A high density results in a high Fermi potential, making high quality DLC a good choice for neutron storage. Recent test measurements of the critical velocity of various DLC coatings using neutron reflectometry [71] showed critical velocities at about 7 m/s, which was the reason for a detailed investigation of the storage properties in this experiment.

The samples that have been measured are Be and DLC coatings on the substrates Al, quartz (SiO_2), Al-foil and PET-foil (polyethylene). A drawing of a sample tube is shown in fig. 4.17.

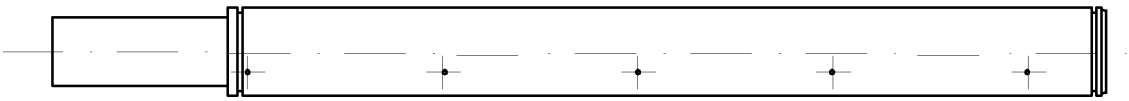

Figure 4.17:

Sample tube. The total length is 1080 mm, the inner diameter is 70 mm, the wall thickness 10 mm. At the left side the wall thickness is milled down to 1.5 mm to fit into the bore of the magnet. The crosses mark threads for temperature sensors and heaters. Any mechanical treatment was done without iron containing tools.

To mount a sample the setup has to be opened at the top and the cryogenic insert (cooling machine with flexible Cu-strips, sample tube and thermal shield) is put on an external support structure using a crane. The thermal shield has to be unscrewed to access the sample. The sample is connected to the flexible copper fibres with eight brass screws, which are opened for sample exchange. Handling of the sample tube is done with gloves to avoid additional hydrocarbon contamination. The sample surfaces are not treated in any way before mounting, the transport was done in a closed container to protect them from dirt and dust. Cleaning with acetone and alcohol afterwards was done on the outside of the sample tube.

4.4.1 List of Samples

- Al-tube with a Beryllium coating from PNPI[1], ID 70 mm, "BE on Al-tube, PNPI"
  The Be coating has been produced using magnetron sputtering. A Be sputter target mounted inside the sample tube with a surrounding magnetic field on a negative potential is hit by Argon ions and Be ions are sputtered away. They follow a potential difference to the sample walls and produce a film there. The film thickness is thicker than 100 nm.

[1] Petersburg Nuclear Physics Institute, Gatchina, Russia

It is crucial that the thickness is significantly larger than 10 nm, which is a few times the entering depth of UCN into materials.

- Quartz-tube with a Be coating from PNPI, ID 65 mm, "BE on Quartz-tube, PNPI"
  The quartz tube is sputtered in a similar way as it is done for the Al-tube. A crucial point for the sputtering on non-conducting substances is, that the film is grounded from the beginning.

- Al-tube with a Be coating from TUM[2], ID 70 mm , "BE on Al-tube, TUM"
  The tube is also coated with magnetron sputtering. The procedure is to coat first a layer of Aluminum on the surface and without breaking the vacuum sputtering the Be coating on the clean surface.

- Al-tube with a DLC coating from the VT[3], ID 70 mm, "DLC on Al-tube, VT"
  The tube is cleaned with HF to remove all hydrocarbons from the sample. All cleaning is done in a dust-reduced environment. The DLC coating is done with pulsed laser deposition (PLD). This technique is very common in solid state physics to produce such layers. A Carbon target is mounted in the sample tube and hit by a laser beam. The wavelength of the laser is responsible for the energy of the Carbon particles. A UV-laser wavelength produces a suitable energy of the carbon atoms so that they form a layer on the sample substrate with a higher density than graphite.

- PET-foil with a 150 nm DLC coating from IWS[4], "DLC on PET-foil #1, IWS", mounted inside two shells made of aluminum, ID 70 mm
  The foils are coated using laser arc deposition. Here the film is produced by a laser induced vacuum arc from a cylindrical sputter target to the (flat) sample foil. The density of the films depends on the conditions of processing. Using this method one can produce big surfaces coated with DLC.

- PET-foil with a 120 nm DLC coating from IWS, mounted inside two shells made of aluminum, ID 70 mm, "DLC on PET-foil #2, IWS". A layer of Titanium is sputtered as an interface layer on the Al-foil to increase the adhesion of the DLC layer on the substrate.

- Al foil with a 150 nm DLC coating from IWS, mounted inside two shells made of aluminum, ID 70 mm, "DLC on Al-foil, IWS"

Foils as surfaces are the cause of some practical difficulties in the measurement. By rolling them inside a tube to produce a storage volume, an uncoated edge will be visible for the neutrons over the whole distance in height. This edge would dominate the measurements, and therefore a "trick" is used to produce a suitable storage volume. The foils are mounted in a way that there is no slit, as it is shown in fig. 4.18. The Aluminum-foil (left) is mounted with screws to assure that no slit can appear. In the case of the PET-foil, which is relatively soft compared to the metal foil, the mounting is done in a tube consisting of two half-shells, which are screwed together.

The Quartz-tube was mounted inside an Al-tube with 70 mm ID, identical to the coated tubes. The Al-tubes are honed and mechanically polished inside with a mean roughness of $< 0.1\,\mu$m. All processing was done using tools that do not contain ferromagnetic substances

[2]Technische Universität München, Germany
[3]Virginia Polytechnic Institute, USA
[4]Fraunhofer Institut für Werkstoffkunde und Strahlführung, Dresden/Dortmund, Germany

to avoid residuals of ferromagnetic substances below the sample surface, which could cause disturbances in the magnetic field of the shutter.

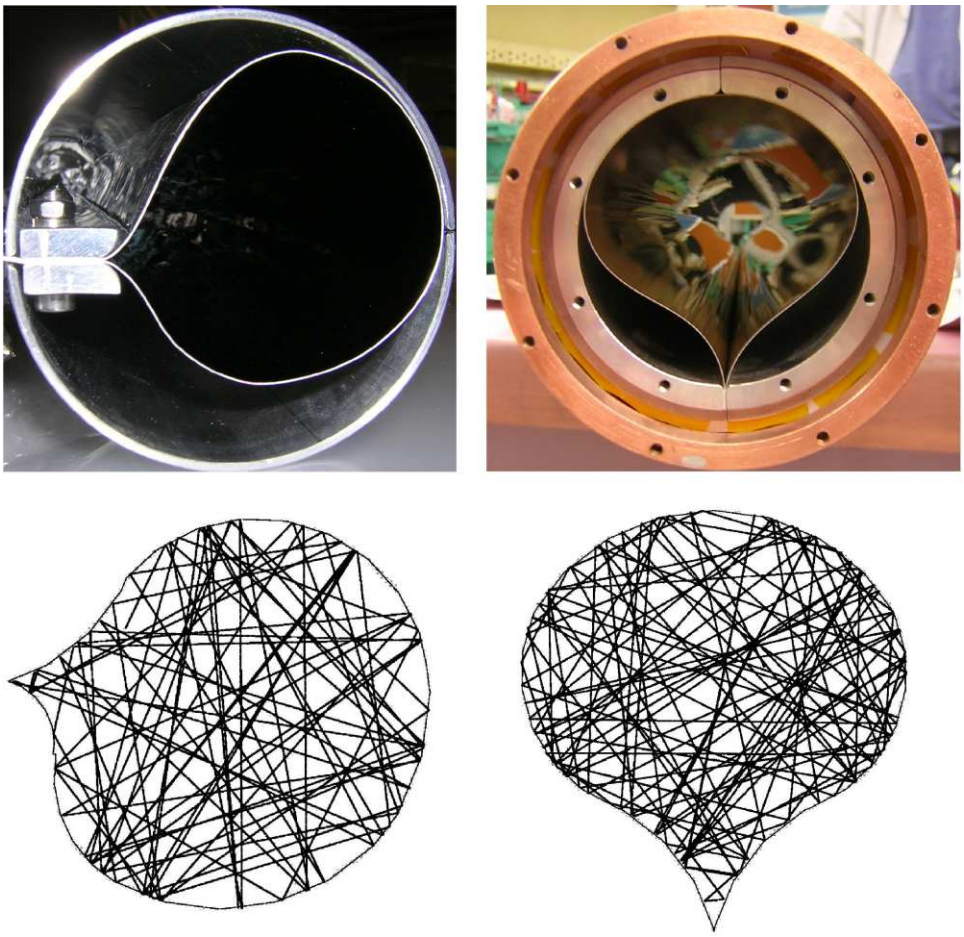

Figure 4.18:

Foil samples. The foils are mounted inside two half-shells which are screwed together. Left: Al-foil sample viewed from the bottom, where the neutrons enter. Right: PET-foil sample viewed from the top. The two Aluminum half shells can be ssen where the foil is mounted. The copper tube around is the thermal shield. Below, two geometries are shown as they are used in the simulation. The simulated geometry is averaged for the shape of the foils on both ends of the sample.

Chapter 5

Measurement Principle

The parameters of interest for neutron storage are the loss probability per wall collision, the depolarization probability per wall collision and the Fermi potential.

The Fermi potential V_F depends on the bound coherent scattering length of the nuclei of the material and their density. It can be obtained by using neutron reflectometry or transmission of UCN through a foil, as it is shown in sec. 9.5. This property can also be measured using methods that do not use neutrons. This is the subject of ongoing work at PSI [72].

The loss and depolarization probabilities are measured using stored UCN.If neutrons are stored in a volume, they undergo many collisions with the walls of the storage volume. For the measurement of any interaction that occurs during wall collisions it is necessary to find out the number of wall collisions per time and area, ν. This is not experimentally accessible in our experiment and calculated by Monte Carlo simulations using GEANT4, as it is described in sec. 3.

Materials used for the storage of UCN are highly reflective for such particles, but there is still a small probability to loose a particle on a wall collision due to absorption, mechanical slits or surface defects. Especially mechanical slits in the storage volume can contribute significantly to the wall losses. Originating from incoherent scattering effects during a collision also the spin orientation of the stored UCN relative to an external magnetic field can change. Our approach to determine the loss and depolarization probability experimentally is to use a trap consisting of a vertically mounted sample tube, with the surface which should be investigated on the inside. Technologically it is favorable to reduce the surface to a simple geometrical shape, e.g. a tube, which can be produced almost perfectly. The tube is "closed" on the top by gravity and on the bottom by a magnetic field.

The idea of using a magnetic field for the confinement for neutrons goes back to Vladimirski [73], the first experiment was performed by Abov (1976) [74][1], it was further developed by Kosvintsev et al. [75]. Magnetic storage is based on the force on a neutron caused by a field gradient

$$\mathbf{F} = \pm\nabla(\mu \cdot \mathbf{B}) \tag{5.1}$$

with the neutron magnetic moment μ.

The magnetic field can be switched on and off and is so used as a shutter. The neutrons are filled through this shutter when the field is turned off. After filling to an equilibrium number of neutrons, the magnet is turned on and a detector is counting all neutrons below the magnet. Neutrons that can pass through the magnetic field (1.5 T = 90 neV) have either the "wrong" (parallel) orientation of the magnetic moment relative to the magnetic field or have too much energy to be reflected, i.e. $E_{\|B} > \pm\mu|\mathbf{B}|$. Figure 5.1 shows the track of a stored neutron. Storage in traps for long times is based on the adiabatic condition as it is discussed in

[1] The work was not published in english before 1986

sec. 2.2. The stored neutrons are perfectly polarized. Below the magnet a mechanical switch is mounted to allow for switching between the feeding neutron guide for filling the volume and the detector for counting neutrons that fall through the magnetic shutter.

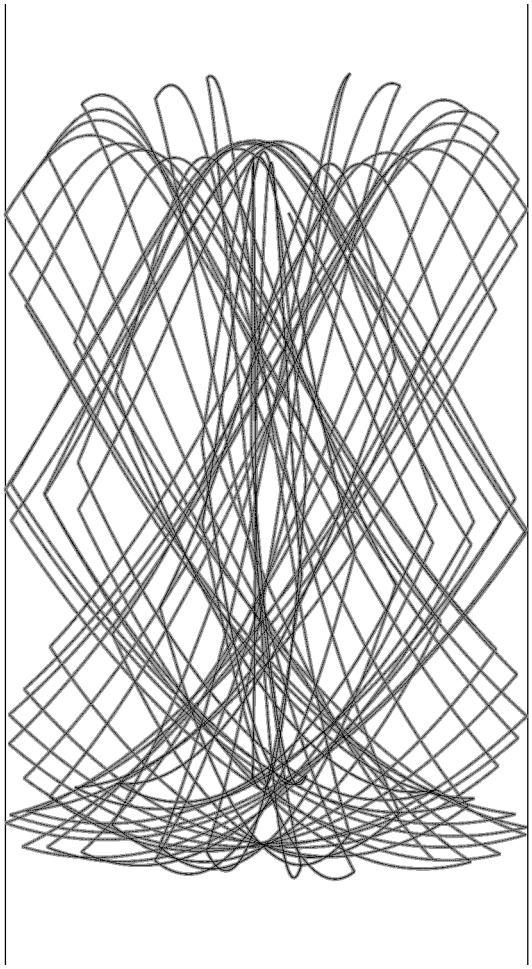

Figure 5.1:
The trajectory of a stored UCN in a storage tube. For the illustration the particle is only specularly reflected from the walls.

The loss probability μ per wall collision determines the time a neutron can be stored in an experiment. This value is therefore important to know and should be as small as possible for most applications. In a real situation the loss probability is very often dominated by mechanical slits or edges. From eq. 2.20 we know that the parameter depends on the loss coefficient η, which is not energy dependent and depends on the bound coherent scattering length and the temperature dependent loss cross section of the material. In fig. 5.2 the loss probability for $\eta = 1 \cdot 10^{-4}$ is shown in dependence of the energy. The shaded region shows the range from 0 to 83.4 neV, which used for our measurements. The low energy limit of the spectrum is determined by the magnetic field barrier, which is different for each field level used for the measurements, as it is discussed in sec. 6.

For the measurement of the depolarization parameter we assume that the spin flipped neutrons do not change their energy significantly due to energy gain on the surface[2], so that

[2]Of course, inside the field the potential energy is changed by changing the sign in the Hamiltonian.

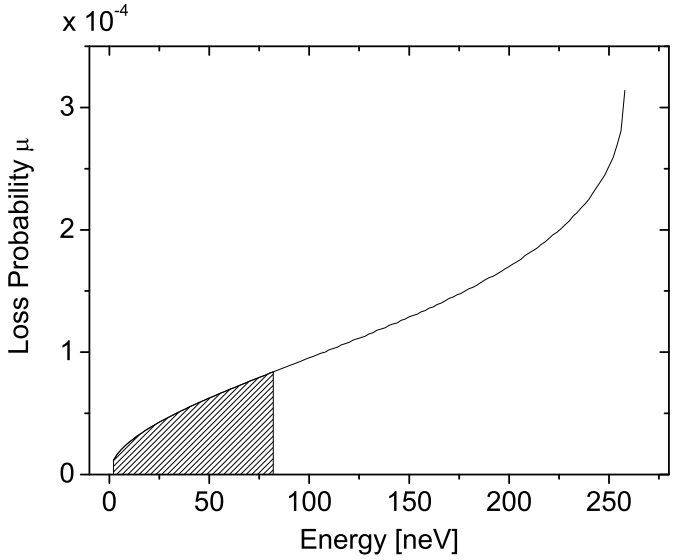

Figure 5.2:

The loss probability as a function of the energy of the neutron for a fixed value of $\eta = 1 \cdot 10^{-4}$. The distribution is valid for the case of random angles on wall collisions. The shaded region is the region addressed by our experiment.

they can be counted in the detector. By comparing two different measurement methods we can check on possible systematic effects. The two different methods to measure the loss coefficient η and the depolarization probability per wall collision β are described in the following.

5.1 Storage Method

The storage method allows for the determination of both parameters, η and β, by storing neutrons for different times t_1 and t_2 inside the sample volume. The principle of the measurement is shown in fig. 5.3. In the left picture the experiment is filled. During filling neutrons enter the storage volume, and leave the volume again at the top or at the bottom. After a short time an equilibrium neutron density of entering and leaving neutrons inside the storage volume is reached. Then the magnetic field is turned on and one spin component is stored. Only neutrons that are too fast or have the wrong spin relative to the field lines escape, as shown in the middle picture. To count the neutrons that were stored for a time t_i, the field is turned off and the neutrons fall into the detector. By performing this experiment with two different times, t_1 and t_2, one can determine the storage time.

$$\tau_{tot} = \frac{t_2 - t_1}{\ln(N_1/N_2)} \tag{5.2}$$

In sec. 9.1.2 the approach to derive the storage time exponent by knowing only two points is investigated in more detail by measuring storage curves with more points. From the storage time in the bottle we calculate the loss coefficient. The numbers N_1 and N_2 correspond to the number of stored neutrons at the times t_1 and t_2. If a neutron is absorbed or up-scattered on a wall collision it is lost from the volume. In the case of a spin flip it falls down through

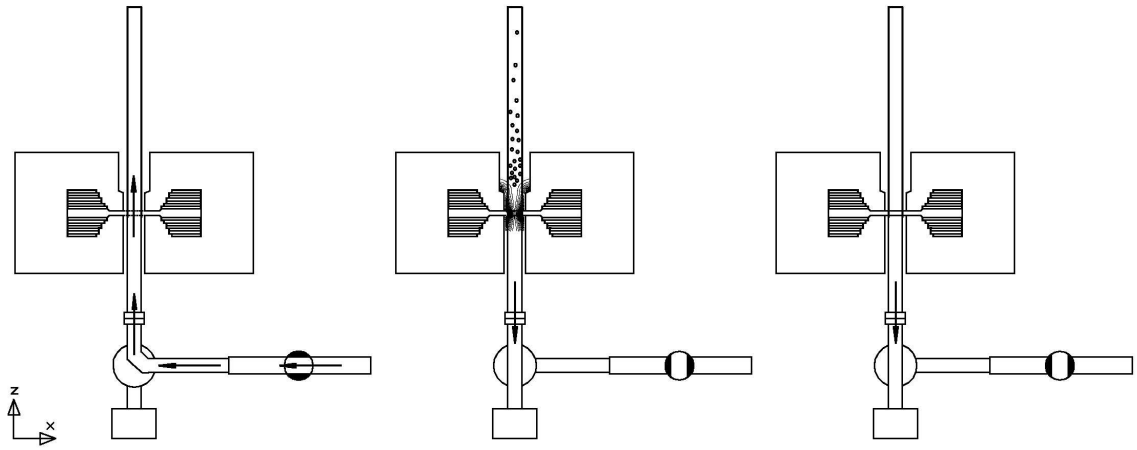

Figure 5.3:

Storage method. Left: the magnetic field is turned off, the switch is in filling position and the shutter is open. Middle: the field is turned on, the neutrons are trapped. The shutter is closed, the switch is in emptying position. Right: the field is turned off and the neutrons are counted in the detector.

the magnetic barrier in the detector and is therefore also lost from the storage volume. The storage time in the tube is based on the neutron lifetime τ_n, the wall reflection losses and the losses caused by spin flips on wall collisions:

$$\frac{1}{\tau_{tot}} = \frac{1}{\tau_n} + \frac{1}{\tau_\mu} + \frac{1}{\tau_\beta}. \tag{5.3}$$

The inverse loss-time $1/\tau_\mu = \nu \cdot \mu$ consists of the loss probability μ and the wall reflection frequency ν. Losses originating from from spin flips are described by $1/\tau_\beta = \nu \cdot \beta$, where β is the depolarization probability per wall collision. This is valid for one single neutron energy, where the influence of gravity on the wall reflection frequency is neglected. The number of spin flipped neutrons is

$$\frac{dN_{sp}}{dt} = N(t) \cdot \nu \cdot \beta. \tag{5.4}$$

By integrating this formula between time t_1 and t_2 we get the depolarization probability β:

$$\beta = \frac{N_{sp}}{\tau_{tot} \cdot \nu \cdot (N_2 - N_1)} \tag{5.5}$$

with the number of spin flipped neutrons N_{sp} defined as the number of neutrons falling through the magnet between t_1 and t_2, N_1 and N_2 the corresponding number of neutrons.

5.2 Complementary Method

In the complementary method, spin flipped neutrons are accumulated in the sample by filling through the magnetic field, as shown in fig. 5.4. Neutrons with one spin component can pass the field barrier, whereas the second spin component is reflected from the field. Neutrons that pass the barrier make wall collisions inside the storage volume. If they undergo a spin flip there, they are trapped by the magnetic field. If their kinetic energy is smaller than the field barrier, they cannot escape from the bottle any more and can be stored for a long time.

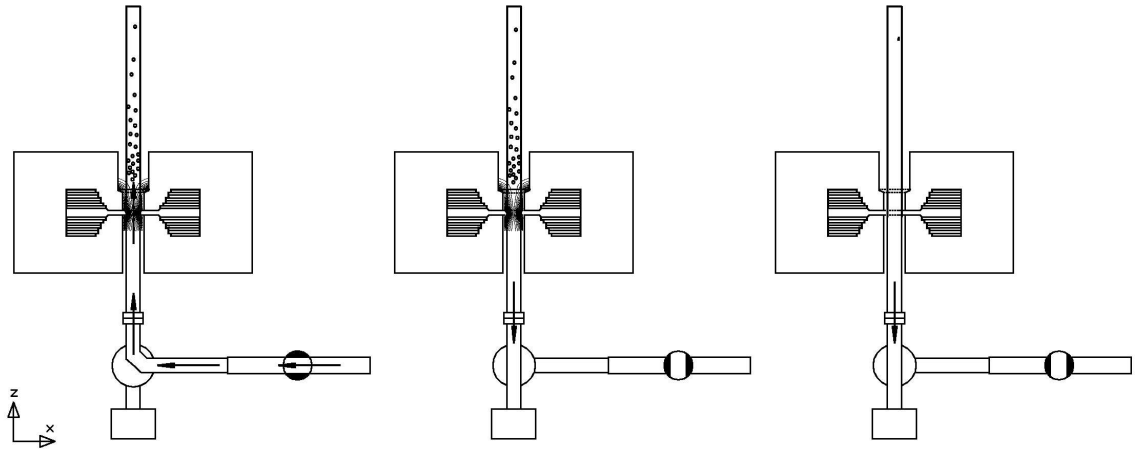

Figure 5.4:

Complementary method. Left: the field is turned on, and neutrons are filled through the field. Spin flipped neutrons are accumulated. Middle: the shutter is closed, the switch is in emptying position. Right: the field is turned off and the trapped neutrons are counted.

By exposing this system to the neutron beam for e.g. 100 s, trapped neutrons can be accumulated and an equilibrium will be reached. The equilibrium results from losses due to the β decay, wall collisions and depolarization. The mathematical description for this problem is similar to a radioactive decay with a daughter product

$$N_{sp}(t) = R^{+} \cdot \tau_{tot} \cdot (1 - e^{-\frac{t}{\tau}}) \tag{5.6}$$

where τ_{tot} is the storage time as it is measured using the storage method. The time t is the time used for accumulating spin flipped neutrons. The production rate

$$R^{+} = N_0^{*} \cdot \nu \cdot \beta \tag{5.7}$$

depends on the number of neutrons in the storage volume N_0^{*}, which is a equilibrium number based on the incident neutrons from the guide and the neutrons that fall down or escape on the top. The parameter ν is the wall collision frequency for one energy and β the depolarization probability.

5.3 Measurement Cycle

The measurement procedures are repeated consecutively under similar conditions to gain statistical accuracy. The number of stored neutrons per measurement cycle ranges from about 200 after 120 s of storage, up to 640 for DLC coated PET-foil after 120 s, depending on the geometry and the storage properties of the sample. Therefore, all data shown consist of a sum of runs, which are either shown integral or averaged.

Each run starts with a signal to open the beam line shutter. This signal triggers the start of the detector readout. All other commands used in one measurement cycle are performed with a time delay relative to this trigger. The error on the reproducibility of the measurement procedure is less than < 0.1 s and thus has only a negligible effect on the error estimation.

In order to determine the energy dependencies of β and η, measurements were performed at different magnetic field strengths, corresponding to different limiting energies. Using this

data, a differential energy spectrum $g(E)$ of the neutrons that are stored can be determined. This spectrum acts as a weight function for the analysis. Also the wall collision frequency $\nu(E,h)$ depends on the energy of the particle and due to gravity also on the height in the bottle. The calculation of the parameters $g(E)$ and $\nu(E,h)$ is shown in chapter 6.

A detailed description of the measurements and the analysis are shown in chapter 7, which deals with the determination of the loss coefficient η using the storage method. Chapter 8 describes the two methods of determining the depolarization probability per wall collision β.

Tests on other small effects which could be of concern for the storage time, as e.g. small energy increase of the neutrons during storage, are shown in sec. 9.3. Neutron spin reorientation in low field regions, which is referred to as Majorana transitions [76], has been investigated by changing and reversing the current in the holding field coil. This effect is also small, a further investigation of this issue is described in sec. 9.3.1.

5.4 Optimization of Working Parameters

For the operation of the experiment some parameters have to be optimized:

5.4.1 Filling

The neutron shutter at the turbine exit is opened and the switch is put to fill position. During this process the magnet is turned off, so neutrons can freely enter and exit the sample volume. In a few seconds an equilibrium density is reached due to a balance of the incident neutron flux with neutrons that escape on the top or on the bottom, or are absorbed. The time until an equilibrium is reached inside the bottle was measured by varying the time from opening the beam line shutter to ramping up the field. The time dependence is shown in fig. 5.5. The neutrons are stored for the same time and then counted in the detector. An equilibrium of neutrons is reached 15 s after the beam line shutter is opened and thus a fill time constant of 15 s was chosen for all measurements. The mirror inside the neutron switch, which is made of polished stainless steel, cuts the spectrum of the upwards reflected neutrons due to the Fermi potential of stainless steel (194 neV). The influence of a different upper energy cut-off of the initial spectrum on the stored spectrum is shown in sec. 9.1 and is not relevant for our experiment.

5.4.2 Closing the Magnetic Valve

After an equilibrium density in the volume is reached, the magnet current is turned on and at the lower end of the sample a magnetic field barrier of up to 1.52 T in the geometrical center z = 0 and r = 0 of the tube is raised with a ramp of 3 s. A field strength of $|\mathbf{B}| = 1.52$ T causes a field barrier of $\mu_N \cdot |\mathbf{B}| = \pm 91.67$ neV. During the ramping of the field the neutrons gain energy. In order to count neutrons passing the magnetic valve, the switch is moved to the "counting" position after the field reaches its maximum value. The beam line shutter is closed at the same time to avoid neutrons from the turbine leaking through the switch into the detector.

The influence of the magnetic field depends on the different velocities of neutrons passing the field region while the field changes. Slower neutrons increase their energies more than faster ones.

In the simulation shown in fig. 5.6, the situation is simplified compared to the realistic situation: Neutrons are produced homogeneously distributed over a horizontal plane at z = -100 mm below the magnetic field maximum inside the feeding guide. The momentum distribution is calculated by using a linearly rising distribution of the velocity in upward z direction

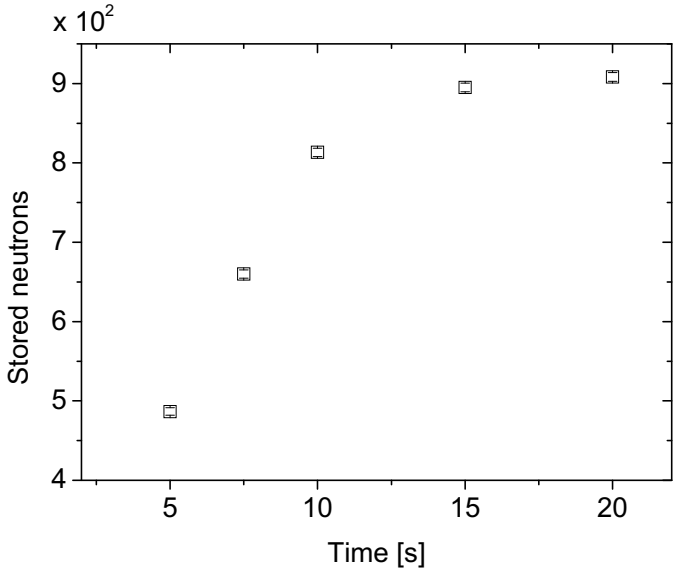

Figure 5.5:

The number of stored neutrons as a function of filling time. The storage time after filling was 50 s.

and a radial velocity component with a flat probability distribution from $-5.8\,\mathrm{m/s}$ to $5.8\,\mathrm{m/s}$, corresponding to approximately the limiting velocity of the neutron guide. The number of wall reflections per time is high compared to the time the neutron spends inside the storage tube. This makes the simulation insensitive to diffuse or specular reflection probabilities, as long as this is non-zero. For our simulation a diffuse scattering probability of 7 % was chosen.

In the simulation used in the analysis, the magnetic field is approximated by using the measured values of the field at the z-axis at $r = 0$ and calculated values at $r = 20\,\mathrm{mm}$ and $r = 35\,\mathrm{mm}$, and interpolating the values in between. The ramping of the field is simulated linearly, which is in agreement with the measured ramp (see fig. 4.13). The simulated energy gain as a function of energy and ramping time for different neutron energies is shown in fig. 5.6. In this simulations neutrons are produced 100 mm below the field maximum. The energy is normalized to $z = 0$, which corresponds to the position of the maximum field. The energy shift for energy 0 would be exactly the minimum potential which is possible in the storage volume when the magnet is turned on.

5.4.3 Magnetic Cleaning

Directly after the magnetic shutter is switched on, the spectrum of stored neutrons consists of both spin components and many neutrons with kinetic energies significantly higher than the energy necessary to pass the potential barrier of the magnetic field. The neutrons with the direction of the magnetic moment oriented parallel to magnetic field lines escape with a time constant of about 2 s. The anti-parallel component is stored and after a very short time the neutron ensemble is perfectly polarized. The neutrons that are too fast are - depending on their energy - still stored and escape only slowly, since for the transmission of the field only the velocity component parallel to the field lines is relevant. The time constant for loosing

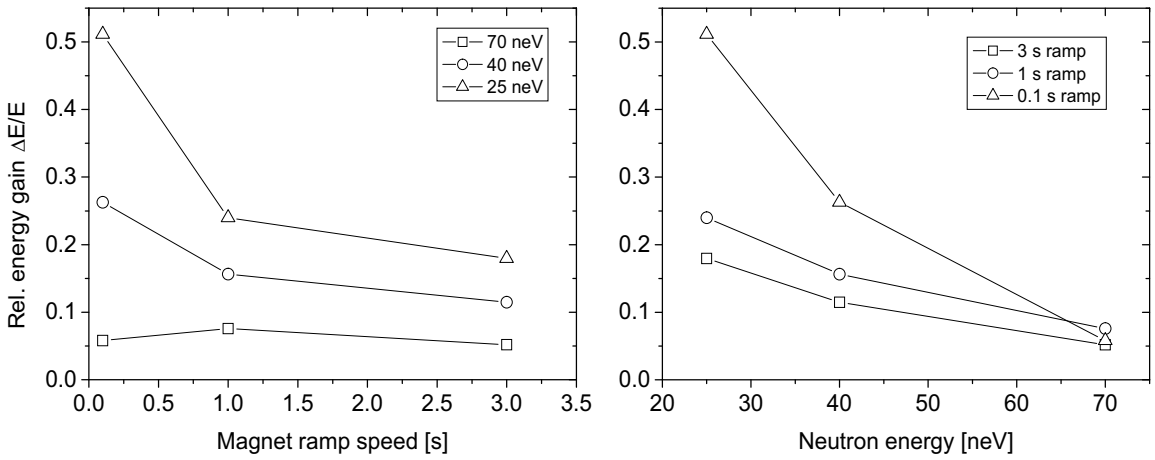

Figure 5.6:

The energy gain caused by the magnet ramp. In the left picture the energy gain for different initial energies in dependence of the ramping time is shown, in the right picture the data is plotted to show the energy gain as a function of the neutron energy. The lines are to guide the eye.

these neutrons is in the order of 200 s, which is too long for our purpose and would still not guarantee that we do not have single "wrong" neutrons that escape with a long delay during the measurement. To improve on this, a "cleaning" procedure is introduced. For this we raise the field in the beginning only to 90 % of the value during storage to make it easier for the faster neutrons to escape. After 100 s the field is raised to 100 %. This assures that the energy of the stored neutrons is lower than field barrier. The exact numbers of this procedure have been determined by Monte Carlo simulation and verified experimentally. As an illustration the loss channels from the storage volume for a simplified field configuration directly after filling are shown in fig. 5.7, where the loss per time from the storage volume is shown on a logarithmic scale. The total curve is split into regions denoting the different loss channels. The loss channels from the bottle are

1. Escape on the top. Neutrons with a velocity component in vertical direction higher than the sample height have a possibility to leave the volume on the top. The sample height is 1080 mm, corresponding to a kinetic energy of 108 neV. Only neutrons above this energy can escape through this channel.

2. Escape through the magnetic field. Neutrons with a velocity component in vertical direction downwards higher than the critical velocity caused by the field barrier leave the volume on the bottom.

3. Wrong spin. If neutrons with a spin anti-parallel to the field lines enter the volume, they can transmit the field and will therefore also leave the volume easily and very fast. This is only visible in the very first time bins.

4. Loss on wall collision. Wall losses are mainly caused by thermal up-scattering and nuclear absorption. In both cases the neutron is not stored any more.

5. Neutron β decay. The neutrons decay with a lifetime of 885.7 s [77].

6. Depolarization on wall collision. When the spin is flipped at a wall collision the neutron can leave the volume through the magnetic field barrier and will not be stored any more.

7. Spin reorientation on low field transitions. When the adiabatic condition (cf. eq. 2.38) is not fully preserved, the neutron can re-orient its spin relative to the magnetic field lines with a non-zero probability. In the simulation this is neglected. Experimentally the holding field prevents such regions well enough and this effect can be neglected.

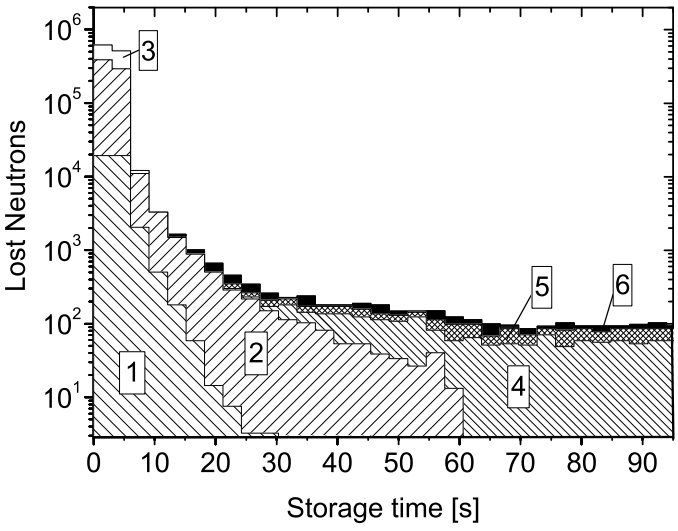

Figure 5.7:

Simulation of losses from the bottle originating from different loss processes. The graph shows the time after filling on the x-axis and the number of neutrons leaving the volume. In this simulation after 60 s the field is raised from 90 % to 100 %. For a detailed description see the text.

In the experiment we chose a cleaning time of 100 s, which is on the safe side. Experimental tests on this time constant and a comparison with the Monte Carlo simulation of this realistic situation is shown in sec. 9.1, which is also a stringent test for the Monte Carlo simulation.

5.4.4 Storage

When the field is raised to 100 % the neutrons are stored for about 20 s to show that there are no counts of "wrong" neutrons in the detector any more. All counts that can be observed in the detector from this time on, are neutrons that have changed the orientation of their spin in the field. The storage time can be varied with different measurements to get an exponential decay curve of the stored number of neutrons. The decay curve is based on the losses caused by the decay of the free neutron, the loss probability per wall collision and the spin flip probability per wall collision.

5.4.5 Emptying

In order to count the number of stored neutrons in the bottle the field is turned off with a ramp of about 2 s to 5 % of its former value. The neutrons fall into the detector and are

counted. The efficiency of the detector cancels out for the calculation of the storage time. The magnet time constant for emptying is $\sim 2\,s$. However, in practice it turned out that for a part of the neutrons it takes much longer that a neutron is counted due to (i) the reflectivity of the vacuum separation window with the stainless steel support structure, (ii) the detector entrance window, (iii) diffuse reflections in the feeding guide tube that prolong the track of the neutron. The vacuum separation foil is mounted 600 mm below the magnetic field maximum and has a Fermi potential of 54 neV. The window of the detector is made from 100 μm Aluminum with a Fermi potential of also 54 neV. The distance in height between the magnetic field maximum and the detector window is 922 mm and so the reflectivity is according to eq. 2.14 8 % for a neutron with 180 neV at the window position and 18 % for a neutron with 100 neV, which explains the delayed counts in the emptying peak.

5.4.6 Background Measurement

A background measurement follows each emptying procedure of the bottle consecutively. Depending on the time when - per definition - emptying is finished and the background measurement starts, the "background" rate changes, and reaches a stable low level for emptying times $> 40\,s$. A time behaviour of the background after the variation of the emptying time is shown in fig. 5.8 (left). For the analysis the emptying time was even set to 60 s. To get a stable result for the background rate, the background was measured additionally in long runs directly after and before a sample change. The background runs were done during the whole reactor cycle and give an average of $4.8 \pm 0.3\,mHz$. As it can be seen in fig. 5.8 (right) the countrate was stable during the whole reactor cycle. The beam line shutter was closed and the switch was moved in "empty" position, to assure similar conditions as during the time for N_{sp} counting in the storage method measurements.

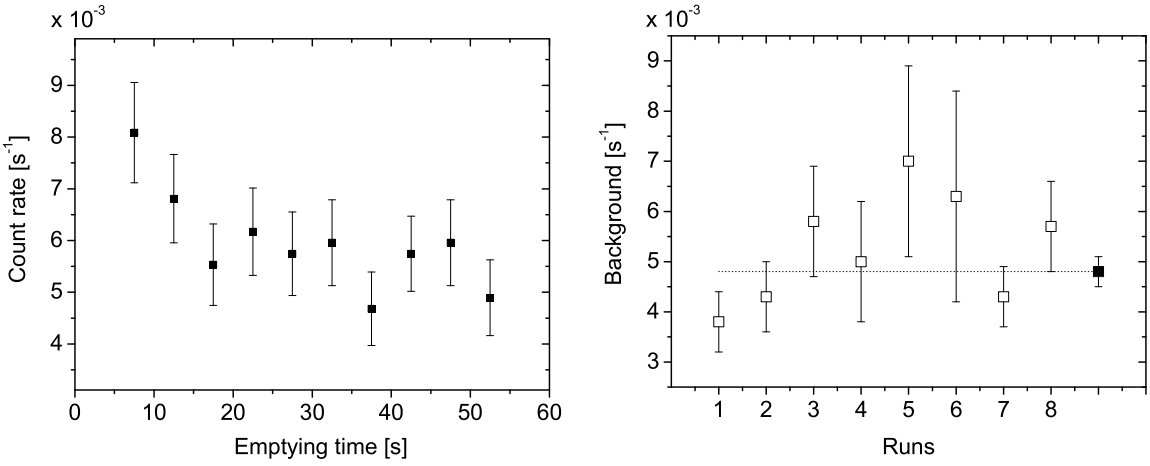

Figure 5.8:

Left: emptying times. Directly after the emptying of the experiment a background run was attached. Depending on the time after emptying the count rate during the background measurement changes. Right: background runs spread over the whole reactor cycle. The shielding has been readjusted a view times in between. The background seems to be reasonably stable during all this time and we take the average value (last point) as a mean background of $4.8 \pm 0.3\,mHz$.

5.5 List of Measurements

A list of measurements which were used for the analysis is shown in tab. 5.1.

Sample	Institute	Measurement	T [K]	Cycles
Be on Al-tube	PNPI	Storage method	300	270
		Storage method	380	124
		Complementary method (1 step)	300	164
		Complementary method (1 step)	380	44
		Complementary method (2 steps)	300	208
		Fill time tests	300	37
		Magnet ramping	300	74
		Holding field tests	300	28
Be on Quartz-tube	PNPI	Storage method	300	114
		Complementary method (1 step)	300	38
Be on Al-tube	TUM	Storage method	300	84
		Complementary method (1 step)	300	120
		Long storage without cleaning	300	90
		Long storage with cleaning	300	52
DLC on Al-tube	VT	Storage method	300	70
		Complementary method (1 step)	300	100
DLC on PET-foil # 1	IWS	Storage method	300	48
(measured in May)		Complementary method (1 step)	300	16
DLC on PET-foil # 1	IWS	Storage method	300	22
(measured in June)		Complementary method (1 step)	300	9
DLC on Al-foil	IWS	Storage method level 0-4 = Energy spectrum	300	144
		Complementary method (1 step)	300	45
		Cleaning time variations	300	25
		Cooling	300 - 70	66
		Storage method level 0-4 = Energy spectrum	70	85
		Complementary method (1 step)	70	30
DLC on PET-foil #2	IWS	Storage method level 0-4 = Energy spectrum	300	100
		Complementary method (1 step)	300	30
		Long storage without cleaning	300	180
		Long storage with cleaning	300	44
		Low energy heating tests	70	14
		Cooling	300 - 70	142
		Storage method level 0-4 = Energy spectrum	70	90
		Complementary method (2 steps)	70	75
		Low energy heating tests	70	14

Table 5.1:

List of all performed measurements. The parameter T is the sample temperature, cycles the number of repetitions of the individual measurements. No background runs are listed.

Chapter 6

Stored Neutron Spectrum

A proper knowledge of the spectrum of stored neutrons is necessary for an energy dependent analysis. The idea of the measurement is that different magnetic field strengths allow for the storage of spectra with a different energy range. The exact determination of these spectra is strongly related to Monte Carlo simulations.

6.1 Simulation of the Spectrum

In the simulation using the GEANT4-UCN package (see sec. 3), it is assumed that neutrons enter the storage volume of the experiment with a linearly rising velocity distribution in upward vertical direction from 0 to 15 m/s and a flat distribution from -5.8 m/s to 5.8 m/s in radial direction. In the energy range used in our experiment this distribution produces a spectrum that is almost linear in energy. The initial distribution of the velocities is not critical due to the diffuse scattering properties of the walls and the long storage times compared to the reflection frequencies. During the first 100 s after filling, the energy spectrum inside the volume develops is formed with respect to the loss channels (see sec. 5.4.3). The resulting energy spectrum is almost linear in energy.

The average energy stored in each spectrum can be roughly estimated from the upper limit of the spectrum given by the field of the magnetic shutter during the cleaning procedure. This limit can be determined more accurately with the simulation. A small correction to the value of the average energy of the integral spectra, as well as for the bin widths for the differential spectrum is deduced. The lower energy limit is given by the lowest possible energy inside the magnetic bottle. The energies for the different field levels which were used for cleaning and during storage are shown in tab. 6.1.

Magnet Level	$\mathbf{B}_{cl}$**[T]**	**B [T]**	$\mathbf{E}_{cl}$ **[neV]**	**E [neV]**	$\mathbf{E}_{av}$ **[neV]**	$\mathbf{E}_{min}$ **[neV]**
0	1.39	1.52	83.41	91.31	66.50	28.9
1	1.30	1.39	77.76	83.41	59.85	26.6
2	1.16	1.25	69.59	74.84	53.80	22.9
3	1.00	1.08	60.01	64.68	46.20	17.5
4	0.82	0.90	49.30	54.14	37.77	13.2

Table 6.1:

Magnetic field levels used for the measurements during cleaning and storage.

The level number is used to describe the measurements in the following, B_{cl} is the magnetic field barrier during the cleaning time, E_{cl} the corresponding energy, which is similar to the maximum energy that is stored, E_{av} the average energy of the spectrum and E_{min} the minimum potential which is possible after the magnetic field is switched on. The lower energy limit E_{min} of the spectrum for each level results from the field distribution as it is shown in fig. 6.1.

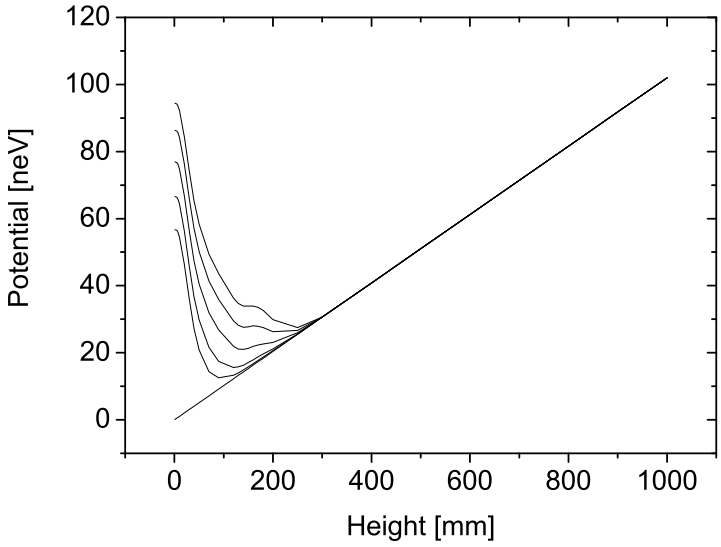

Figure 6.1:

The potential energies in the bottle depending on the height for different field levels (0-4 from tab. 6.1) during storage, as they were used in the simulation. The uppermost curve corresponds to the maximum magnetic field (level 0). In the lower region the potential is mainly determined by the magnetic field. The gravitational potential rises linearly with height (lowest curve).

The potential energy in the bottle consists of the magnetic and the gravitational field. In the experiment, five different magnetic field levels were chosen. For lower field strengths this potential is almost homogeneous for different radii. At high currents the iron gets saturated and the field outside increases. The potential as it is seen by the UCN inside the tubes is shown in fig. 6.2. Positions of low potential energy are blue, high potential energies are red. Neutrons with very low energies can only reach blue areas.

This field configuration is used for the simulation. The field points are entered in arrays of absolute values along the z-axis, for the radii r = 0, r = 20 mm and r = 35 mm. Interpolation between these points is done linearly.

After cleaning, the losses from the trap are caused by wall losses and β-decay. The wall losses are energy dependent and increase for higher energies. The simulated spectra in the bottle after 100 s cleaning are shown in fig. 6.3. The shape results mainly from the incident velocity distribution of the neutrons, the energy shift, which is caused by the magnetic field ramp, the height of the magnetic field barrier during cleaning and the wall losses during 100 s storage. Figure 6.3(a) shows the shape of the spectra normalized to 1, (b) shows the spectra in relation to each other. The shape of these spectra is used for the determination of the differential spectra. Figure 6.3(c) shows the differences resulting from the subtraction of consecutive integral spectra, as it is discussed in the following (sec. 6.2).

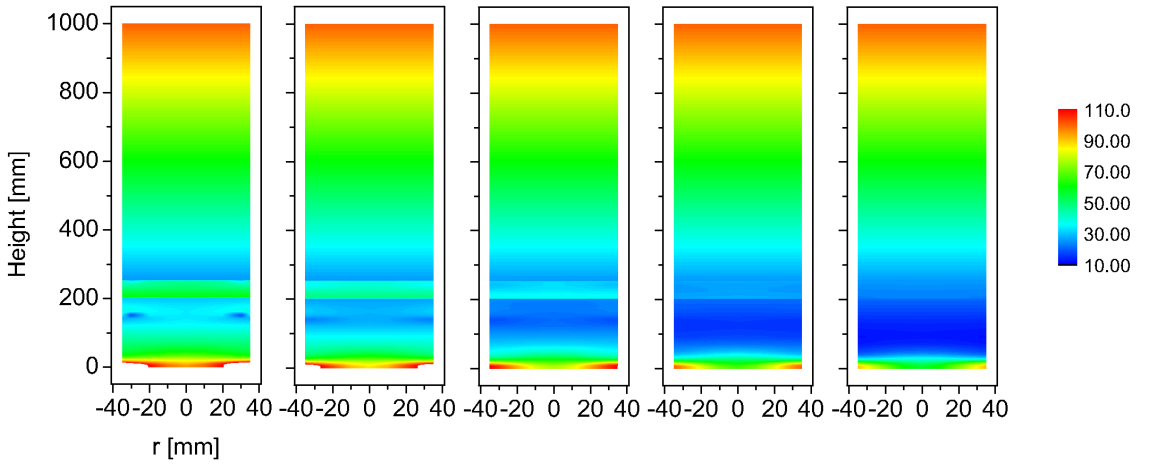

Figure 6.2:

Magnetic and gravitational potential in the bottle for the different field strengths used for the measurements (from level 0 (left) to 4). The potential energy in neV is shown on the scale (right). A vertical cut at r = 0 is shown in fig. 6.1.

6.2 Measured Spectra

6.2.1 Integral Spectra

The integral spectra are shown in fig. 6.4, with the energies taken from tab. 6.1. The measured numbers are directly taken from measurements. For the illustration of the analysis, data from the samples DLC PET-foil #2 at 300 K (left) and at 70 K (right) are used. The open symbols are the raw measurements, the energy is the average energy of the spectrum determined by Monte Carlo. Using the simulated spectra, one can calculate a differential spectrum from the integral spectra. The smaller symbols correspond to the correction (subtraction) for the negative bin contents from fig. 6.3(c). On the energy scale, the points are placed at is the average energy of each spectrum. The error on this position is smaller than the size of the symbol. Black markers represent values measured at totally 120 s storage time, red markers correspond to 320 s.

Energy Dependent Emptying Times

When neutrons, which were stored at level 0, are emptied into the detector, they reach the detector about 1 s faster than neutrons stored at level 4. This is caused by the lower energies of the stored neutrons at lower field strengths. In this one second the neutrons make additional wall collisions. The error on the measurement is linear in time, and small due to the long storage time relative to 1 s ($< 1\,\%$). It is therefore neglected in the analysis of the integral spectrum. In the measurement of the storage time, this error disappears.

6.2.2 Differential Spectra

The differential spectra can be calculated by subtracting the values of the simulated spectra at different magnetic fields. The difference can become negative for some energy bins, as it can be seen in the simulated spectra in fig. 6.3(c). The area of the individual integral spectra is reduced by the part of the area that would become negative. These corrected spectra are then

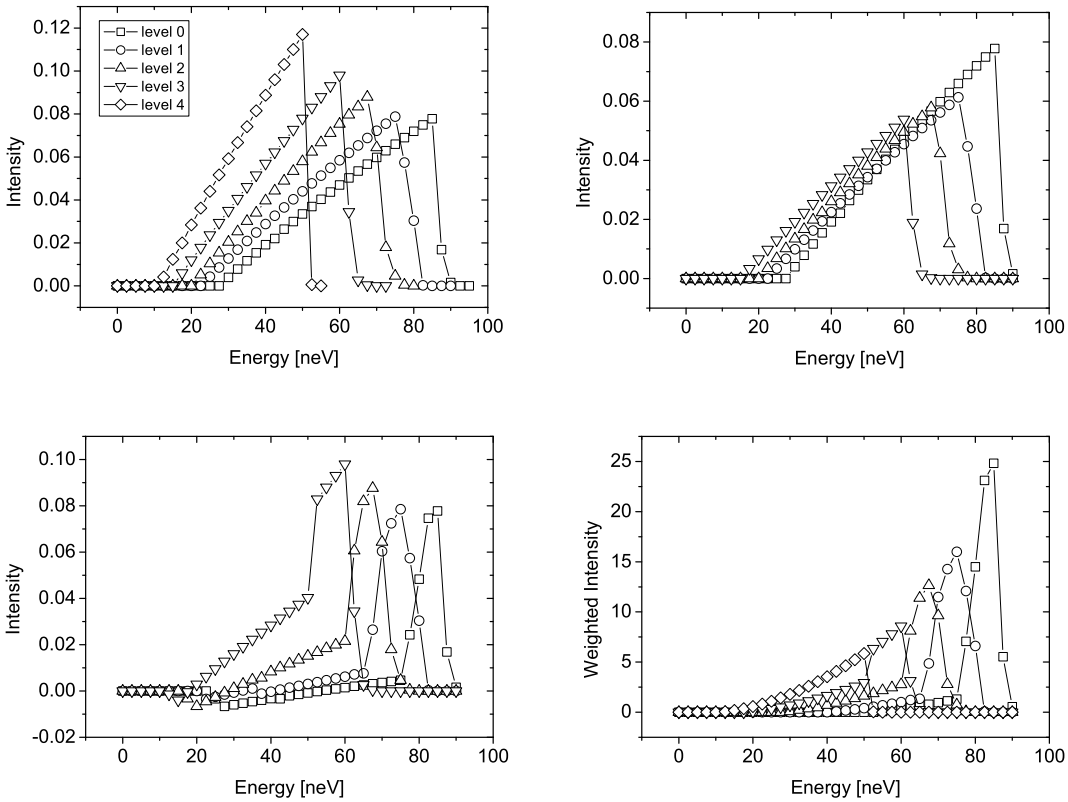

Figure 6.3:

The simulated spectra for the different measurements. The upper left picture (a) shows the spectra normalized to 1, the upper right picture (b) shows the spectra normalized relative to level 0, which has an area equal 1. The lower left picture (c) shows the differences between the spectra, the lower right picture (d) is weighted with the energy. The sum over each curve is the corresponding average energy of each difference, where the lowest energy step is simply the level 4 spectrum.

subtracted. The negative bins result from the fact that the lowest possible energy depends on the field strength used for storage. The average energies of the differential spectra, determined using the spectra from fig. 6.3(d), and the width of these differential bins are shown in tab. 6.2. The with of the last bin is limited on the lower end by the magnetic potential in the bottle. The low count rate at very low energies makes the analysis relatively insensitive to the exact position of this cut-off.

The differential spectra are shown in fig. 6.5. Each point is the difference of the integral spectra at two consecutive energy levels. The open symbols are the uncorrected differences, the full symbols are determined using the correction of the simulation. The black points correspond to the spectrum measured at 120 s of storage, the red points are measured after 320 s.

In fig. 6.6 the spectra from the measurements and the simulated spectra used for the analysis are compared. Although the individual measured points are already corrected by simulation, the shape of the measured spectrum should still fit to the shape of the simulated spectrum. The simulation curve is not fitted but scaled to fit best by eye for visualization, the area cancels in the analysis due to normalization.

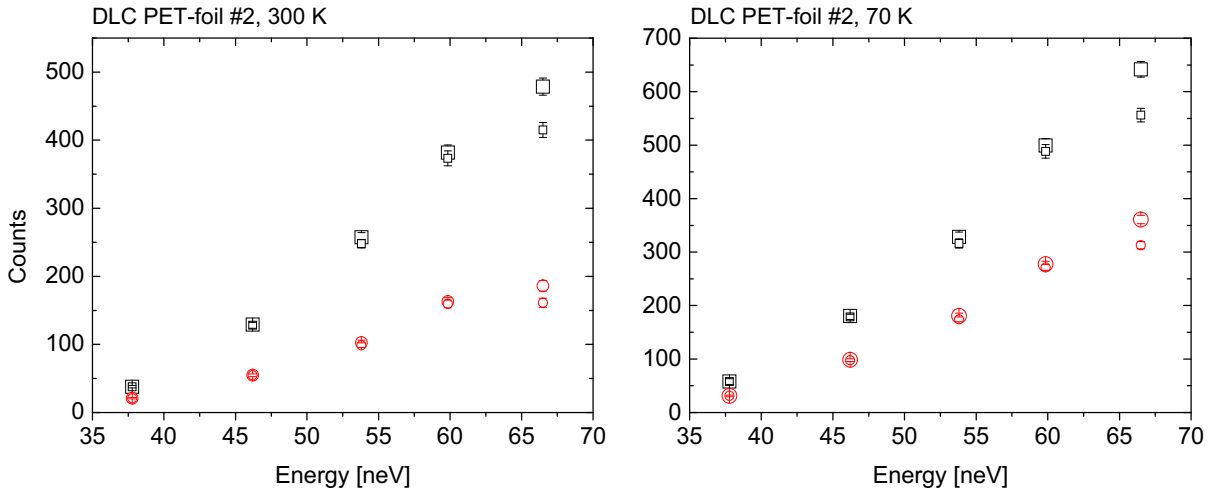

Figure 6.4:

The integral spectra for the DLC PET-foil #2 sample at 300 K (left) and at 70 K. The black symbols refer to 120 s storage time, the red symbols to 320 s. The counts are the average number of stored neutrons per measurement.

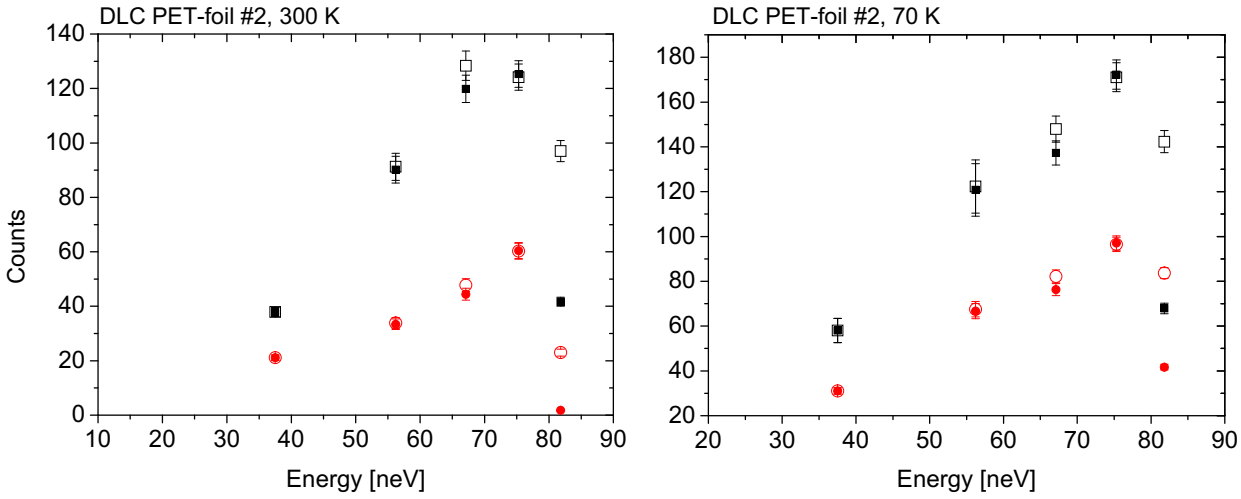

Figure 6.5:

The differential spectra for the DLC PET-foil #2 sample at 300 K (left) and at 70 K. The black symbols denote the measurements at 120 s storage time, the red curves the measurements at 320 s. The open symbols are the measurements without the correction for the negative bins, the filled ones are corrected.

Magnet Level	Bin Width [neV]	E_{av} [neV]
0	5.65	81.8
1	8.18	75.3
2	9.58	67.1
3	10.62	56.2
4	49.39	37.5

Table 6.2:

Bin width and average energy of the differential spectrum steps. The bin width of the last step starts at zero.

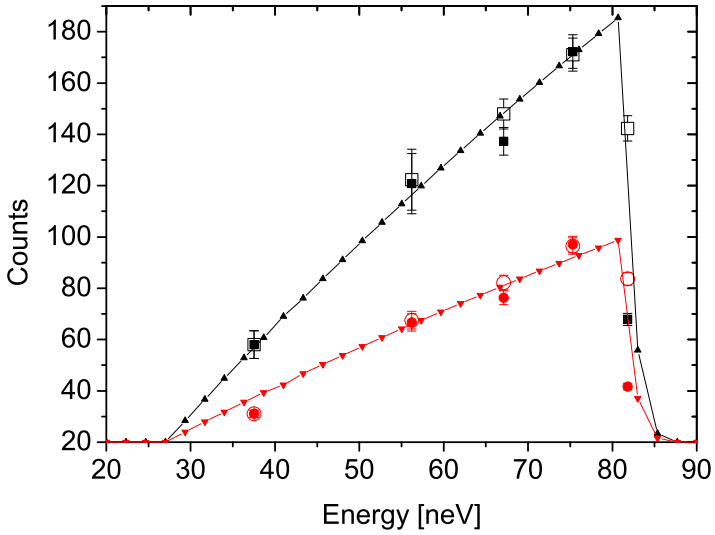

Figure 6.6:

Comparison of the measured differential and the simulated spectra. The triangles are the calculated spectra for 120 s and 320 s, the open squares and circles the uncorrected measurements, the filled symbols the corrected values.

Energy Dependent Detector Efficiency

The efficiency of the detector for different energies (practically) cancels for the measurement of storage times, if we assume that the energy distribution for these measurements stays stable. In the case of spectrum measurements this influences the shape of the spectrum due to the $1/v$-dependent absorption cross section of the Aluminum entrance window of the detector and the higher efficiency of the ^{3}He detector gas. Both effects show an inverse behaviour and a correction on lower energies is less than 2 %.

Chapter 7

Loss Coefficient

The loss coefficient η is determined using the storage method, which is described here in detail. As specified in sec. 5.1, neutrons are stored in the storage volume and after a time t_1 emptied into the detector. The corresponding number of neutrons counted during emptying at t_1 is called N_1. In a second measurement neutrons are again stored and emptied at a later time t_2, corresponding to a number of counted neutrons at this time, N_2. Neutrons that reach the detector in the time between t_1 and t_2 must have made a spin flip, otherwise they could not have passed the field barrier, or they are background counts. These neutrons are referred to as spin flipped neutrons N_{sp}. The time constants used for the measurements are:

Fill time	15	s
Cleaning	100	s
N_1 storage (t_1 - t_0)	20	s
N_2 storage (t_2 - t_0)	220	s

Table 7.1:

Time constants used for the measurement. The storage times for N_1 and N_2 are with respect to the end of the cleaning time t_0.

The storage time of the neutrons in the bottle is

$$\tau_{tot} = \frac{t_2 - t_1}{\ln(N_1/N_2)}. \tag{7.1}$$

The storage time is determined by the lifetime of the free neutron τ_β, the contribution of the wall loss probability τ_μ and the losses caused by depolarization τ_β:

$$\frac{1}{\tau_{tot}} = \frac{1}{\tau_n} + \frac{1}{\tau_\beta} + \frac{1}{\tau_\mu}. \tag{7.2}$$

The losses caused by the decay of the free neutron are known, the present value [77] is $\tau_N = 885.7 \pm 0.8\,\mathrm{s}$, where the error on this value can be neglected in our analysis. The parameters τ_μ and τ_β are unknown. But since the number of spin flipped neutrons N_{sp} and the time label for each of them is known it is possible to estimate a number of neutrons N_2 at time t_2, which is independent on the depolarization, i.e. $\beta = 0$. This assumption is valid for the case that we count all neutrons that make a spin flip N_i at the time t_i. The number of neutrons at t_2 becomes then

$$N_2^* = N_2 + \sum_i N_{spi} \cdot e^{\frac{-(t_2 - t_i)}{\tau_{tot}}} \tag{7.3}$$

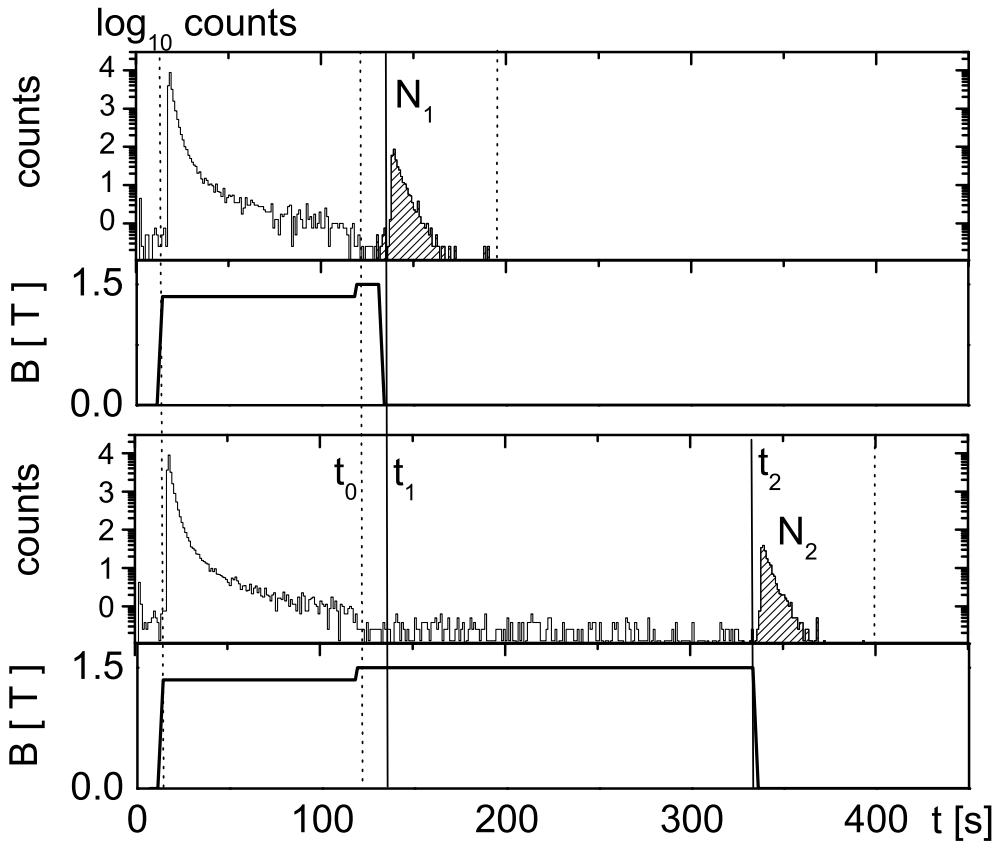

Figure 7.1:

The two necessary measurements are shown. The upper curve is the count rate in the detector, the curve directly below is the magnetic field strength. From time 0 to the first dotted line the experiment is filled, then cleaning starts. Cleaning ends when the field is ramped from 90 % to 100 %. The first measurement is emptied at t_1, the second at time t_2.

where τ_{tot} is the storage time calculated using eq. 7.1. With the new number of neutrons at time t_2 one can calculate a new storage time τ^*_{tot} by using eq. 7.1 again. This new lifetime can be used for eq. 7.3 to estimate a more accurate number of N_2^*. This procedure is carried out iteratively and converges very fast. Now the storage time does not depend on $1/\tau_\beta$ any more. This operation makes only small changes to the storage times, the results are shown in fig. 7.2.

Due to the long measuring times the influence of the background has to be taken into account. The background rate is 4.8 ± 0.3 mHz, see sec. 5.4.6. For 200 s typically 0.96 ± 0.06 counted neutrons are expected[1]. The number of spin flipped neutrons is corrected by the ratio of expected background counts per 200 s to the counted neutrons per 200 s, κ, so eq. 7.3 becomes

$$N_2^* = N_2 + \sum_i N_{spi} \cdot e^{-\frac{(t_2 - t_i)}{\tau_0}} \cdot \kappa \tag{7.4}$$

[1] A discussion on the statistical treatment of such a small count rate is given in sec. 8.1.1

Sample	$\tau_{tot}[s]$	$\tau_{corr,bg}[s]$	$\mathbf{Nsp}_{av}$	$\mathbf{N1}_{av}$	$\mathbf{N2}_{av}$
DLC VT 300 K	157 ± 6.0	161.1 ± 6.0	6.3	321	90
BE TUM 300 K	138 ± 4.5	141.4 ± 4.5	5.7	292	69
BE PNPI AL 300 K	200 ± 11.0	207.2 ± 11.0	10.8	381	140
BE PNPI Al 380 K	176 ± 11.2	180.7 ± 11.2	9	349	112
BE PNPI Quartz 300 K	133 ± 3.7	140.2 ± 3.7	17	262	58
DLC PET 1 May 300 K	316 ± 24.7	332.4 ± 24.7	3	114	60
DLC PET 1 June 300 K	210 ± 28.2	225.6 ± 28.2	1.85	38.8	15
DLC PET 2 300 K level 0	211 ± 15.0	231.5 ± 15.0	32.7	479	186
DLC PET 2 300 K level 1	235 ± 19.8	260.9 ± 19.8	27	382	163
DLC PET 2 300 K level 2	218 ± 14.9	245.6 ± 14.9	21.7	258	103
DLC PET 2 300 K level 3	234 ± 24.6	274.6 ± 24.6	13.2	129	55
DLC PET 2 300 K level 4	364 ± 124	477 ± 124	5.3	38	21
DLC PET 2 70 K level 0	348 ± 59	428.0 ± 59	59.7	641	361
DLC PET 2 70 K level 1	340 ± 65	433.4 ± 65	54.3	499	277
DLC PET 2 70 K level 2	336 ± 79	440.9 ± 79	40.4	328	181
DLC PET 2 70 K level 3	331 ± 72	433.6 ± 72	21.6	180	99
DLC PET 2 70 K level 4	321 ± 205	432.6 ± 205	7.9	58	31
DLC AL Foil 300 K level 0	119 ± 2.3	120.8 ± 2.3	1.7	158	30
DLC AL Foil 300 K level 1	124 ± 4.2	126.6 ± 4.2	2.4	126	25
DLC AL Foil 300 K level 2	140 ± 5.8	146.1 ± 5.8	3.5	81	19
DLC AL Foil 300 K level 3	133 ± 6.2	137.7 ± 6.2	2	52	11
DLC AL Foil 300 K level 4	204 ± 12.9	229.6 ± 12.9	1.1	12.4	4.7
DLC AL Foil 70 K level 0	221 ± 13.5	224.8 ± 13.5	3.8	326	132
DLC AL Foil 70 K level 1	235 ± 21.0	241.3 ± 21.0	4.8	247	105
DLC AL Foil 70 K level 2	206 ± 12.7	215.4 ± 12.7	6.1	176	67
DLC AL Foil 70 K level 3	297 ± 51.0	327.3 ± 51.0	4.9	95	48
DLC AL Foil 70 K level 4	275 ± 58.6	313.1 ± 58.6	2.0	27.8	13.4

Table 7.2:

Measured storage times. The storage time resulting from N_1 and N_2 is called $\tau_{tot}[s]$, whereas $\tau_{corr,bg}$ is the storage time corrected for the number of spin flipped neutrons according to eq. 7.4.

After the correction the new storage time is

$$\frac{1}{\tau^*_{tot}} = \frac{1}{\tau_n} + \frac{1}{\tau_\mu}. \tag{7.5}$$

From this the "loss time" τ_μ can be extracted. The effect on the storage time is shown in tab. 7.2, where also a list of measured storage times and average count rates is given.

For the analysis we assume temporal stability of the conditions. This means similar residual gas pressure, temperature and neutron flux over several hours of measuring. The measured stability of the count rates accumulated in a measurement program over 12 hour is shown in fig. 7.2.

In the measurement not only one energy of neutrons is stored, and therefore the energy dependence of the parameters has to be taken into account. The height changes the kinetic energy of the particles and therefore the energy dependent loss parameter becomes also dependent on the height $\mu(E,h)$. The wall collision frequency $\nu(E,h)$ depends on the velocity of

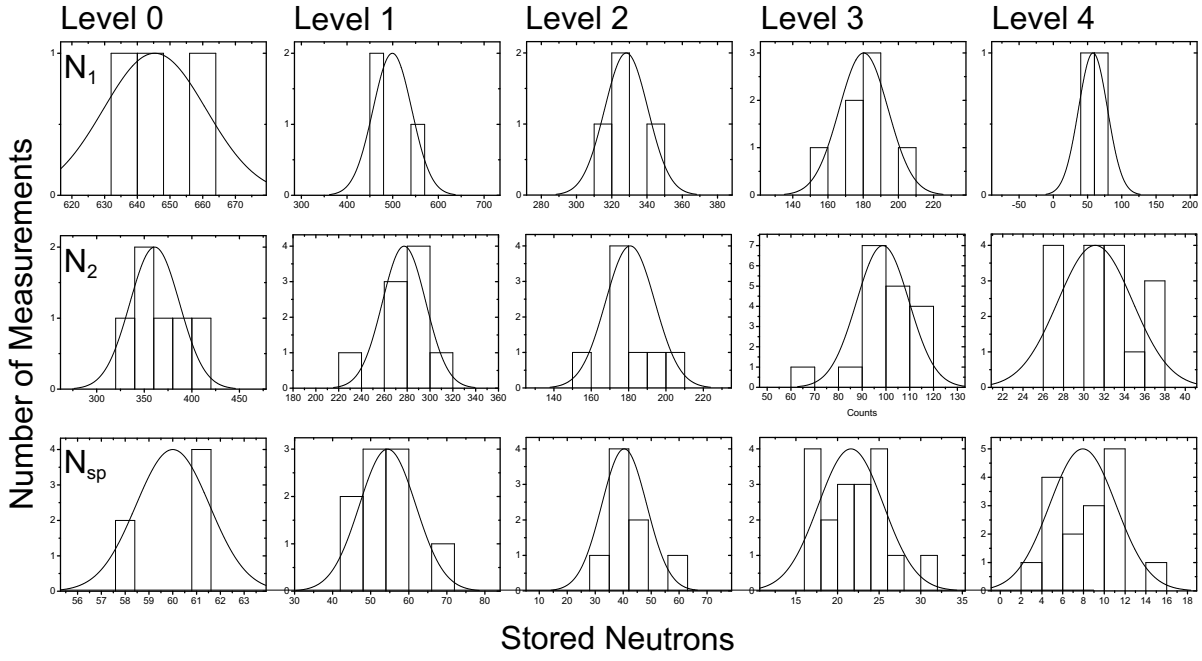

Figure 7.2:

Stability of the measurements. N_1 denotes neutrons counted at time t_1, N_2 at time t_2, N_{sp} the number of neutrons between time t_1 and t_2. The width of the curve gives an idea of the stability of the measurements. The individual measurements are spread over 12 hours. The levels denote the measurements at the different field barriers, as shown in tab. 6.1.

the neutrons, and therefore also on the energy of the neutron and its position in height inside the volume. The magnetic field and gravity always convert part of the energy to potential energy:

$$E_{tot} = E_{kin}(h) + E_{grav}(h) + E_{mag}(h) \tag{7.6}$$

with E_{grav} the gravitational potential mgh and E_{mag} the magnetic potential $\pm\mu|\mathbf{B}|$. For one single neutron energy, the loss becomes:

$$\frac{1}{\tau_\mu} = \int_0^H \nu(h) \cdot \mu(h) dh \tag{7.7}$$

with a normalization so that the integral over $\nu(h)$ is the average wall collision frequency for this energy. This calculation has to be performed for all energies:

$$\frac{1}{\tau_\mu} = \frac{\int_0^E \int_0^{H(E')} \nu(h, E') \cdot \mu(h, E') \cdot g(E') dh dE'}{\int_0^E g(E') dE'} \tag{7.8}$$

The shape of the energy spectrum $g(E')$ is determined in sec. 6, the loss probability per wall collision is based on eq. 2.20, the collision frequency is calculated using Monte Carlo. The calculated distributions of the collisions are shown in fig. 7.3.

The loss parameter per collision is calculated using eq. 2.20, with the loss coefficient η as the parameter that can be varied. The Fermi potential used is 258 neV. The integrals are replaced by sums over height with 1 cm bins and energy with 2.5 neV bins for the numerical solution.

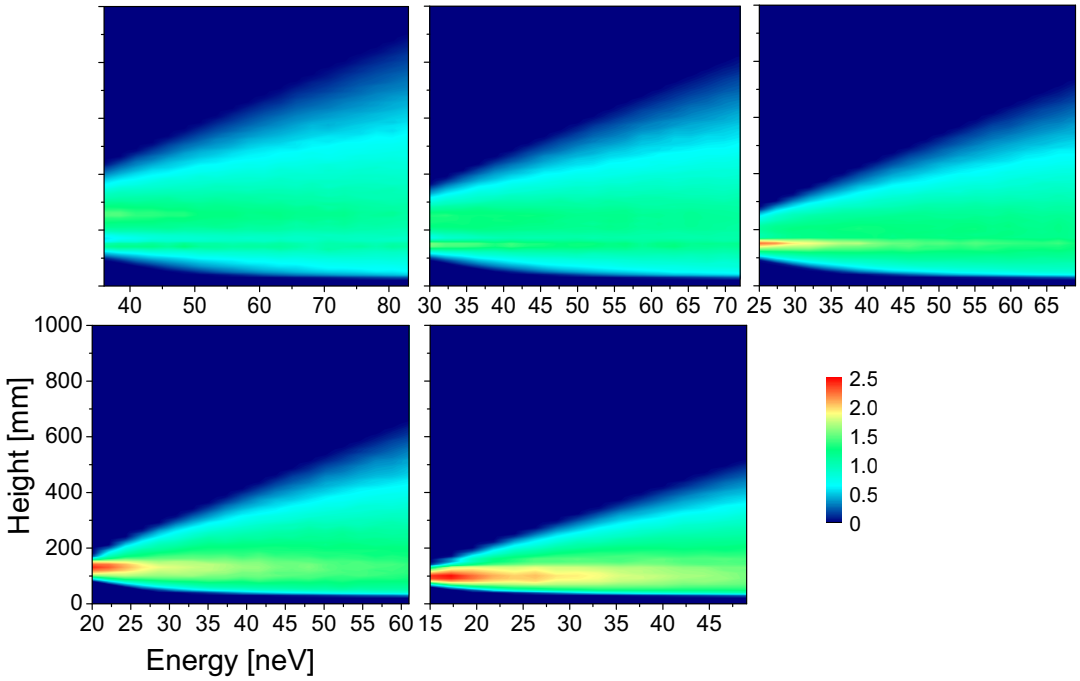

Figure 7.3:

Number of wall collisions per particle per second per cm in height. On the x-axis the total neutron energy is plotted, with a potential energy equal to zero at z = 0 (B-field maximum in z-direction). The upper left graph is for level 0 (see tab. 6.1), the lower right for level 4. Dark blue denotes no collisions, a brighter color represents more collisions. The scale on the right is in units $1/(s \cdot cm)$ per neutron, where cm means cm in height of the volume. For the tube samples this is a ring, for the foil samples this is a more complicated surface, and not easily normalized to $1/cm^2$.

We performed measurements at 5 different magnetic field levels as shown in tab. 6.1 with a level for cleaning at 90 % of the field used for storage. Figure 7.4 shows a set of measurements for the PET foil 2 sample at 70 K. The measurements consists each of a series of N_1 and N_2 runs, which are carried out consecutively under similar conditions (residual gas pressure and sample temperature).

The distribution of the wall collisions (fig. 7.3) results from the simulation of trajectories through the volume. Depending on the kinetic energy of the particles the distribution reaches further up against gravity and deeper into the magnetic potential. In the upper part of the bottle - where the magnetic potential is negligible - the distribution follows the behaviour as expected by kinetic gas theory [18], p. 79. In the lower part of the storage volume the number of collisions is reduced by the potential of the magnetic field, which causes a reduced velocity. The simulation is based on the same calculation as it is used for the determination of the spectrum (see sec. 6.1).

Using the wall collision distribution from the simulation and the loss probability from eq. 2.20, a "loss time" τ_μ can be simulated for a selected η. By doing a simulation for many different values of η, a storage time curve can be calculated for each magnetic field level and for each sample geometry. A set of curves for the DLC PET-foil # 2 sample from level 0 to

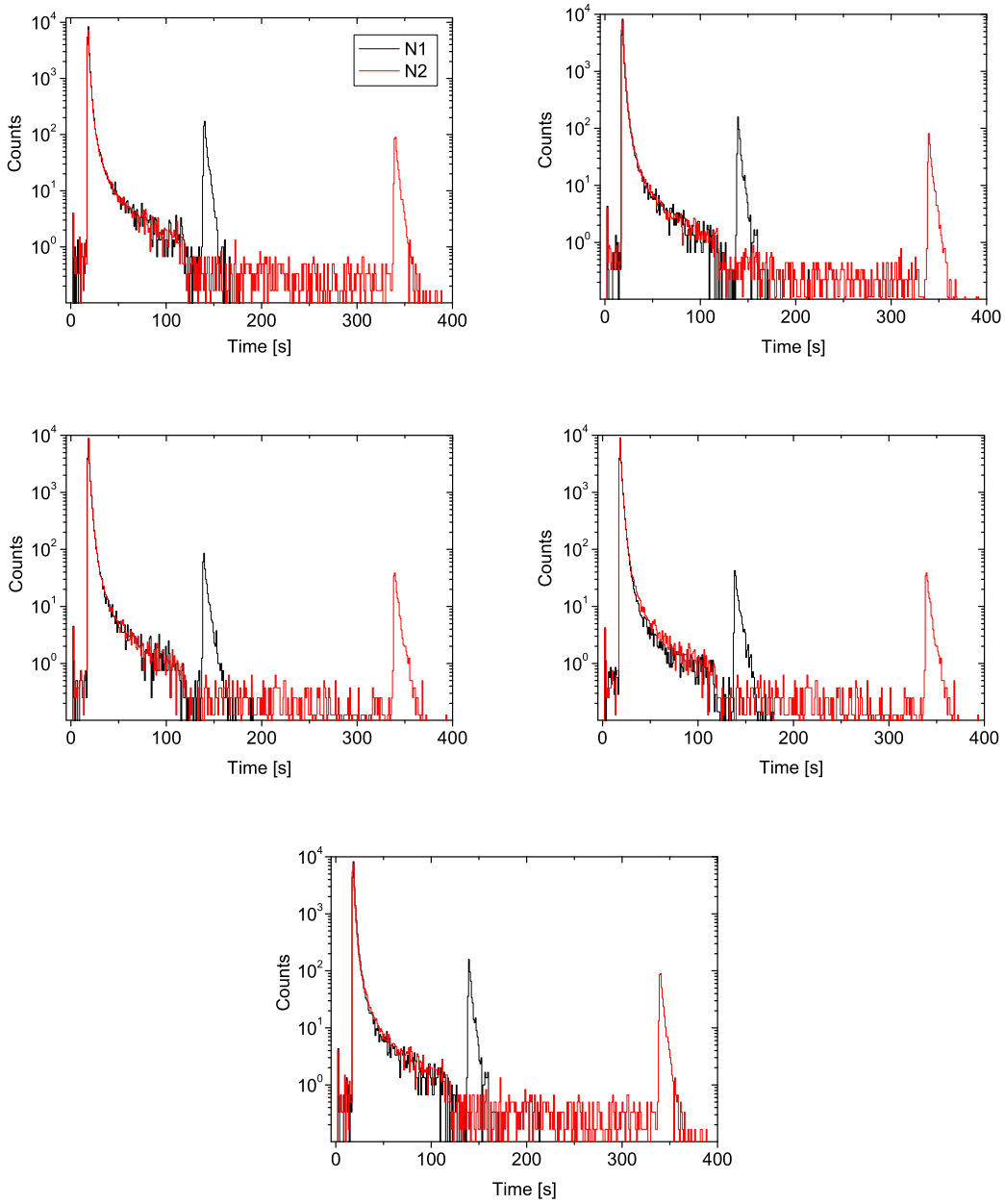

Figure 7.4:

Storage method runs for different magnetic fields. The first picture corresponds to level 0 (maximum field), the lower to level 4 (see tab. 6.1).

level 4 is shown in fig. 7.5.

The inverse spin flip corrected storage time $1/\tau^*$ can now be compared to the simulated storage time $1/\tau_{st}$, for each magnetic field level and sample geometry. Interpolation between the individual points on the curve is done linearly.

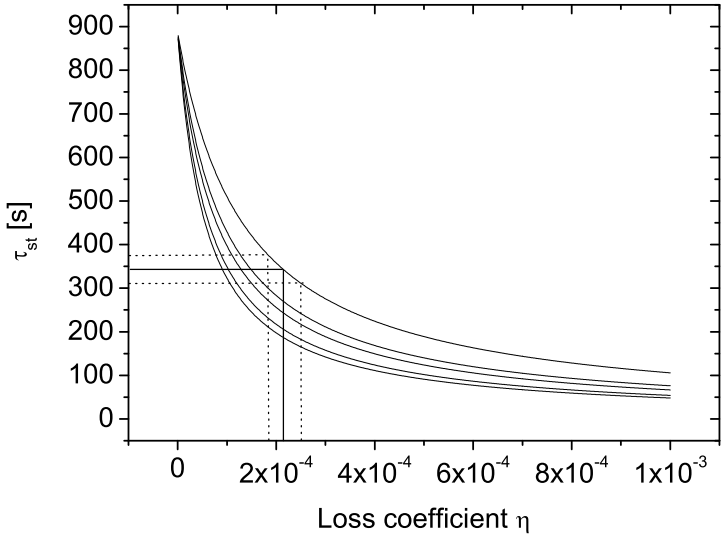

Figure 7.5:

Calibration curves for the calculated storage time τ_{st} as a function of η for the DLC PET-foil #2 sample for the magnetic field levels 0 to 4, where $1/\tau_{st} = 1/\tau_\mu + 1/\tau_n$. The uppermost curve corresponds to level 4. An example of the principle determination of η with error bars is shown. The distance between the calculated points of the curves in η is $1 \cdot 10^{-7}$ so that the error caused by evaluating from the curve is negligible.

7.1 Error Estimation

The error calculation for η is started by calculating the Gaussian error of the measured storage time:

$$\Delta\tau = \frac{t_2 - t_1}{ln(N_1/N_2)^2}\sqrt{\frac{1}{N_1} + \frac{1}{N_2}}. \tag{7.9}$$

Then by varying η, the error $\Delta\eta$ related to $\Delta\tau$ is approximated according to fig. 7.5. A cross check for possible systematic effects is that the loss coefficient η should not depend on the energy, if the correction for the background is correct.

The wall reflection frequency is fully determined using Monte Carlo simulation, which was tested in chapter 3. An uncertainty arises from the fit of the simulated to the measured spectra. By changing the shape of the simulated spectra the wall reflection frequencies also changes and this influences the value for η. Fitting different possible energy spectra through fig. 6.6 gives an estimated uncertainty of less than about $\pm 2\,\%$ in the average energy of the spectrum, which influences the wall collision frequency (and also η, consequently) with a square root behaviour. Relative to the uncertainty of the storage time this error is neglected.

Another issue is the influence of the accuracy of the Fermi potential to the measurement. The calculated value for η depends (cf. eq. 2.20) also on the Fermi potential V of the wall material. This value is not measured in this measurement. It was determined using neutron reflectometry, as it is discussed in sec. 9.5.

For the energy spectrum stored in the samples Be Al-tube TUM, BE Al-tube PNPI, Be Quartz-tube PNPI, DLC PET-foil #1 May and DLC Al-tube VT the position of the samples was mis-adjusted, as it is discussed in sec. 9.7. There the spectrum used for the analysis has a lower energy cut-off and therefore a lower average energy, which is known to about 1 %.

7.2 Results

From this analysis we get the energy dependent loss coefficients η. The samples used for the analysis are shown in tab. 7.3. For the samples DLC Al-foil at 300 K and at 70 K and for the samples DLC PET-foil at 300 K and at 70 K values averaged over the different energy level measurements are shown. The samples Be Al-tube TUM, DLC Al-tube VT, Be Al-tube and Quartz-tube PNPI and the DLC PET-foil #1 are corrected for an energy cut-off caused by a different sample position in height, which results in a different stored energy spectrum (see sec. 9.7).

For an easier comparison by eye the values are shown in fig. 7.6. All samples were taken directly from the production process as they were, without special treatment before the measurements like e.g. baking. The vacuum conditions were kept as good as possible, i.e. $\sim 1 \cdot 10^{-9}$ mbar in the sample at 70 K and $\sim 1 \cdot 10^{-7}$ mbar at 300 K in oil free vacuum to avoid additional "dirt" deposition during the measurements. With these conditions we could not measure a loss coefficient as low as it is reported for Beryllium at low temperatures of $(3 \pm 1) \cdot 10^{-5}$ [37], which was obtained after long baking treatment under Helium atmosphere. Nevertheless, in our direct comparison the DLC coated foils from the Fraunhofer Institut IWS, Dresden, i.e. DLC Al/PET-foils exceeded the value for Be, DLC on PET even by a factor of 2.6 at room temperature. At 70 K the theoretically expected value for the loss coefficient on DLC is also much lower than the value measured, similar to the losses on Be. This suggests that DLC is also affected by the so-called anomalous losses.

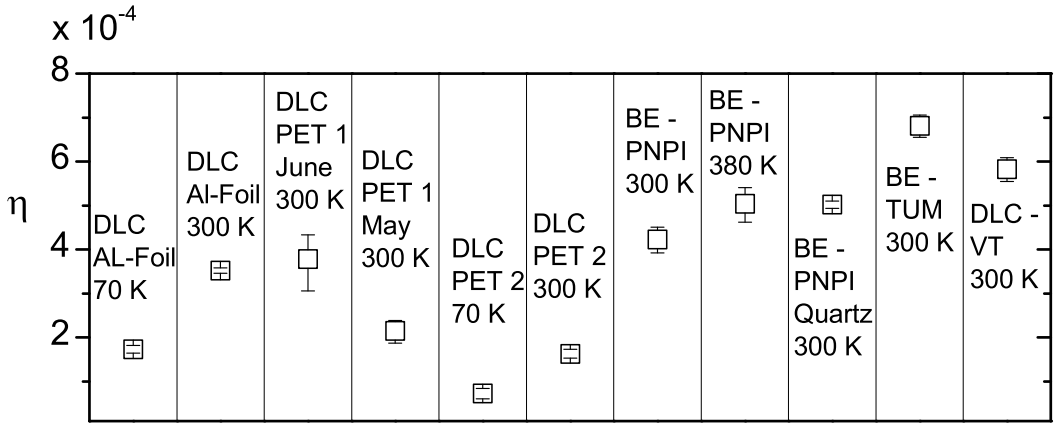

Figure 7.6:

An overview of the measured loss coefficients for the different samples. For the samples DLC on AL/PET-foil the energy averaged value is shown [78].

The DLC coated PET-foil #1 was mounted twice, once in May and once in June. The value measured in June is worse and this is not fully understood, it is probably based on a mechanical misalignment during mounting. This sample was mounted using Kapton tape, which became loose-fitting during the storage between the two measurements. DLC PET-foil #1, May and #2 were mounted and measured independently and show a similar behaviour. The values for the Be coatings are worse than expected. For the Be coating from TUM this value of $\mu = 1 \cdot 10^{-3}$ for about 180 neV was reproduced by another group [79], which is in good agreement with our value of $\eta = 6.81^{+0.26}_{-0.25} \cdot 10^{-42}$. The measurements of samples with

[2]The values can be directly compared using eq. 2.21 and a Fermi potential of 258 neV

Sample	**Loss coefficient η**
DLC AL-foil 70 K IWS level 0	$1.60^{+0.14}_{-0.12} \cdot 10^{-4}$
DLC AL-foil 70 K IWS level 1	$1.60^{+0.26}_{-0.13} \cdot 10^{-4}$
DLC AL-foil 70 K IWS level 2	$1.87^{+1.30}_{-0.14} \cdot 10^{-4}$
DLC AL-foil 70 K IWS level 3	$1.50^{+0.47}_{-0.30} \cdot 10^{-4}$
DLC AL-foil 70 K IWS level 4	$2.35^{+0.84}_{-0.57} \cdot 10^{-4}$
DLC AL-foil 70 K IWS av	$1.73^{+0.09}_{-0.09} \cdot 10^{-4}$
DLC AL-foil 300 K IWS level 0	$3.48^{+0.07}_{-0.11} \cdot 10^{-4}$
DLC AL-foil 300 K IWS level 1	$3.70^{+0.14}_{-0.14} \cdot 10^{-4}$
DLC AL-foil 300 K IWS level 2	$3.25^{+2.50}_{-0.35} \cdot 10^{-4}$
DLC AL-foil 300 K IWS level 3	$3.90^{+0.30}_{-0.20} \cdot 10^{-4}$
DLC AL-foil 300 K IWS level 4	$3.69^{+0.89}_{-0.66} \cdot 10^{-4}$
DLC AL-foil 300 K IWS av	$3.52^{+0.06}_{-0.06} \cdot 10^{-4}$
DLC PET-foil #1 IWS June 300 K	$3.78^{+0.72}_{-0.55} \cdot 10^{-4}$
DLC PET-foil #1 IWS May 300 K	$2.15^{+0.28}_{-0.24} \cdot 10^{-4}$
DLC PET-foil #2 70 K IWS level 0	$6.15^{+1.90}_{-1.50} \cdot 10^{-5}$
DLC PET-foil #2 70 K IWS level 1	$6.80^{+2.20}_{-1.80} \cdot 10^{-5}$
DLC PET-foil #2 70 K IWS level 2	$8.20^{+2.80}_{-2.50} \cdot 10^{-5}$
DLC PET-foil #2 70 K IWS level 3	$9.90^{+3.80}_{-2.90} \cdot 10^{-5}$
DLC PET-foil #2 70 K IWS level 4	$14.20^{+8.95}_{-2.53} \cdot 10^{-5}$
DLC PET-foil #2 70 K IWS av	$7.25^{+1.20}_{-1.20} \cdot 10^{-5}$
DLC PET-foil #2 300 K IWS level 0	$1.62^{+0.15}_{-0.13} \cdot 10^{-4}$
DLC PET-foil #2 300 K IWS level 1	$1.56^{+0.17}_{-0.16} \cdot 10^{-4}$
DLC PET-foil #2 300 K IWS level 2	$2.04^{+0.37}_{-0.19} \cdot 10^{-4}$
DLC PET-foil #2 300 K IWS level 3	$2.02^{+0.38}_{-0.16} \cdot 10^{-4}$
DLC PET-foil #2 300 K IWS level 4	$1.18^{+0.38}_{-0.65} \cdot 10^{-4}$
DLC PET-foil #2 300 K IWS av	$1.63^{+0.10}_{-0.10} \cdot 10^{-4}$
BE AL-tube PNPI 300 K	$4.23^{+0.31}_{-0.28} \cdot 10^{-4}$
BE Al-tube PNPI 380 K	$5.04^{+0.42}_{-0.37} \cdot 10^{-4}$
BE Quartz-tube PNPI 300 K	$5.02^{+0.08}_{-0.08} \cdot 10^{-4}$
BE Al-tube TUM 300 K	$6.81^{+0.26}_{-0.25} \cdot 10^{-4}$
DLC Al-tube VT 300 K	$5.83^{+0.28}_{-0.26} \cdot 10^{-4}$

Table 7.3:
A list of all measured loss coefficients. The samples BE AL-tube and Quartz-tube PNPI, BE Al-tube TUM and DLC Al-tube VT are corrected for the lower energy spectrum that was stored.

a strongly different surface rougness, Be on an Al-tube (mechanically polished) and on a Quartz-tube, also showed no indication that surface roughness contributes significantly to the losses.

The error bars in fig. 7.6 are due to statistics. There is no uncertainty from the Monte Carlo simulation shown. Figure 7.7 shows the values for the loss coefficient measured at different field barriers with DLC coated foils at 70 K and at 300 K. The parameter η should not be energy dependent, which is in agreement with the analysis. The values for different energies are therefore averaged, as it is shown in fig. 7.7. Averaging is done by weighting according to the error bars of the values, where asymmetric error bars are averaged for each point.

$$\overline{x} = \frac{\sum (x_i/\sigma_i^2)}{\sum (1/\sigma_i^2)} \tag{7.10}$$

with a variance of the mean value

$$\sigma^2 = \frac{1}{\sum (1/\sigma_i^2)}. \tag{7.11}$$

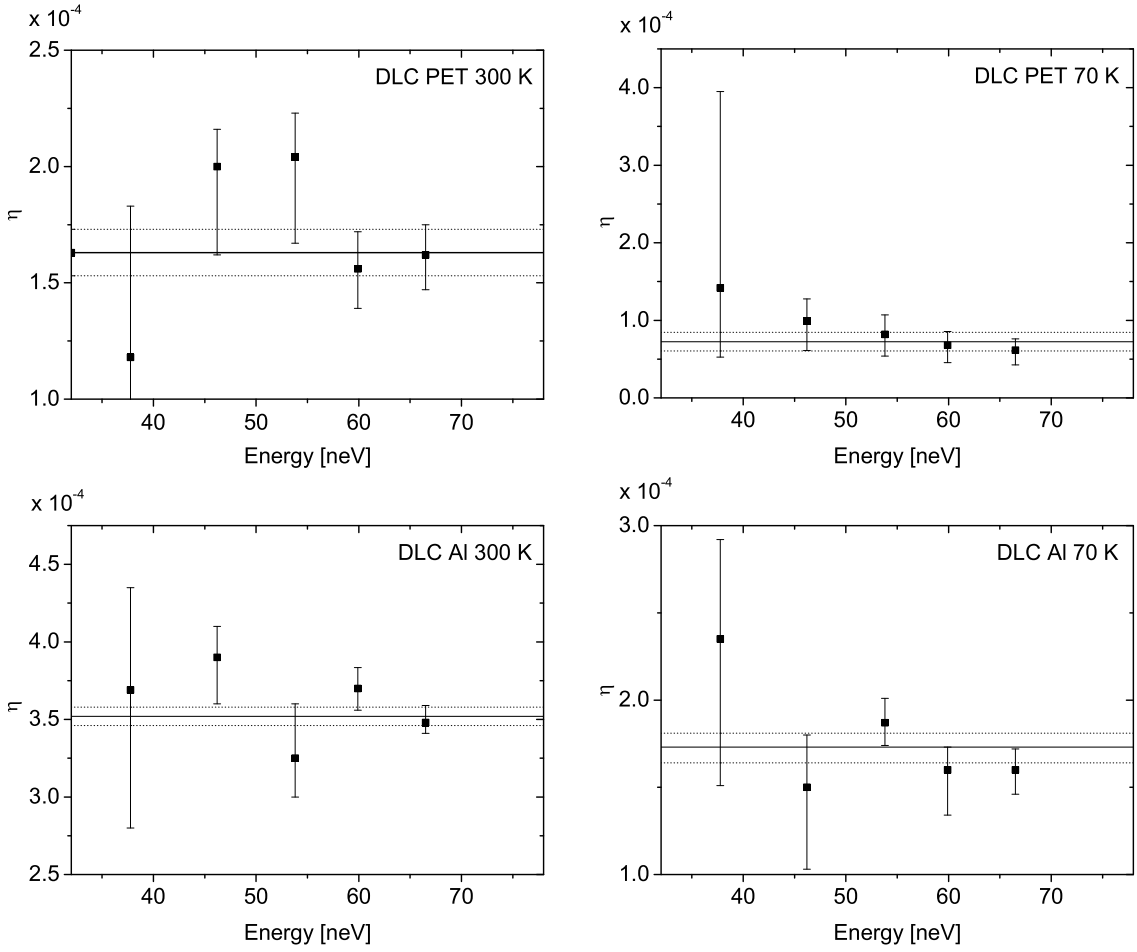

Figure 7.7:

Loss coefficients for different field levels. The values for level 0 to 4 are drawn, the energy is the average energy of the stored spectrum. The solid line is the weighted averaged value, the dotted lines are the resulting error bars.

7.3 Cross Check on the Analysis

The analysis can be also done by evaluating the loss probability from differential measurements. Here the storage time for differential energy bins is calculated and from this the loss probability $\mu(E)$ is determined. The energy range that is accessible reaches to slightly higher energies (see tab. 6.2) than the integral procedure which is shown before. For this demonstration data measured with the sample DLC PET-foil #2 at 70 K and at 300 K is used, taken from tab. 7.2. The number of neutrons per bin is obtained by subtracting the number of neutrons at level 1 from the number of neutrons at level 0 consecutively. The number at N_2 is obtained using eq. 7.4. From this a storage time per energy bin is calculated and τ_μ is extracted:

$$\frac{1}{\tau_\mu(E)} = \frac{1}{\tau(E)} - \frac{1}{\tau_n}. \tag{7.12}$$

The parameter $\tau_\mu(E)$ equals $\nu(E) \cdot \mu(E)$, with the height averaged wall reflection frequency $\nu(E)$ and the angle and height averaged loss probability $\overline{\mu}(E)$. The wall reflections and the shape of the individual bins are calculated using Monte Carlo simulations. Corrections for the different shapes of the spectra (see fig. 6.3(c)) are applied. By drawing the values for the loss probability $\mu(E)$ as a function of energy, one can compare these values to the value for η which was determined with the integral analysis from above. In fig. 7.8 the values of μ as a function of energy from the differential analysis are shown. The differential analysis is in good agreement with the integral analysis. The differential method is more sensitive to parameters that can be only addressed by Monte Carlo simulation, like the cleaning efficiency for each energy bin and the shape of the individual bins. The y-error bars in the graph are only due to statistics, the x-error bar denotes an uncertainty from Monte Carlo calculations. Due to the worse systematics this method is not discussed in more detail.

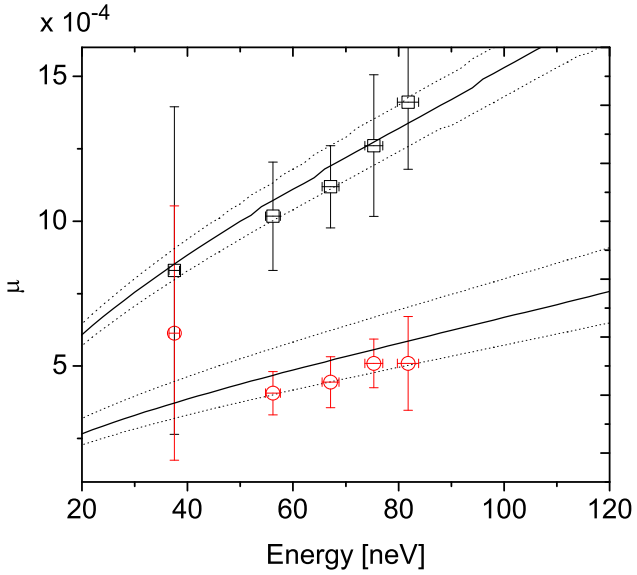

Figure 7.8:

The values for μ for different energy bins is shown for measurements at 300 K (squares) and at 70 K (circles). The lines denote the corresponding values for η, the dotted lines are the 1-σ-error bars. We used values extracted from the integral analysis of $\eta(70K) = 3.52 \cdot 10^{-4}$ and $\eta(300K) = 7.25 \cdot 10^{-5}$.

Chapter 8

Depolarization Probability

The depolarization probability can be determined using the storage method and the complementary method. At first the storage method is discussed:

8.1 Storage Method

The depolarization parameter β is calculated based to eq. 5.4. Here we consider the energy dependence of the parameters and also a correction for the background. Equation 5.5, which shows the number of spin flipped neutrons, becomes

$$\beta = \int_0^E \frac{(N_{sp}(E') - N_{bg}) \cdot g(E')}{\overline{\nu}(E') \cdot \tau_{tot}(E') \cdot (N_1(E') - N_2(E'))} dE'. \tag{8.1}$$

The parameters $N_{sp}(E')$, $N_1(E')$ and $N_2(E')$ are distributed according to the shape of the spectrum taken from sec. 6, the sum over the bins of these distributions is the measured number of N_{sp}, N_1 and N_2 as listed in tab. 7.2. The wall collision frequency $\nu(E', h)$, which is shown in fig. 7.3, is summed over all heights for each energy and is here written as $\overline{\nu}(E')$. The parameter $g(E')$ is the neutron spectrum. The parameter $\tau_{tot}(E')$ is the storage time for each energy bin, the averaged value corresponds to the measured value of τ_{tot} (eq. 5.2), without correction for spin flipped neutrons. The measurements are carried out at different magnetic field levels, to investigate on a possible energy dependency of the parameter β. The data used for the analysis is identical with those from the loss coefficient analysis from the storage method. The numerical integration over all energies is carried out by summing up over the spectrum in 2.5 neV steps.

The mean value of the background is 4.8 ± 0.3 mHz (see sec. 5.4.6). The measuring time in our experiment is only 200 s, which we can estimate an expected number of background neutrons of only 0.96 from. Therefore no Gaussian error is valid here.

8.1.1 Error Estimation

The calculation of the errors for β is done using Monte Carlo simulation, since especially for the DLC on AL-foil samples the depolarization rate is only a factor of 3 above the background level (see tab. 7.2). The background treatment is done taking into account Poisson distributed errors. The mean value of each parameter of eq. 8.1 is known, so the real measurement can be repeated in a simulation, using a Poisson distribution for the values of N_{sp}, N_{bg} and a Gaussian distribution for N_0 and $\tau(E)$ with the corresponding error as the width of the distribution. Each parameter is randomly produced and eq. 8.1 is evaluated. This procedure is repeated 10^7 times. The shape of the resulting distributions for the DLC PET-foil #2 sample at 70 K for level 3 and 4 is shown in fig. 8.1. In the case of high count rates the Poisson distribution

results in a Gaussian distribution. The convolution of Gaussian distributed numbers is again Gaussian and is not shown. For higher N_{sp} count rates the distributions therefore become Gaussian. Low coutrates cause "wiggles" due to the low number of different integer-difference combinations of N_{sp} and N_{bg} from eq. 8.1. Theses integer differences cause discrete values for β, which are smeared out by the other Gaussian distributed parameters. At high statistics this discrete values result in a continuous distribution. The error is determined from the convolution of the distributions of the measurement parameters. We define our 1-σ-range here as 68.31 % of the area of the curve around the mean value. The values outside one sigma are shaded. With this error estimation β could become also negative, which is unphysical. There are different approaches in literature on how to treat this problem [80][1]. Here we accept that the negative part is small and we simply include this region into the error bars.

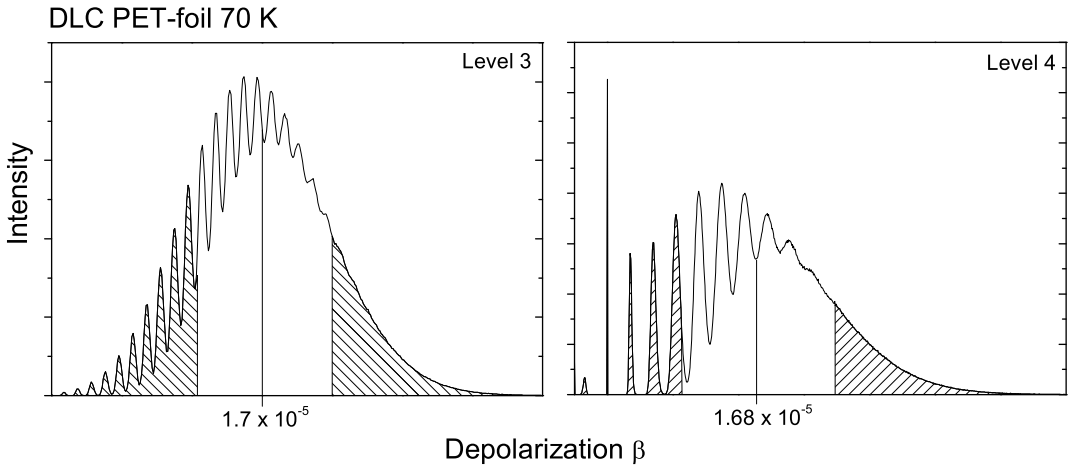

Figure 8.1:

The error bars around the expectation value of β for the DLC PET-foil #2 70 K sample is shown for the measurements at level 3 (left) and 4 (right).

8.1.2 Fit of the Spin Flip Rate with the Storage Time

The storage time has to be in agreement with the decay constant of the spin flipped neutron count rate in the detector. The fit through the spin flipped neutrons N_{sp} in the sum of DLC PET-foil #2 at level 0 measurements is shown in fig. 8.2. It gives a storage time τ of 412 $\pm$ 157 s, compared to 428 $\pm$ 59 s determined using N_1 and N_2 determined from the storage method measurement.

8.2 Complementary Method

A complementary method is to fill neutrons through the closed magnetic shutter. Only neutrons with too high kinetic energies or their polarization parallel to the field can pass the magnetic field barrier. If a neutron that can pass the field barrier makes a wall collision above

[1] A more detailed discussion of this problem is shown by the Particle Data Group, who define an upper limit of 1.64 σ for a 90 % upper limit. [81]

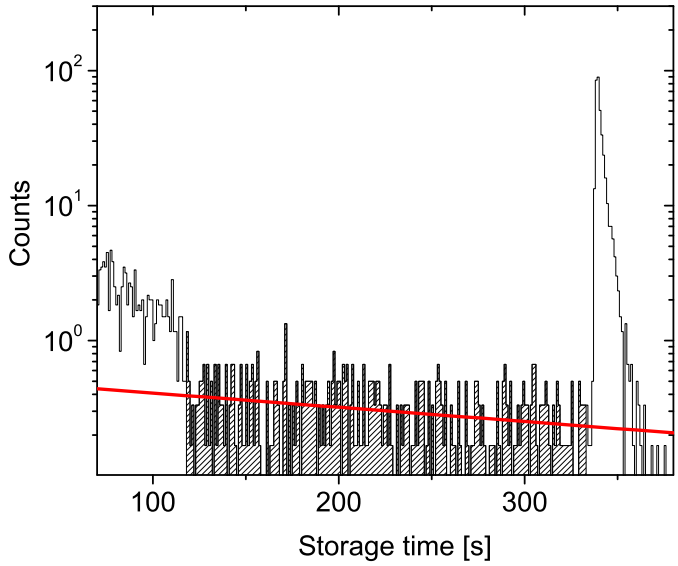

Figure 8.2:
The storage time determined using the spin flipped neutrons. The shaded region is used for fitting.

the barrier and changes its polarization direction relative to the field direction, it is trapped, if its kinetic energy is lower than the corresponding magnetic field and lower than the potential energy, that is necessary to escape on the top of the storage volume. During a filling time of typically 100 s such neutrons are accumulated. When these neutrons are emptied into the detector by switching off the detector, they are counted in one peak. The method is best suited to determine β in the case of a very low depolarization probability, where the correction for the background would cause a large systematic effect.

The equilibrium number of captured spin flipped UCN, N_{sp}, consists of a production term and a decay term

$$\dot{N}_{sp} = R^+ - R^- \tag{8.2}$$

with the decay term

$$R^- = -\lambda N_{sp} = \frac{1}{\tau} N_{sp} \tag{8.3}$$

and the production term

$$R^+ = N_0^* \cdot \nu_{par} \cdot \beta. \tag{8.4}$$

The parameter N_0^* denotes the number of neutrons inside our storage volume, which are polarized parallel to the field barrier, and do not have enough energy to escape from the volume on the top. These neutrons are stored if they undergo a spin flip. Simulations showed that the number of neutrons in equilibrium N_0^* during the accumulation time from t_0 to t_1 is equal to the number of neutrons in the same spectral range N_0 from the storage method at time t = 0 s. The number of wall collisions for the parallel polarization component ν_{par} is calculated with Monte Carlo. The number of accumulated spin flipped neutrons N_{sp} is found by integration:

$$N_{sp}(t) = R^+ \cdot \tau \cdot (1 - e^{-\frac{t}{\tau}}). \tag{8.5}$$

The parameter t denotes the time used for accumulation and τ is the storage time of the sample tube, which is measured using the storage method. Entering the magnetic field, neutrons with parallel polarization are accelerated in the magnetic field, whereas neutrons with anti-parallel oriented polarization are decelerated. The energy difference originates from the potential energy of the magnetic field, which also affects the distribution of wall collisions for the different polarization components.

After 100 s of accumulating (t_1) the magnetic field is lowered to 91 % for another 100 s (t_2). After this, the field is again raised to 100 % for 20 s in order to prepare comparable conditions to the storage method. Then the neutrons are emptied at time (t_3). The number of accumulated neutrons at time t_1 is extrapolated using the storage time τ_{tot} from the storage method measurements:

$$N_{sp}(t_1) = N_{sp}(t_3)/e^{-\frac{(t_3-t_1)}{\tau_{tot}}} \tag{8.6}$$

A typical measurement cycle for this measurement method is shown in fig. 8.3.

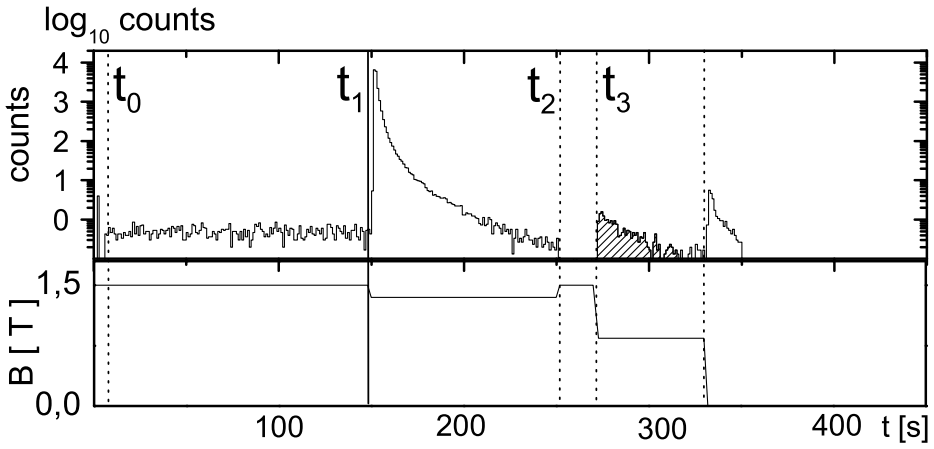

Figure 8.3:

The principle of the complementary measurement. Depolarized neutrons are accumulated from t_0 to t_1, cleaned at 91 % magnetic field level for 100 s to time t_2 and emptied at time t_3. In this picture the field is turned off in two steps, which is used as a calibration for the energy sensitive measurement, as it is shown in sec. 8.2.1. The counts between t_0 and t_1 are due to leakage through the neutron switch.

The time constants for accumulating neutrons, cleaning, storing and emptying used for a complementary measurement are shown in tab. 8.1. By emptying the bottle in steps, i.e. by consecutively lowering the magnetic field barrier, also an energy dependent measurement can be performed, as it is shown in sec. 8.2.1.

Accumulation time (t_1 - t_0)	100	s
Cleaning (t_2 - t_1)	100	s
Emptying (t_3 - t_2)	20	s
Peak length	60	s

Table 8.1:
Time constants used for the complementary method.

For the analysis of the depolarization probability β the energy dependency of the storage time, the wall collisions and the spectrum are taken into account. The eq. 8.5 becomes:

$$\beta = \int_0^E \int_0^{H(E)} \frac{N_{sp}(t_1) g(E')}{N_0(E') \nu(E', h)_{par} \tau(E') \left(1 - e^{-(t_1 - t_0)/\tau(E')}\right)} dh dE'. \tag{8.7}$$

The spectrum $g(E')$ corresponds to the full spectrum as described in sec. 6, which is equal for both polarization components. The number of spin flipped neutrons after accumulating is extrapolated from the number measured at t_3, similar to eq. 8.6, but using an energy dependent storage time $\tau(E')$:

$$N_{sp}(t_1) = N_{sp}(t_3) / e^{-\frac{t_3 - t_1}{\tau(E')}} \tag{8.8}$$

The wall collision frequency $\nu(E', h)_{par}$ for neutrons with polarization parallel to the field is larger than for neutrons with anti-parallel polarization (stored neutrons) and is simulated, see fig. 8.4. This can be qualitatively understood using eq. 3.1, which shows a linear dependence of the flux on the surface with the particle velocity. The storage times for each energy are different due to the energy dependent losses. This is calculated fitting a parameter η to the measured storage time τ_{tot} from eq. 7.1, where also losses due to spin flips are included here.

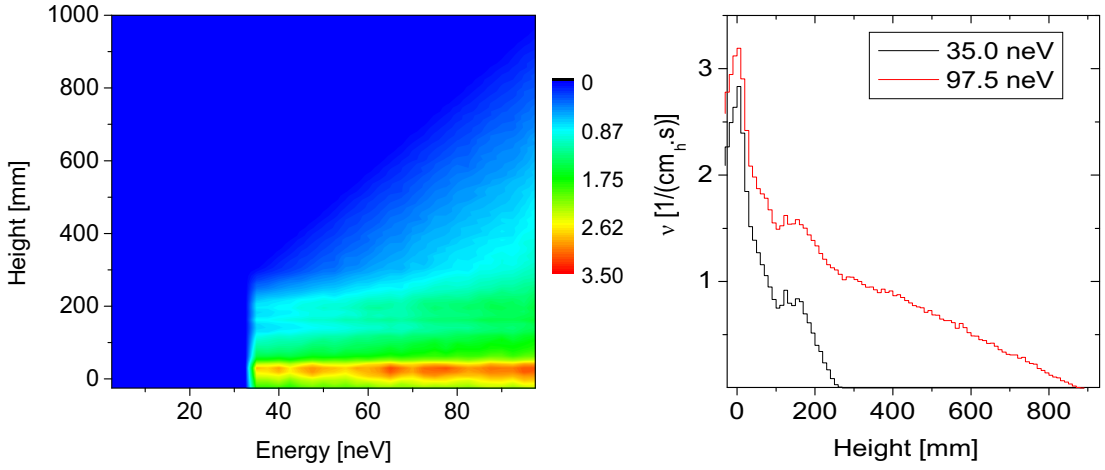

Figure 8.4:
The left plot shows the reflection frequency for different energies in dependence of the height of the bottle for the spin component that transmits the field. Blue denotes no wall collisions. The number of collisions is normalized per cm in height, second and neutron. The right plot shows two curves (35 neV and 90 neV) taken from the left plot.

8.2.1 Complementary Method using Stepwise Emptying

In fig. 8.5 the stored neutrons are emptied in steps. This means, the field is lowered to a fixed value and all neutrons with energies above this field barrier can escape through the field. After some time, typically 20-60 s, the field is lowered further and the next part of the stored spectrum can escape. In principle, one measurement with emptying in two energy steps would be enough to determine an energy dependence. However, if the field is reduced, particles with energies higher than the field barrier are counted only slowly in the detector, with a time constant of ~ 100 s. This would cause an uncertainty on the extrapolation to the number of spin flipped neutrons in equilibrium, $N_{sp}(t_1)$ and additional sensitivity to background.

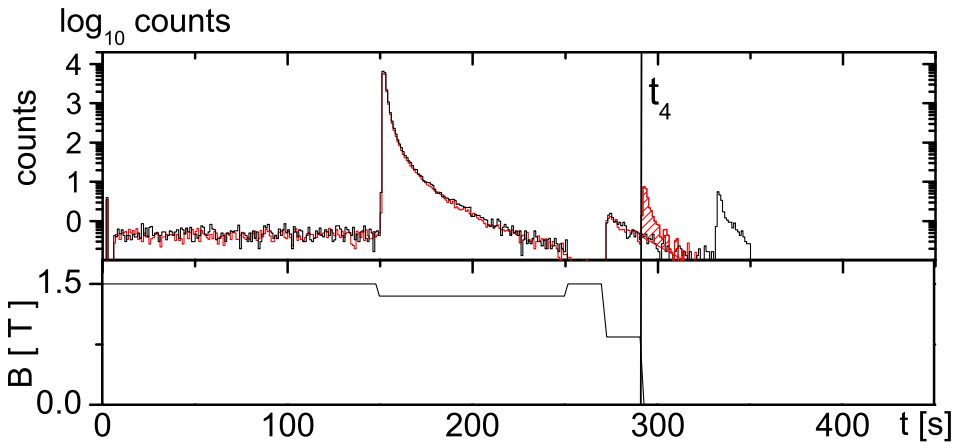

Figure 8.5:

Detector count rate as a function of time for the alternative measurement method. The two curves that are plotted on the same graph denote measurements with emptying in two energy steps. The red curve corresponds to emptying at "Step 2". The correction for counts with higher energies during emptying is shown with a fitted line (red).

In the "Step 2" measurement, neutrons with energies between 83.4 neV and 73.5 neV are emptied in a first step at 150 s after the accumulation time ended, and in a second step at 180 s (t_4) after the accumulation time. The emptying time of 30 s is not long enough to remove all neutrons with a higher energy from the bottle, and therefore the "Step 1" measurement counts are subtracted during the 50 s emptying time. This correction is denoted with a red line below the peak at t_4 in fig. 8.5.

The number of spin flipped neutrons at the end of the accumulation time, $N_{sp}(t_1)$, is extrapolated using the corresponding storage time of the sample, similar to sec. 8.2, with the time constants $t_4 - t_1 = 180$ s. The energy range of the two steps is shown in tab. 8.2.

To extract a value for β, the reflection frequency and the shape of the spectrum has to be calculated. The analysis is done analogous to ec. 8.2, using the two simulated spectra for the energy steps (see fig. 8.6), the reflection frequencies from fig. 8.4 and the corrected number of neutrons at "Step 2".

Step	Low [neV]	High [neV]	Average [neV]
Step 1	73.5	83.4	78.64
Step 2	28.8	73.5	57.24

Table 8.2:
The two energy bins in the analysis of the two-step emptying measurements.

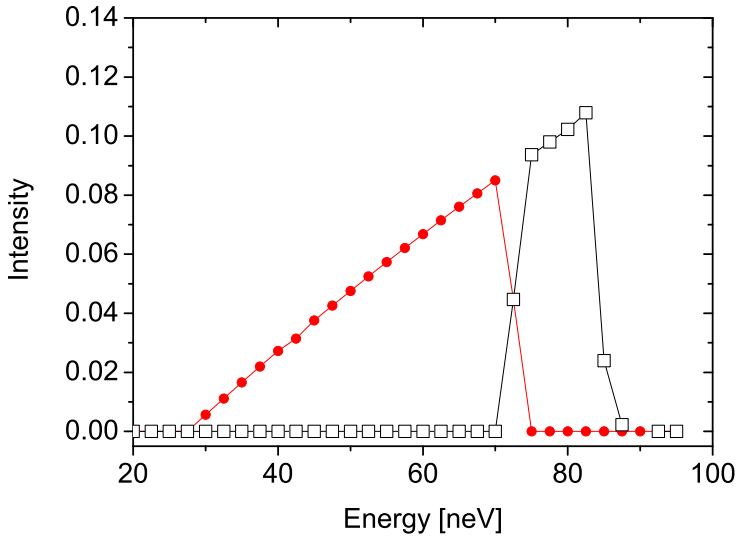

Figure 8.6:
The parts of the energy spectrum covered by "Step 1" (red) and "Step 2" (black).

8.2.2 Error estimation

The advantage of the complementary method compared to the storage method is that it is not really sensitive to the background, since the spin flipped neutrons are counted in a short time ($\sim 20\,\mathrm{s}$) and the expected background is therefore 10 times smaller compared to the storage method. Therefore the background correction is negligible. The error is calculated using Gaussian error propagation for each energy.

$$\delta\beta = \sqrt{dN_0 + dN_{sp} + D\tau} \tag{8.9}$$

with

$$\begin{aligned} \sqrt{dN_0} &= \frac{N_{sp}}{N_0^2 \tau\nu \left(1 - e^{-}t_o/\tau\right)} \\ \sqrt{dN_{sp}} &= \left(N_0\nu\tau \left(1 - e^{-}t_o/\tau\right)\right)^{-1} \\ \sqrt{d\tau} &= \frac{N_{sp}\left(1 - e^{-}t_o/\tau\right) + \tau^{-1}e^{-}t_o/\tau}{N_0\nu\tau^2\left(1 - e^{-}t_o/\tau\right)} \end{aligned} \tag{8.10}$$

8.3 Results

The results of the depolarization probability analysis are listed in tab. 8.3 for the storage method and the complementary method.

The sample BE Al-tube PNPI at 300 K was measured two times, the second time in two step emptying. For easier comparison the results are shown in fig. 8.7. The storage method values for the DLC PET-foil #2 at 300 K, at 70 K, DLC Al-foil at 300 K and at 70 K are weighted averages from 5 measurements with different fields (see fig. 8.8). Averaging is done by weighting with the error bars as shown before. Regions where the error allowed for the uphysical case of a negative value of β were included in the average. The weight of such points is small due to the large size of their errors. An important conclusion from the energy sensitive measurements of the depolarization parameter is that no energy dependence could be observed, as it is shown in fig. 8.8. The inconsistent behaviour of the DLC PET-foil #1 in May and June is most probably caused by the way the sample was mounted in June.

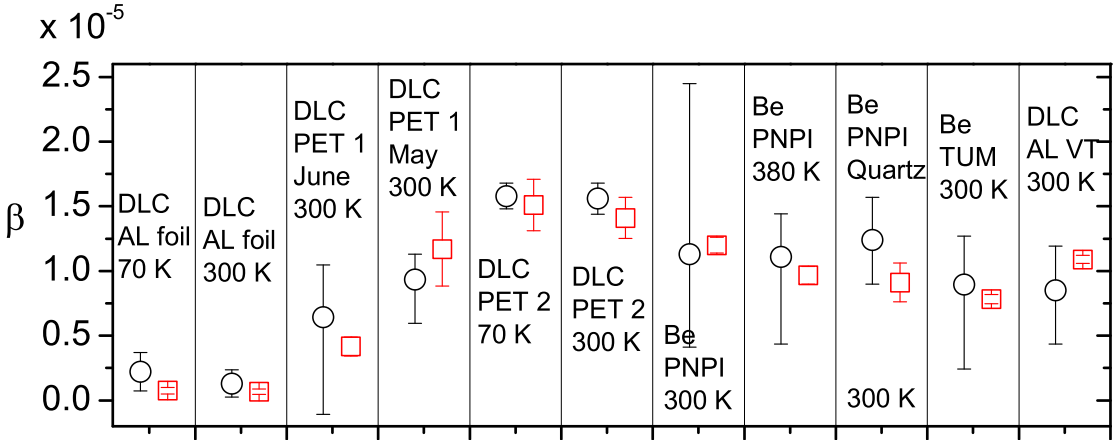

Figure 8.7:

Compilation of all depolarization measurements. The red squares represent the number obtained from the complementary method measurements, the black circles represent the values obtained from the standard method.

The measured values for the depolarization for all Be samples, the DLC Al-tube from VT and the DLC coated PET-foils are on a similar level of $1 - 1.5 \cdot 10^{-5}$ per wall collision, which is in good agreement with literature. The depolarization is not temperature dependent, also no energy dependency in our energy range could be observed. The values for DLC on Al-foil are one order of magnitude lower than all other samples. Systematic effects that could influence these measurements are discussed in chapter 9. A more detailed discussion is given in chapter 10.

Sample	**Storage method β**	**Complementary method β**
DLC AL-foil IWS 70 K level 0	$1.80^{+1.33}_{-2.20} \cdot 10^{-6}$	
DLC AL-foil IWS 70 K level 1	$3.17^{+2.54}_{-3.16} \cdot 10^{-6}$	
DLC AL-foil IWS 70 K level 2	$4.80^{+3.19}_{-8.48} \cdot 10^{-6}$	
DLC AL-foil IWS 70 K level 3	$5.00^{+7.34}_{-2.75} \cdot 10^{-6}$	
DLC AL-foil IWS 70 K level 4	$8.50^{+7.71}_{-2.61} \cdot 10^{-6}$	
DLC AL-foil IWS 70 K av	$2.22^{+1.48}_{-1.48} \cdot 10^{-6}$	$0.76 \pm 0.25 \cdot 10^{-6}$
DLC AL-foil IWS 300 K level 0	$1.28^{+1.24}_{-3.66} \cdot 10^{-6}$	
DLC AL-foil IWS 300 K level 1	$2.61^{+1.15}_{-4.17} \cdot 10^{-6}$	
DLC AL-foil IWS 300 K level 2	$7.70^{+3.61}_{-7.80} \cdot 10^{-6}$	
DLC AL-foil IWS 300 K level 3	$5.10^{+4.88}_{-10.05} \cdot 10^{-6}$	
DLC AL-foil IWS 300 K level 4	$-3.80^{+2.40}_{-2.30} \cdot 10^{-6}$	
DLC AL-foil IWS 300 K av	$1.31^{+1.05}_{-1.05} \cdot 10^{-6}$	$0.67 \pm 0.21 \cdot 10^{-6}$
DLC PET-foil #1 IWS June 300 K	$6.43^{+4.05}_{-7.52} \cdot 10^{-6}$	$4.17 \pm 0.72 \cdot 10^{-6}$
DLC PET-foil #1 IWS May 300 K	$9.33^{+0.37}_{-1.98} \cdot 10^{-6}$	$11.17 \pm 2.87 \cdot 10^{-6}$
DLC PET-foil #2 IWS 70 K level 0	$1.67^{+0.18}_{-0.35} \cdot 10^{-5}$	
DLC PET-foil #2 IWS 70 K level 1	$1.52^{+0.21}_{-0.26} \cdot 10^{-5}$	
DLC PET-foil #2 IWS 70 K level 2	$1.53^{+0.16}_{-0.29} \cdot 10^{-5}$	
DLC PET-foil #2 IWS 70 K level 3	$1.68^{+0.36}_{-0.46} \cdot 10^{-5}$	
DLC PET-foil #2 IWS 70 K level 4	$1.70^{+1.15}_{-1.20} \cdot 10^{-5}$	
DLC PET-foil #2 IWS 70 K av	$1.58^{+0.10}_{-0.10} \cdot 10^{-5}$	
DLC PET-foil #2 IWS 70 K - 2 step 1		$15.10 \pm 2.00 \cdot 10^{-6}$
DLC PET-foil #2 IWS 70 K - 2 step 2		$15.50 \pm 1.46 \cdot 10^{-6}$
DLC PET-foil #2 IWS 300 K level 0	$1.43^{+0.18}_{-0.33} \cdot 10^{-5}$	
DLC PET-foil #2 IWS 300 K level 1	$1.50^{+0.24}_{-0.39} \cdot 10^{-5}$	
DLC PET-foil #2 IWS 300 K level 2	$1.51^{+0.25}_{-0.44} \cdot 10^{-5}$	
DLC PET-foil #2 IWS 300 K level 3	$3.30^{+0.56}_{-3.70} \cdot 10^{-5}$	
DLC PET-foil #2 IWS 300 K level 4	$3.11^{+1.65}_{-1.95} \cdot 10^{-5}$	
DLC PET-foil #2 IWS 300 K av	$1.56^{+0.12}_{-0.12} \cdot 10^{-5}$	$14.10 \pm 1.59 \cdot 10^{-6}$
BE AL-tube PNPI 300 K	$1.13^{+1.32}_{-0.78} \cdot 10^{-5}$	$12.00 \pm 0.50 \cdot 10^{-6}$
BE AL-tube PNPI 300 K- 2 step 1		$12.60 \pm 0.62 \cdot 10^{-6}$
BE AL-tube PNPI 300 K- 2 step 2		$12.00 \pm 0.50 \cdot 10^{-6}$
BE Al-tube PNPI 380 K	$1.11^{+0.33}_{-0.67} \cdot 10^{-5}$	$9.66 \pm 0.68 \cdot 10^{-6}$
BE Quartz-tube PNPI 300 K -1	$1.24^{+0.38}_{-0.34} \cdot 10^{-5}$	$9.11 \pm 1.50 \cdot 10^{-6}$
BE Quartz-tube PNPI 300 K -2	$1.24^{+0.38}_{-0.34} \cdot 10^{-5}$	$9.66 \pm 0.68 \cdot 10^{-6}$
BE Al-tube TUM 300 K	$8.95^{+0.38}_{-0.65} \cdot 10^{-5}$	$7.83 \pm 0.35 \cdot 10^{-6}$
DLC Al-tube VT 300 K	$8.52^{+0.34}_{-0.42} \cdot 10^{-5}$	$10.90 \pm 0.3 \cdot 10^{-6}$

Table 8.3:
The depolarization values for the DLC foils and the BE and DLC tube samples using the storage method and the complementary method.

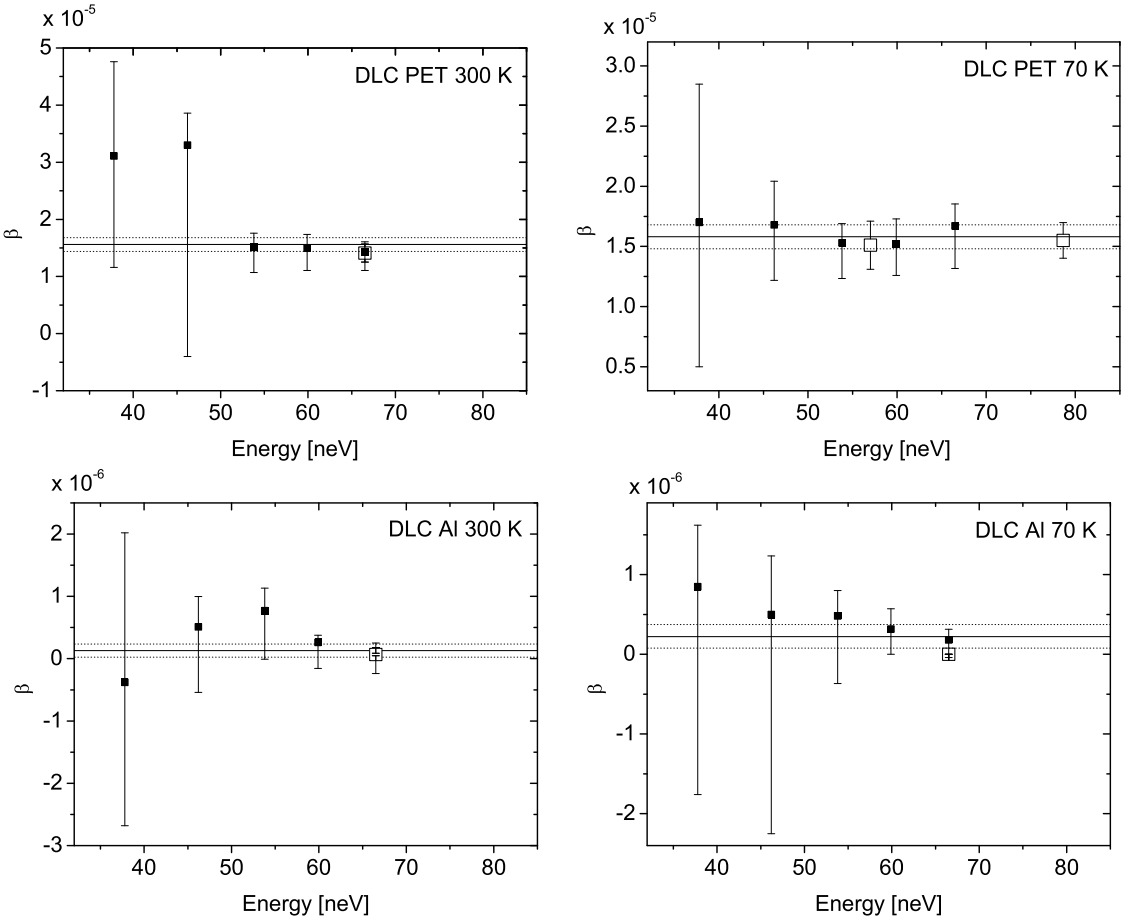

Figure 8.8:

The weighted averages of the measurements. The curves are for the DLC Al foil at 300 K, DLC Al foil at 70 K, DLC PET foil #2 at 300 K, DLC PET foil #2 at 70 K. The y-axis denotes the depolarization probability. The full squares in each graph correspond to the measurements at different magnetic field levels (0 to 4). The solid line denotes the average of these measurements with the dotted lines the corresponding error bars. The open squares are the values obtained from the alternative method, two points for DLC PET #2 at70 K are the values deduced from stepwise emptying (see sec. 8.2.1) at 78.6 neV and 57.2 neV).

Chapter 9

Systematic Effects

9.1 Cleaning Times

A comparison of a measured and a simulated cleaning curve is shown in fig. 9.1. The Monte Carlo simulation can reproduce the cleaning behaviour of the magnetic storage volume, which is a stringent test on our understanding of the experiment. During the first seconds the detector count rate depends on the initial incident spectrum that enters the tube. The difference is caused by an upper energy cut-off in the simulated spectrum that is lower compared to the experimental spectrum. Additionally, only the anti-parallel polarization component (which can be stored in principle) is produced in the simulation, whereas in the real situation the parallel polarization component is also measured in the detector. After a few seconds these different initial conditions disappear. During the next $\sim 60\,\mathrm{s}$ the simulation is not sensitive to our free parameters β and η.

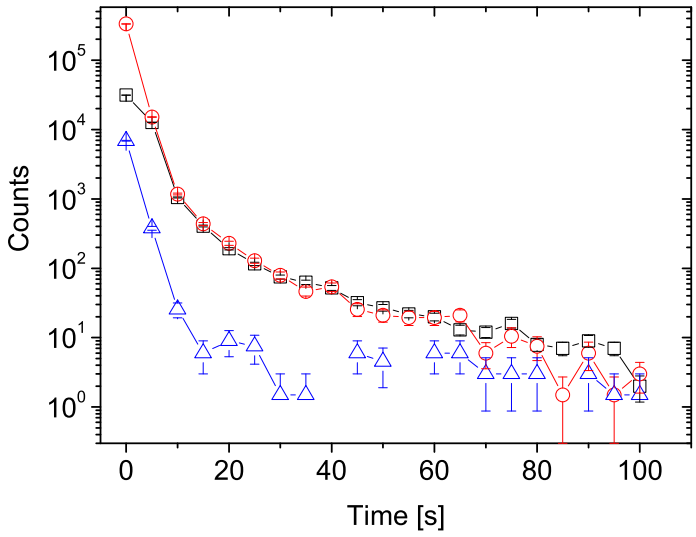

Figure 9.1:

The counts in the detector in dependence of storage time are shown. The squares are the measured cleaning curve for the Al-foil sample at 70 K, the circles are the simulated points. Spin flipped neutrons are included in the circles, they are additionally shown as triangles.

After about 60 s the countrates become small and the simulated curve shows some dependence on the chosen spin flip probability. During the last 5 s bin the field is ramped up to 100 %.

9.1.1 Variation of the Cleaning Times

The length of the magnetic cleaning time is a critical issue. If it is too short, neutrons other than the spin flipped neutrons will pass the magnetic field during the measurement and will be counted as spin flipped neutrons. This would also change the exponent of the storage behaviour. In a simulation before the experiment was performed (see fig. 5.7), the cleaning time was calculated using a simplified field configuration, i.e. a linear field gradient of 0.15 T/cm with 1.5 T at z = 0 and a value close to 0 at z = 100 mm. The estimated time constant was 60 s for this configuration. The field in the realistic situation is more complicated, making the cleaning process slower. Therefore we chose 100 s as a standard cleaning time. Tests with longer storage times are shown in fig. 9.2, where a DLC-Al foil sample measured at level 0 was used.

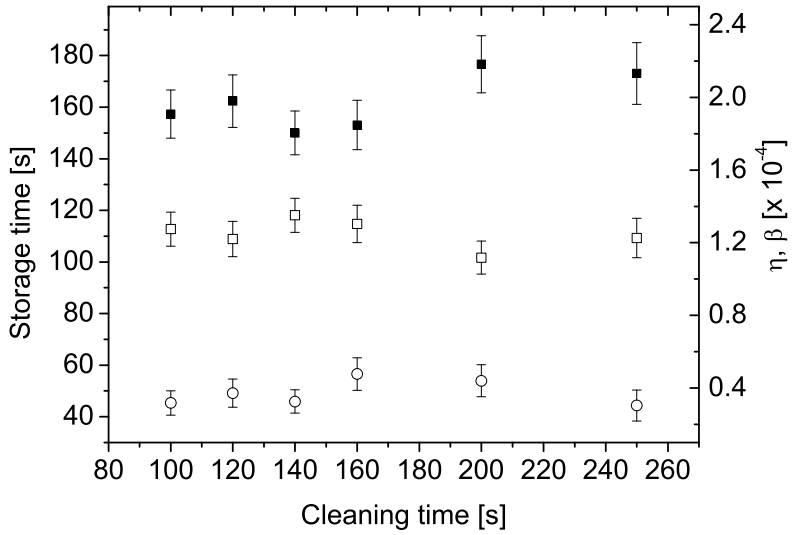

Figure 9.2:

The dependence of the storage time on the cleaning time. The upper curve (filled squares) is related to the left axis and denotes the storage time for different lengths of cleaning times. The circles show the (spectrum averaged) depolarization, related to the right scale. For illustration, also spectrum averaged values for η (open squares) are given, they are related to the right scale.

A second test is to analyze β for a high statistics sample by using only the first half of the spin flip counting time (0 s to 100 s), and similar for the period between (100 s and 200 s), where 0 corresponds to t_1 and 200 to t_2. By comparing these values one can see, if the β value determined from the first half of the counting time would be significantly higher than the second one. This would be an indication of a non sufficient cleaning time. Figure 9.3 shows that no systematic effect could be observed. The value for β given here is averaged over the energy spectrum without background correction.

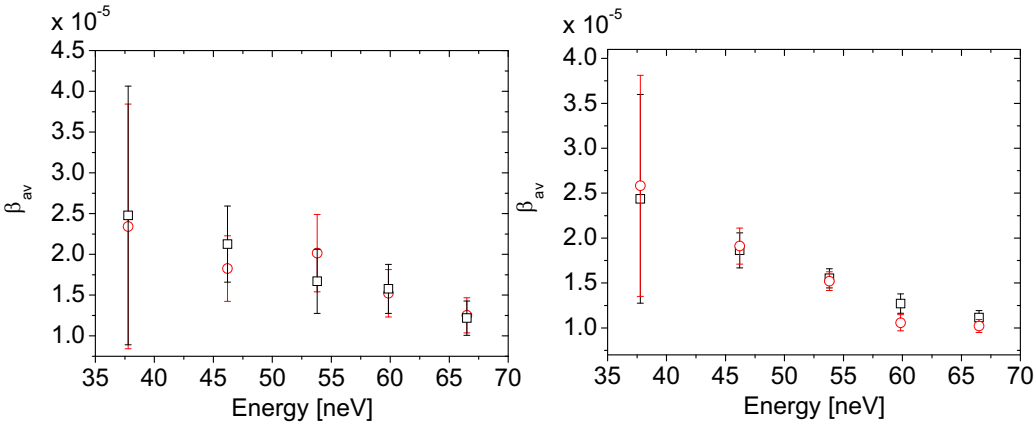

Figure 9.3:

Values for β calculated for an averaged spectrum without background correction for the first and the second half of the counting time, each 100 s, left for DLC PET-foil #2 300 K, right 70 K. The obvious energy dependence results from the simplified analysis, which should only point out any difference between the first and second half of the measuring time.

9.1.2 Long Storage Times

When we measure the storage time we deduce this value from only two measured points at two times and assume that there is only one exponent. To test on this, measurements with the same cleaning procedure as the one for the storage method were performed. A storage time curve with more points over a longer timescale was measured. The storage time constant becomes larger with longer storage times due to the higher losses of neutrons with higher energies. A set of measured exponents for various samples is shown in fig. 9.4 (left). The change of the storage time exponent of the cleaned spectrum is small since the spectrum range is very narrow in energy. The storage times are in good agreement with the measurements from the storage method. Table 9.1 shows the fitted exponents.

If there is no cleaning procedure applied, the spectrum cleans itself with a longer time constant. The exponent of this cleaning procedure is shown in fig. 9.4 (right), the measured exponent is in good agreement with the simulation. The measured storage time after natural cleaning of the spectrum is 171 ± 9 s for the DLC Al-tube VT sample, compared to 160.7 ± 6.0 s for the storagetime with cleaning before.

9.2 Magnetic Heating

The upper limit for a possible energy gain of UCN during storage in the magnetic bottle originating from field fluctuations is calculated. The measured coil current stability is on the relative level $1{\cdot}10^{-4}$, which is a worst case limit for field fluctuations, and shown only for the demonstration of a possible effect.

A simulation using a ripple with 50 Hz field fluctuation with a maximum amplitude of $1 \cdot 10^{-4}$ shows no significant heating. The temporal dependence of this effect is shown in fig. 9.5. The assumption of a magnetic field instability on this level is quite conservative, since the field does not follow the fluctuations automatically. Additional heating tests were carried

Sample	$\tau_1[s]$	$\tau_2[s]$
DLC Al-tube VT 300 K	160.7 ± 6	157 ± 6.0
BE Al-tube TUM 300 K	141.3 ± 4.5	138 ± 4.5
BE Al-tube PNPI 380 K	180 ± 11	176 ± 11.2
BE Quartz-tube PNPI 300 K	140 ± 12	133 ± 3.7
DLC PET-foil #1 June 300 K	210.4 ± 28.1	210 ± 28.2
DLC PET-foil #1 May 300 K	332 ± 24	316 ± 24.5

Table 9.1:
The parameter τ_1 corresponds to the storage time fitted through the curve with more measurements, τ_2 corresponds to the storage times from tab. 7.2.

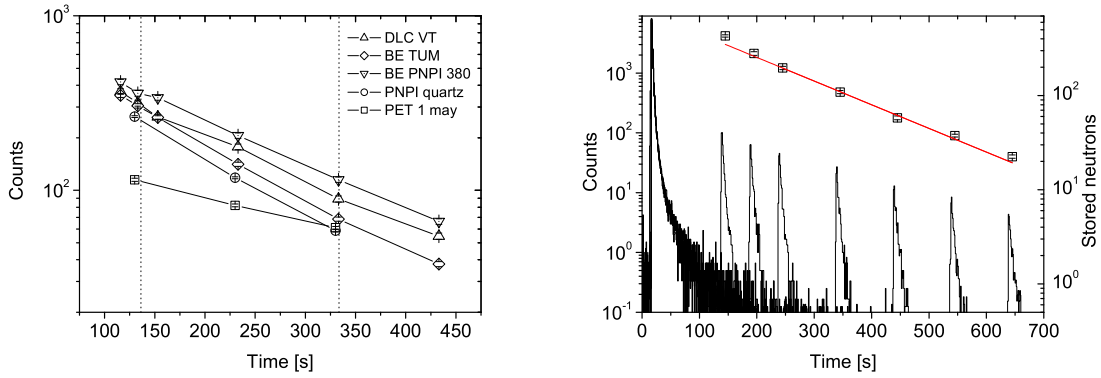

Figure 9.4:
Left: storage times for the cleaned spectrum with more points over a longer time. The lines correspond to the times used for emptying, t_1 and t_2, from the storage method. Right: the average counts in the detector are shown (left axis). The sum of the peaks is denoted by the open squares (right axis).

out by storing neutrons with additional wiggles on the magnetic field. The maximum frequency modulation of the field strength is given by the internal properties of the power supply of the magnet. This is fixed by the minimum internal ramp and based on the inductivity of the magnet which causes an induced voltage into the power supply. This allows for a maximum ripple frequency of about 1 Hz and therefore no visible magnetic heating could be observed.

9.3 Low Energy Heating

For tests on the so-called low energy heating, we can give a limit from two different tests:

The first test is shown in fig. 9.6. Here we store neutrons with a limiting potential of 73.5 neV for 100 s. Then the field was set to 73.5 neV, 83.4 neV, 87.5 neV or 91.3 neV for additional 200 s. At the end, the number of stored neutrons was counted. If the field is kept at a level of 73.5 neV, natural cleaning continues and therefore the number of neutrons is smaller after the storage time as compared to the case when the field is raised. If the field is increased, the number of neutrons is not changed by cleaning any more. The number of stored

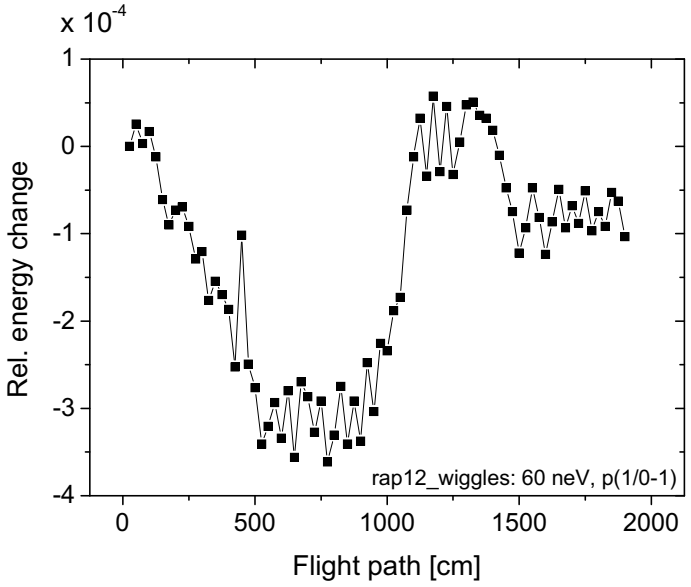

Figure 9.5:

Simulated relative energy change with a 50 Hz ripple on the field added. The height of the ripple is in every position of the field 10^{-4} of the absolute value of the field.

neutrons does not depend on the level to which the field is raised after cleaning, between 73.5 neV and 91.3 neV. By comparing the number of stored neutrons for these measurements we can estimate an upper limit for low energy heating:

$$\Delta_1 \sim \frac{\Delta N}{N \cdot \nu \cdot \Delta t} \tag{9.1}$$

with N the number of counted neutrons, ΔN the difference of the number of stored neutrons after cleaning at 83.4 neV and 87.4 neV field barrier, ν the reflection frequency and Δt the storage time after cleaning. The three measurements for the increased field do not show an increasing number of neutrons within statistics. This is the case for both temperatures. A limit for potential low energy increase can be estimated within the statistics by comparing the value at 83.4 neV to the averaged values at 87.4 neV and 91.3 neV. Using the numbers of neutrons from fig. 9.6 into eq. 9.1 for 300 K and 70 K, and combining the resulting numbers with errors, we can estimate an upper limit of $\Delta_1 < 2 \cdot 10^{-6}$ per wall collision.

A second test can be done by comparing the values of β from the storage method and from the complementary method. For illustration we compare the depolarization values for each sample by dividing and calculate an error for each. The value for β is 2.9 ± 0.8 % smaller for the alternative method. The difference can be interpreted as neutrons, that will be counted as spin flipped neutrons in the storage method, but being lost in the complementary method. If a neutron gains energy during a wall collision, it can pass the magnetic barrier and it will be counted in the detector in the storage method and will be therefore considered as spin flipped. In the complementary method, only stored UCN are considered, heated UCN have left the volume already before they are counted. In case of low energy heating in the storage method the number of neutrons that can pass the field barrier is described by the depolarization probability β, which consists of the real depolarization effect and a small portion of heated

neutrons, $\beta = \beta + \Delta_2$. Therefore the upper limit for low energy heating can be estimated by subtracting the values for β from both methods.

$$\Delta_2 \sim \beta_{st} - \beta_{compl} \tag{9.2}$$

The difference is calculated by subtracting the values for β (see tab. 8.3) for each measurement. The differences for each sample are weighted with the Gaussian error based on the values for η. The upper limit for the probability for heating per wall collision Δ_2 is then $1.4 \cdot 10^{-6}$. In ref. [82] a dedicated experiment for the investigation of such an effect was carried out. They find a probability of $< 2 \cdot 10^{-8}$ per collision for an even higher increase of energy, which is in contradiction to [83], who find a probability of $1 \cdot 10^{-7}$ per collision.

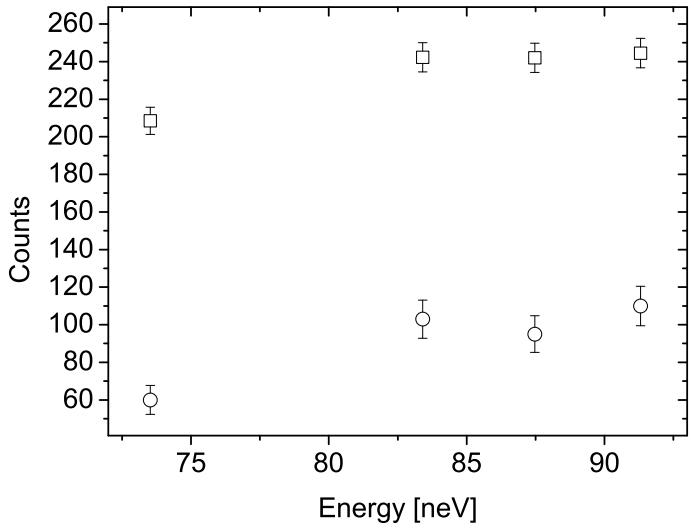

Figure 9.6:

Measurements of a possible magnetic heating effect. The number of stored neutrons after 100 s of cleaning and 200 s of storage in dependence of the field barrier strength. The squares show the number of stored neutrons for the DLC PET-foil #2 sample at 70 K, the circles at 300 K. The measurement turned out to be a good test on our cleaning efficiency. The energy scale denotes the upper limit of the stored energy.

9.3.1 Field Depolarization

In an experimental test, depolarization in low field regions was tested by varying the magnitude of the holding field. The nominal value for the holding field was $5.6 \cdot 10^{-3}$ T inside the holding field coils. The aim of the variation was to look for a difference in the depolarization value for different field configurations. If the direction of the storage field and the holding field is the same, no influence of the depolarization effect on the field strength could be observed. For a reversed holding field an increased depolarization effect could be observed as shown in fig. 9.7.

In the followning a theoretical limit on the influence of this effect on our measurements is estimated. The calculated field map of the magnet and the holding field coil is shown in fig. 9.8. The current in the magnet is 300 A, the holding field in the picture is 5 mT. In the right picture the holding field polarity is reversed. At z = 360 mm above the middle of the magnet gap, the field becomes zero.

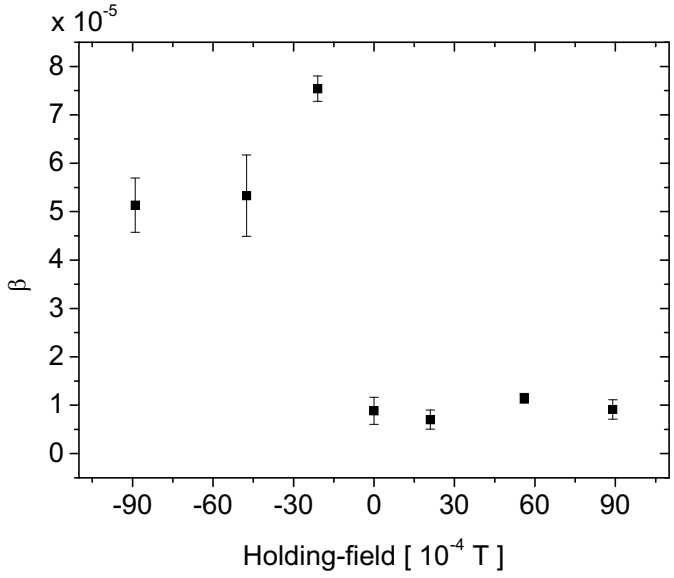

Figure 9.7:

Dependence of the field depolarization on the holding field. The energy averaged depolarization parameter β as a function of the strength of the holding field. The error bars do not account for the influence of energy dependent parameters and background. The curve was measured with the Be Al-tube, PNPI, sample at 380 K.

The situation for such a zero field transition can be simulated. The zero field region is implemented in the GEANT4 simulation as a magnetic field with a field strength of $5 \cdot 10^{-3}$ T, 50 mm above and below the zero field plane at z = 360 mm, decreasing linearly to this plane. An external homogeneous field at 45° to the holding field direction is superimposed. The strength of this field is varied from $1 \cdot 10^{-6}$ to $1 \cdot 10^{-2}$ T. The orientation of the polarization vector during the transition of the low field region is shown in fig. 9.9. The polarization is calculated by numerically solving the Bloch equation (eq. 3.2), as it is described in sec. 3.2.2. At higher field strengths the neutron follows the field change adiabatically. Due to the small field strength the trajectory of the UCN is not influenced, and the approach described in sec. 3.2.2 can be applied.

From this simplified picture we can estimate a spin flip probability. The probability amplitude (eq. 2.37) is $a = cos(\theta/2)$, where θ is the angle between the polarization vector and the field direction. The probability P of spin flip is then

$$P = 1 - a^2 \tag{9.3}$$

For this situation, it is possible to simulate a probability of spin flip during a low field transition. This is estimated in such a way that we assume that the neutron bounces upwards through the low field region and falls down into the field barrier again, where the spin state is analyzed. In the case of a holding field parallel to the field of the magnetic shutter, we can obtain a value for field depolarization during normal storage conditions. We assume a gradient of $3 \cdot 10^{-2}$ T/m of the magnetic field around the low field position. The value of the earth magnetic field is $\sim 5 \cdot 10^{-5}$ T. The storage time is again 200 s, the number of transitions through the low field region is about 2 Hz. Then the spin flip probability per neutron in 200 s

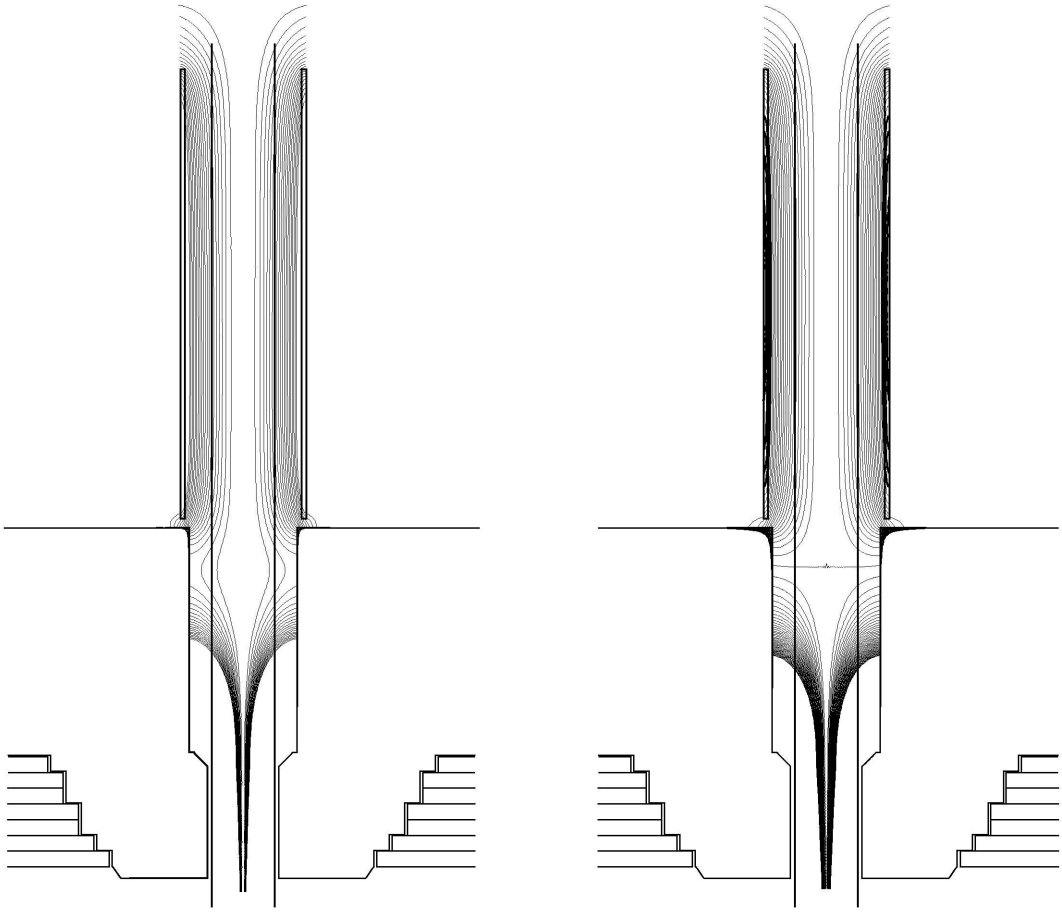

Figure 9.8:

In the left picture the holding field and the magnet have a parallel orientation, in the right picture the current in the holding field coil is reversed. The field lines are projected from the rotationally symmetric situation on a plane, that is why the field lines in the coil are not equidistant.

is $P < 1 \cdot 10^{-4}$, this means 1 of 10^4 neutrons will flip the spin during the measuring time. This can be expressed in terms of a false value for β. If we assume a wall collision frequency of $\nu = 30\,\mathrm{Hz}$ and a storage time of $\Delta t = 200\,\mathrm{s}$, we obtain

$$\beta = P/\nu/\Delta t \sim 1 \cdot 10^{-8} \tag{9.4}$$

per collision. This is a rough assumption, since it is not easy to find out the configuration of the very low fields in detail. The value thus corresponds to an upper limit. Further investigations on this problems are shown by [84, 85].

A practical upper limit for field depolarization is the low value for the DLC coated Al-foil, which shows a depolarization probability of $\beta < 1 \cdot 10^{-6}$ per wall collision All other samples show a factor of 10 more. This cannot be caused by the field configuration, which was identical for all samples. The different geometries used in the measurements cannot contribute to the depolarization: the different geometries were mounted asymmetrically inside the tube, where field inhomogeneities are expected to be symmetrical. This makes the DLC Al-foil, with a smaller geometrical cross section also sensitive to every field depolarization that might occur in any other sample geometry. Mounting of these foils was done with Aluminum parts and

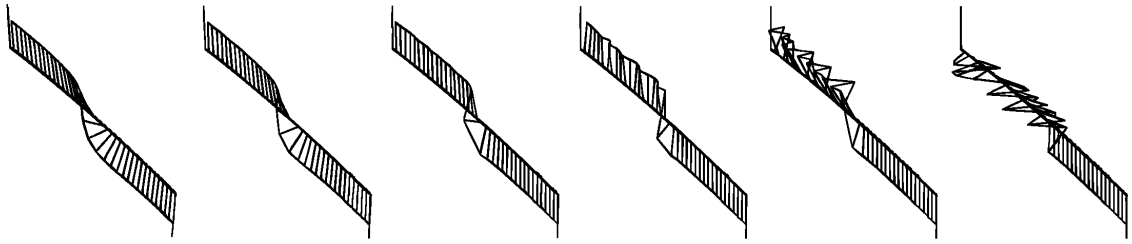

Figure 9.9:

The calculated trajectory of a UCN passing a low field region (from bottom to top) into a reversed holding field. The trajectory is calculated from z = 310 mm to z = 410 mm. The value of the external field is (from left to right) $7 \cdot 10^{-4}$ T, $4 \cdot 10^{-4}$ T, $1 \cdot 10^{-4}$ T, $5 \cdot 10^{-5}$ T, $3 \cdot 10^{-5}$ T and $8 \cdot 10^{-6}$ T. After 400 steps the polarization vector is plotted, the end of the vectors are connected to guide the eye. The longer line at the beginning of the trajectory (bottom) and at the ends is the direction of the magnetic field, which is always parallel at the beginning. It can be seen in the right pictures that for lower fields the adiabaticity is lost.

stainless steel screws, which have been measured and are non magnetic. Anyhow, significant magnetic inhomogeneities of such parts would have caused increased depolarization, instead of lower depolarization.

9.4 Cooling - the Temperature Dependence of the Losses

The cooling procedure was performed for the DLC AL-foil and the DLC PET-foil #2 samples. The gain in storage time is shown in fig. 9.10. The straight lines are the temperatures, measured (left picture) on the shield (upper curve), on the top of the sample (middle curve) and on the cold stage of the cooling machine (lower curve). On the right picture only the sensor at the upper end of the sample is shown.

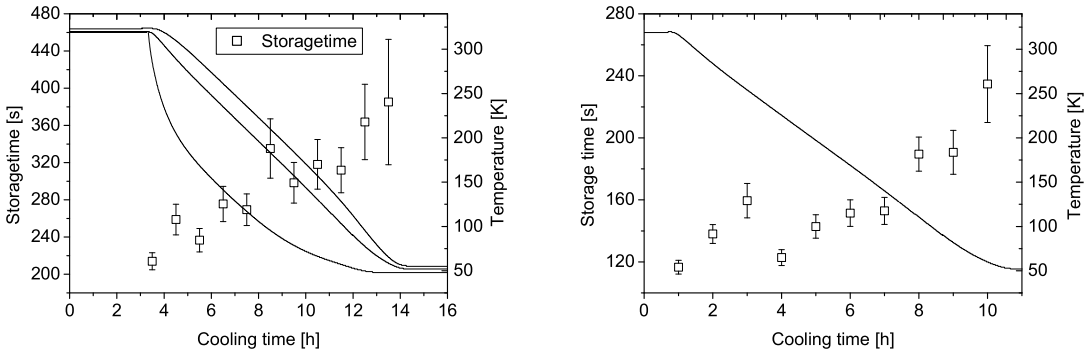

Figure 9.10:

The storage time during cooling of the DLC PET-foil #2 sample (left) and DLC Al-foil (right). For the evaluation of the storage time always consecutively one N_1 and two N_2 measurements are used. The lines correspond to temperatures and refer to the right scale.

9.4.1 Temperature Gradient on the Sample

The temperature of the sample could be measured at maximum five points on the sample tube. In the case of foils the sensors were mounted on the shells which hold the foils. In an offline measurement the temperature of the DLC PET #2 foil on the lower end was measured by a sensor that was directly mounted on the foil. At 70 K "average" temperature the sensor on the top of the sample showed 55 K, the sensor mounted directly on the lower end of the foil showed 75 K in the offline measurement. These temperatures were reached without thermal shield at the lower end of the sample.

9.5 DLC Density Measurements

The Fermi potential for the DLC coatings was determined using the technique of neutron reflectometry [71], XPS, NEXAFS, the laser-acoustic method LAwave^{TM}, UCN transmission and qualitatively also Raman spectroscopy. This is part of ongoing work at PSI [72]. For a piece of the DLC coated Al-foil used for the experiment, the transmission of UCN was measured afterwards using time-of-flight setup at ILL at the instrument PF2. As a calibration a 10 μm Cu-foil coated with Be was also measured (see fig. 9.11). From this figure one can conclude a quite similar behaviour of DLC and Be coatings. Therefore the value for the potential used for the analysis was 258 neV for all the samples.

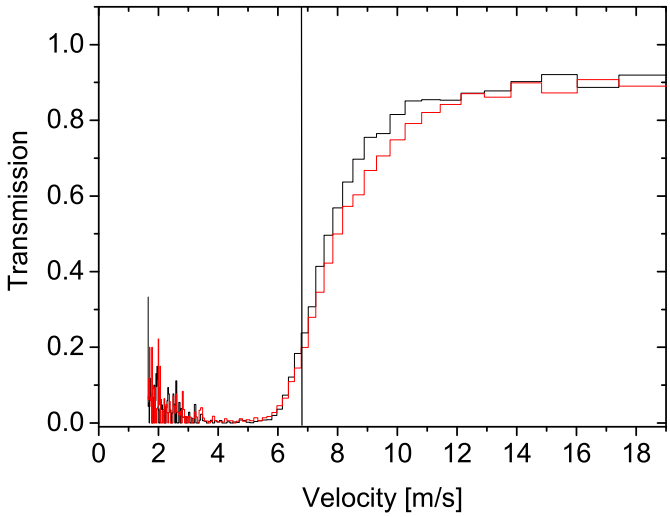

Figure 9.11:

The transmission of UCN through DLC (red) and Be (black) coated foils. The smeared out curve for DLC originates qualitatively from the thickness of the Al-foil (200 μm, compared to 10 μm for the Be coated Cu-foil).

Figure 9.12 shows the influence of the Fermi potential on the value of η. The curve is calculated by Monte Carlo simulation, where the Fermi potential was varied. The dependence is linear in this energy range. A conservative assumption of a 10 % change of the potential would lead to a change in the loss coefficient of 4 %. This results in an overall normalization uncertainty of 5 % common to all DLC loss coefficients.

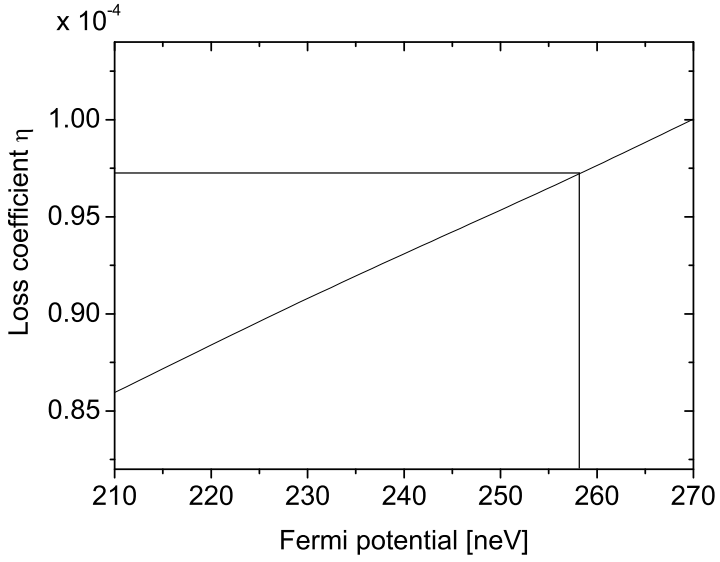

Figure 9.12:

The dependence of the wall loss coefficient on the Fermi potential. For the same measured storagetime a different value of η can be calculated using a different assumption for the value of the potential.

9.6 Dependence of the Storage Time on the Vacuum Conditions

In the estimation of the influence of the residual gases we follow the approach of [86] to calculate a collision cross section for slow neutrons and mono atomic gases. Here we focus on Nitrogen. We neglect the rotational and vibrational excitations of the N_2 molecule, which has only the translation as a degree of freedom. The major contribution of the loss is due to scattering, not due to the absorption cross section. The cross section in thermal equilibrium is

$$\langle\sigma\rangle_T \sim a^2(1+\lambda)^{-2}2\alpha\pi^{-1/2} \tag{9.5}$$

with a the bound coherent scattering length, $\alpha = (2/3)^{1/2}(v_m/v_0)$, where v_m is the mean thermal gas velocity, v_0 the incident neutron velocity and λ the ratio of the neutron mass and the weight of the scatterer. The estimated influence of the vacuum pressure on the loss for an assumed storage time of 200 s and a neutron velocity of 5 m/s is shown in tab. 9.2. By measuring the storage time at different vacuum conditions we found that below $1 \cdot 10^{-5}$ mbar the influence of the residual gases can be neglected.

9.7 Discussion of Experimental Problems

In the design of the experiment the sample tube reaches through the plane of the maximum magnetic field, in the middle of the magnet gap. Due to a mistake in mounting for the first measurements, the positions of the sample tubes were higher than the maximum magnetic field position, which caused additional losses of neutrons. A schematic drawing is shown in fig. 9.13. The parameter Δh shows the offset in height of the sample tube above the middle

Pressure [mbar]	**loss [%]**
$1 \cdot 10^{-2}$	62.1%
$1 \cdot 10^{-3}$	9.2%
$1 \cdot 10^{-4}$	1.0%
$1 \cdot 10^{-5}$	0.1%
$1 \cdot 10^{-6}$	0.0%

Table 9.2:
The relative loss depending on the residual gas pressure inside the storage volume for a storage time of 200 s.

of the magnet gap. The position offset could be reproduced after the measurements and was found $\Delta h = 42.5 \pm 2.5\,\mathrm{mm}$. At the connection between the vertical guide and the sample tube UCN are lost due to a non-coated edge of the sample and due to a possible mechanical that slit absorbed neutrons. Neutrons which hit the iron neutron guide below the connection were absorbed with a probability of $\sim 10^{-2}$ per collision. The consequences and the resulting correction for the analysis is described in the following. It was found by simulation that the connection between the tubes caused the largest influence on the storage behaviour:

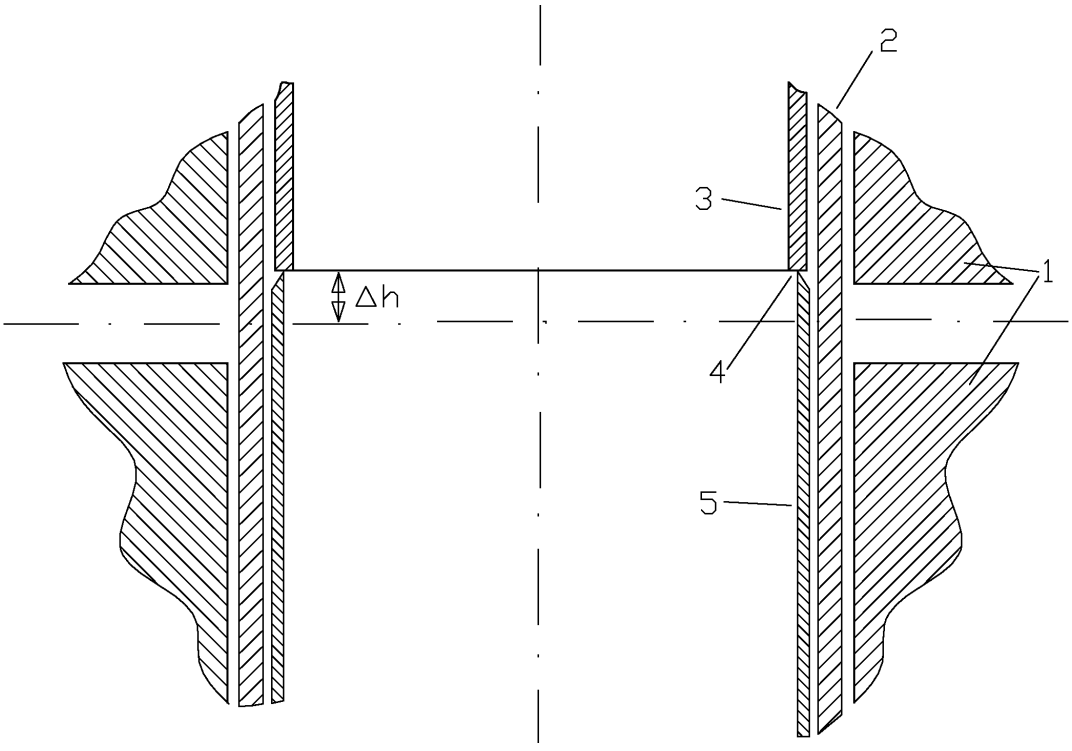

Figure 9.13:
Cut through the sample and the vertical guide relative to the magnet poles. [1] magnet poles, [2] vacuum housing, [3] sample tube, [4] uncoated edge, [5] stainless steel guide. The vertical line is the axis of symmetry, the horizontal line denotes the middle plane of the magnet gap, where the field barrier for neutrons reaches its maximum value.

- High UCN energies. Stored UCN with high energies can reach deeper into the magnetic field barrier and can therefore also "see" the uncoated edge of the sample and the mechanical connection. The number of collisions at this position is > 0.2 Hz per neutron for all energies that can reach this position. The diameters of the sample and the guide tube are different (70.0 mm for the sample and 71.1 mm for the guide). The slit domintates the losses if it is larger than about 0.05 mm. After a cleaning time of 100 s the part of the spectrum with energies high enough to reach the slit has disappeared completely. This causes a lower cut-off in the energy spectrum for the storage at level 0 (83.4 neV cleaning) at 62 neV. The resulting spectrum is shown in fig. 9.14. This spectrum is used for the analysis of the samples BE Al-tube PNPI, BE Al-tube TUM and DLC Al-tube VT.

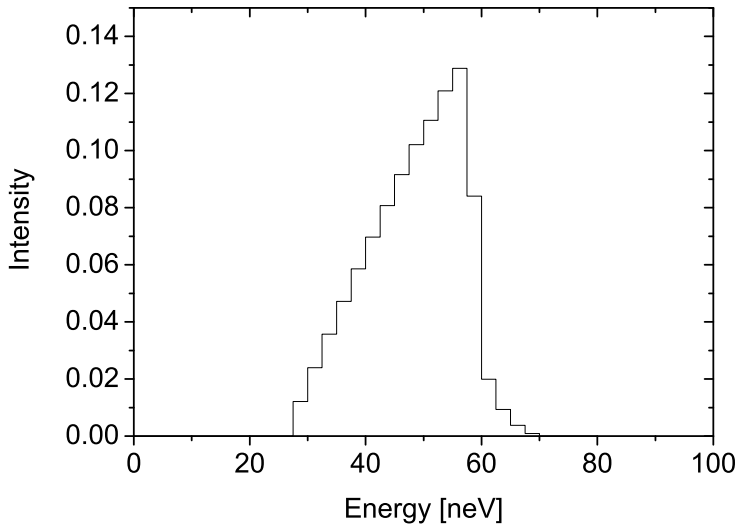

Figure 9.14:

The spectrum for the samples that were mounted too high. The upper energy cut-off is at 62 neV. This is due to losses in the lower regions of the storage volume, caused by a slit in the mechanical connection of the sample to the stainless steel guide from below.

- Low field barriers. At measurements with lower magnetic field strengths (level 3 and 4) the absolute value of the field decreases faster with height. Therefore also UCN with low energies see the mechanical connection and get lost, the situation is then similar to above.

The mechanical position for all misaligned samples was the same. This can be shown by extrapolating the number of neutrons measured at time t_1 to t = 0, using the corresponding storage time. The results are shown in tab. 9.3. A comparison of the extrapolated number of neutrons at t = 0 for a misaligned sample to the number stored in a regularly mounted sample with a full spectrum shows a ratio of 0.35. This corresponds to the ratio of the spectrum shown in fig. 9.14 and the area of the spectra for level 0. The same samples were subject to problems during cooling. For the badly mounted samples a slit between the sample and the vertical guide opened during cooling, where the neutrons escaped. Fortunately these problems could be solved during the reactor cycle.

BE Al-tube TUM 300 K	802 ± 6.4
DLC Al-tube VT 300 K	781 ± 8.5
BE Al-tube PNPI 1 300 K	767 ± 15.6
BE Al-tube PNPI 2 300 K	772 ± 15.8

Table 9.3:
The extrapolated number of neutrons in the spectral range which can be stored, where 1 and 2 describe the same sample mounted at two different times.

Chapter 10

Discussion

In the following we discuss the results and give possible explanations. The interpretation is split into a discussion of the loss coefficients and a discussion of the depolarization parameters. Finally, we try to reconcile the measurements in a consistent model.

A compilation of measured values for the losses and the depolarization is listed in tab. 10.1. The values are averaged over the different energy level measurements. If the error bars were asymmetric, they were averaged. The depolarization probabilities are also given as average numbers, weighted over different energy level measurements for both methods. The values for both methods are again averaged.

Sample	**Loss coefficient** η_{av}	**Depolarization** β_{av}
DLC on Al-foil at 70 K	$1.73^{+0.09}_{-0.09} \cdot 10^{-4}$	$0.80 \pm 0.25 \cdot 10^{-6}$
DLC on Al-foil at 300 K	$3.52^{+0.06}_{-0.06} \cdot 10^{-4}$	$0.70 \pm 0.21 \cdot 10^{-6}$
DLC on PET-foil #1 June at 300 K	$3.78^{+0.72}_{-0.55} \cdot 10^{-4}$	$4.24 \pm 0.72 \cdot 10^{-6}$
DLC on PET-foil #1 May at 300 K	$2.15^{+0.28}_{-0.24} \cdot 10^{-4}$	$10.1 \pm 1.63 \cdot 10^{-6}$
DLC on PET-foil #2 at 70 K	$0.72^{+0.12}_{-0.12} \cdot 10^{-4}$	$15.7 \pm 0.89 \cdot 10^{-6}$
DLC on PET-foil #2 at 300 K	$1.63^{+0.10}_{-0.10} \cdot 10^{-4}$	$15.1 \pm 0.96 \cdot 10^{-6}$
Be on Al-tube, PNPI at 300 K	$4.23^{+0.31}_{-0.28} \cdot 10^{-4}$	$11.8 \pm 0.50 \cdot 10^{-6}$
Be on Al-tube, PNPI at 380 K	$5.04^{+0.42}_{-0.37} \cdot 10^{-4}$	$9.39 \pm 2.18 \cdot 10^{-6}$
Be on Quartz-tube, PNPI at 300 K	$5.02^{+0.08}_{-0.08} \cdot 10^{-4}$	$9.17 \pm 1.41 \cdot 10^{-6}$
Be on Al-tube, TUM at 300 K	$6.81^{+0.26}_{-0.25} \cdot 10^{-4}$	$7.83 \pm 0.35 \cdot 10^{-6}$
DLC on Al-tube, VT at 300 K	$5.83^{+0.28}_{-0.26} \cdot 10^{-4}$	$10.90 \pm 0.30 \cdot 10^{-6}$

Table 10.1:
The values for η and β for all different samples. For the foil samples the results are averaged from different energy level measurements. The values for β are averaged over energies for both methods and over both methods.

10.1 Loss Coefficient

The measured temperature dependence of η for the DLC PET-foil #2 sample is shown in fig. 10.1. From this figure a linear dependence of the losses on the temperature can be estimated. Other expected behaviours known from literature, e.g. $\sim \sqrt{T}$, [18], p. 37f, are also in agreement with the error bars. The main conclusion from this figure is that the loss η includes a temperature dependent part, whereas the depolarization β is temperature independent.

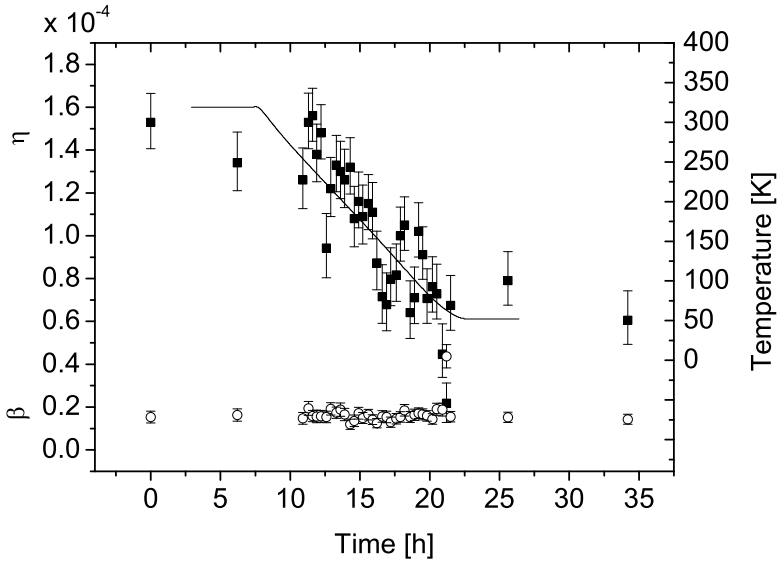

Figure 10.1:

The measured dependence of η on the average sample temperature. The sample used for this measurement is the DLC PET-foil #2. The solid line is the (average) temperature of the sample, the solid squares are the measured values for η, the open circles are the depolarization probability.

All our measurements showed losses that are significantly higher than the theoretically predicted values at low temperatures. This behaviour is also reported in literature: for comparison, the best measured value for Be-coated surfaces at low temperatures is $(3\pm1)\cdot10^{-5}$ [37]. This was achieved by baking at 620 K under He atmosphere for long times (> 28 h). In our experiment the samples were taken directly from the production process, without any special treatment before the measurements. The loss coefficient of DLC, which was for the first time measured in this experiment, is a factor of 2.6 lower than Be in the direct comparison.

10.1.1 Theoretical Prediction of the Loss Coefficient

The loss consists of a temperature independent part η_0 and a temperature dependent part η_T. The temperature independent part due to absorption can be calculated by using eq. 2.18,

$$\eta_0 = \frac{\sigma_l k}{4\pi a_B} \tag{10.1}$$

where the bound coherent scattering length a_B is taken from ref. [87], and the loss cross section σ_l is the absorption cross section σ_a from ref. [88] at a velocity corresponding to a wave number k. Based on this, the predicted loss coefficient for Be is $\eta_0 = 2.7 \cdot 10^{-7}$ and for DLC $\eta_0 = 1.25 \cdot 10^{-7}$.

Substance	Θ_D **[K]**	$\mathbf{T}_s$ **[K]**	σ_a**[barn]**	σ_{el} **[barn]**	σ_{ie} **[barn]**	η **x** 10^{-5}
^{12}C (98.9 %)			0.0035	5.55		
^{13}C (1.1 %)			0.00137	4.84		
C (graphite)	402	70	0.0035	5.55	6.6	0.06
C (DLC)	1200	70	0.0035	5.55	0.3	0.017
C (diamond)	1860	70	0.0035	5.55	0.09	0.015
C (graphite)	402	300	0.0035	5.55	173	1.12
C (DLC)	1200	300	0.0035	5.55	35	0.25
C (diamond)	1860	300	0.0035	5.55	10	0.1
Be	1440	70	0.0076	7.63	0	0.03
Be	1440	300	0.0076	7.63	140	0.3

Table 10.2:

Theoretical predictions of the loss coefficients. The parameter Θ_D is the Debye temperature, T_s is the sample temperature, the scattering cross section σ_{el} is the sum of the coherent and the incoherent scattering cross section following the incoherent approximation [89]. The value for DLC at room temperature depends on the Debye temperature, which here is chosen in between the value for graphite and for diamond.

The temperature dependent loss coefficient η_T can be determined by calculating the interaction probability with phonons in a simple one-phonon Debye model, as it is described in sec. 2.1.3. By absorbing a phonon during a wall interaction, the neutron gains energy and is not stored any more. The calculation is based on eq. 2.26:

$$\sigma_{ie} = \frac{\sigma_{el}}{M}\frac{1}{k_i}\int_0^{\omega_D} d\omega\sqrt{\omega}g(\omega)n(\omega,T)e^{-W(\omega,T)} \tag{10.2}$$

This cross section is added to the absorption cross section in eq. 2.18. We assume that the surface layer is thick enough to be treated like bulk material (> 1000 Å), with its own Debye temperature. This is 402 K for Carbon and 1860 K for diamond. For DLC we use 1200 K, to give an idea of the influence of this parameter on σ_{ie}. Following the incoherent approximation (eq. 2.24), the elastic scattering cross section is the sum of the coherent and incoherent scattering cross section:

$$\sigma_{el} = \sigma_{coh} + \sigma_{inc} \tag{10.3}$$

The scattering cross section is dominated by the coherent part for C and Be. A list of calculated loss coefficients, using eq. 2.26, is shown in tab. 10.2.

10.1.2 Possible Contributions to the Losses

The predicted losses for DLC are much lower than the measured values, similar to the behaviour of Be mentioned above. In the following we discuss possible reasons for the increased losses.

In our setup, false loss channels like mechanical slits or mechanical connections are absent. Losses originating from low energy heating on wall reflections and magnetic field fluctuations are discussed in sec. 9.2 and sec. 9.3. These effects are not of concern in our measurements. We found no indication for other possible loss channels, like acoustic vibrations, as they are discussed in refs. [28, 29] and ref. [30], p. 175ff.

Hydrogen Contamination

The mass of Hydrogen is similar to the mass of the neutron and it can therefore exchange a large momentum with the neutron on scattering. It has a large scattering cross section of 82 barn. From this, 80 barn are the incoherent cross section which also causes spin flip on scattering (see sec. 10.2). The absorption cross section is 0.33 barn for thermal neutrons, which gives for a neutron velocity of 3.56 m/s (the average velocity of the stored neutrons at level 0) already a value of 204 barn. These values make it a good candidate to explain the temperature dependent losses of UCN on surfaces. The inelastic cross section can be estimated by using the usual formalism to calculate temperature dependent up-scattering, by applying the incoherent approximation (eq. 2.24) to eq. 2.26. In our case, we assume that the Hydrogen is strongly bound to the material and use the same properties as for the bulk material, i.e. a mass ratio of 13, as it is used for Carbon. We use the mass ratio as the free parameter to define the strength of the chemical bond of Hydrogen and Carbon. Then the loss cross section for thermal velocities is around 0.5-7 barn, for a Debye temperature in a range between 402 K and 1860 K. For a neutron with 3.56 m/s this gives already a value of 300 barn for an assumed Debye temperature of $T_D = 1200$ K. These numbers are in agreement with the estimation given in ref. [42].

It is known that Hydrogen is absorbed inside the bulk material and adsorbed on surface (see e.g. ref. [90]), and is therefore seen also by the neutrons. The typical amount of contamination of surfaces with Hydrogen is found to be in the order of up to $(2-3)\cdot 10^{16}$ atoms/cm^2 [91] for stainless steel and Copper. For very slow neutrons, the penetration depth into materials is about 50 Å, calculated using eq. 2.15. Distributed over the penetration depth, this number of atoms per area corresponds to a density of $(2-4)\cdot 10^{22}$ atoms/cm^3 in the upper layers of the material. For Be a similar value was found by ref. [35]. Tests on the Hydrogen content of our coatings have been carried out by Korobkina et al. [92], which gives evidence that the coatings contain Hydrogen on the percent level, i.e. a few times 10^{21} per cm^3.

A variation of the Hydrogen content in the upper layers of the surface coating would allow for tuning any loss coefficient. Nevertheless the concentration that would be necessary is ten times higher than the indication from ref. [92].

Pin Holes

Figure 10.2 shows microscope pictures of a typical surfaces of DLC and Be samples [93].

- For the DLC coated Al-foil the fraction of uncoated areas is estimated to be $< 5\cdot 10^{-5}$. Colors surrounding the spots are a sign for a hole in the coating [94], whereas black spots seem to be small pieces of "dirt" deposited during the sputtering process. The increase of losses due to the holes can be estimated by assuming that neutrons that see the $\sim$15 nm Titanium interface layer between the coating and the substrate, are lost from the storage volume. This is caused by the negative scattering length of Ti, $a_B = -3.44$ fm. The loss coefficient for the DLC Al-foil becomes then

$$\eta \leq \frac{(\sigma_{aC} + \sigma_{ieC}(T))\cdot k}{4\pi a_B} + \eta_h \tag{10.4}$$

  which is strongly dominated by the holes $\eta_h = 5\cdot 10^{-5}$ and results in a calculated $\eta_{300K} = 5.25\cdot 10^{-5}$ and $\eta_{70K} = 5\cdot 10^{-5}$, respectively. Here $\sigma_{a,C}$ is the absorption and $\sigma_{ieC}(T)$ the inelastic scattering cross section of Carbon.

- The DLC PET-foil has less visible holes, $< 1\cdot 10^{-5}$. The material PET (Polyethylene Terephthalate) with a chemical formula of $[8OOC8C_6H_48COO8CH_2CH_28]_n$ results in a small positive average scattering length of 2.7 fm. The Fermi potential is about 13 neV

and therefore only a small fraction of the neutrons that hit the hole surface will therefore be reflected.

- For magnetron sputtered Be coatings (lower left), the holes on the surface are in the order of $1 \cdot 10^{-4}$. The picture shows a big hole in the coating, where the copper substrate is visible. Experimental work on this topic is also published, the results are on a similar level, as shown in refs. [95, 96].

Pin holes in the coating contribute to the losses in the worst case proportional to the uncoated surface fraction. Nevertheless, using the upper limits of holes in our coatings, this is not the parameter that explains the losses.

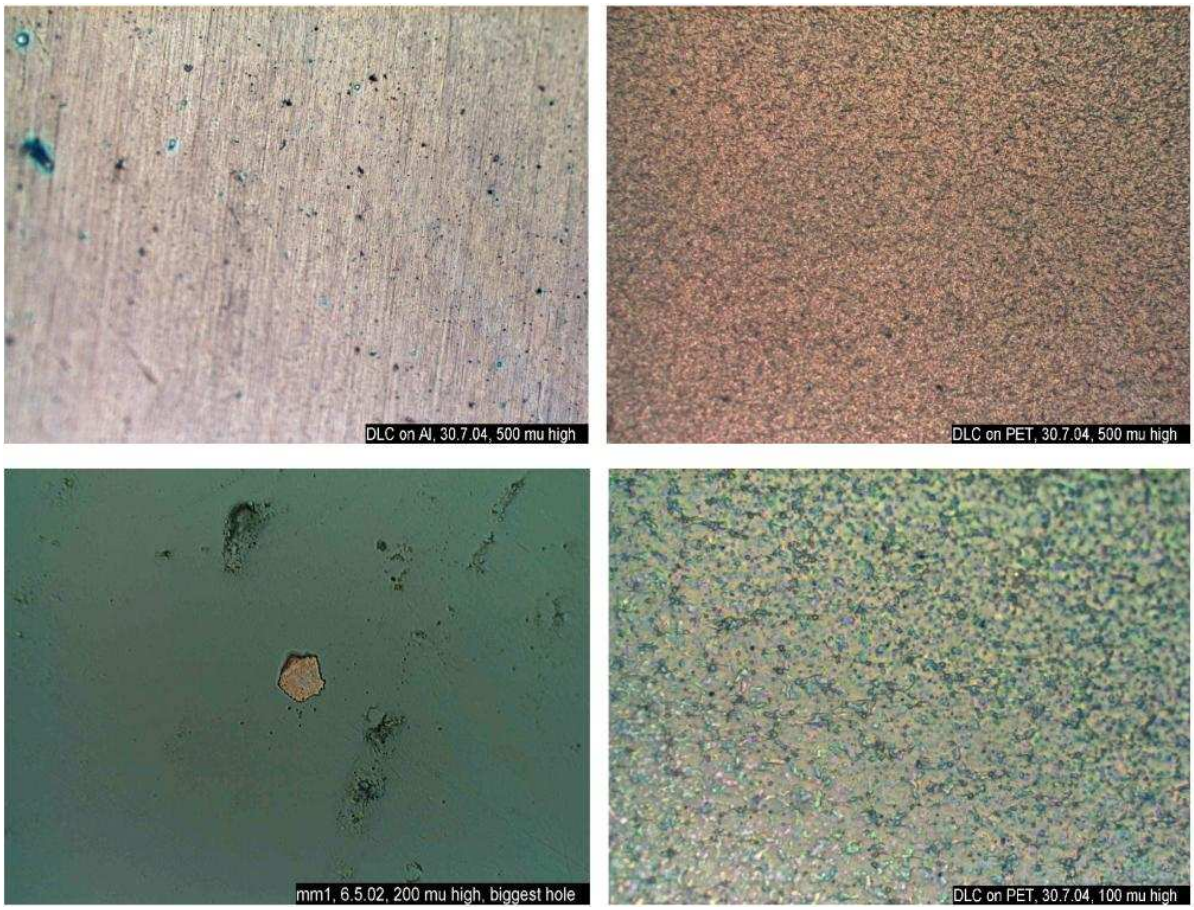

Figure 10.2:

Typical surfaces of a DLC coated Al-foil (upper left) and a DLC coated PET-foil (upper right). The Al foil sample is slightly bent, therefore not the whole range of the picture is clearly in focus. The height of each picture is 500 μm. The lower right picture is a zoomed picture of the PET-foil, height 100 μm. As a comparison, a Be coated surface is shown (lower left), 200 μm.

Surface Roughness

The surface roughness was treated e.g. by ref. [97]. The resulting formula can be applied for a wide range of situations.

$$\mu = \mu_0 \left(1 + \frac{2\sigma^2 \mathbf{k}_c^2}{1 + 0.85\mathbf{k}_c\omega + 2\mathbf{k}_c^2\omega^2}\right)^{1/2} \tag{10.5}$$

where μ_0 is the loss probability on a perfectly smooth surface, $\mathbf{k}_c = \sqrt{2mV_F/\hbar^2}$ the critical wavenumber. The parameter σ is the RMS of Gaussian shaped disturbances and ω the correlation length, or for practical purposes the distance between disturbances on the surface.

Atomic force microscope pictures of the DLC Al-foil and the DLC PET-foil are shown in fig. 10.3. From these pictures a surface profile can be determined. In fig. 10.4 surfaces profiles of the DLC Al-foil (upper figure) a the DLC PET-foil are shown. From the profile of the DLC Al-foil also the size of typical "dirt" particles can be determined. Excluding these "dirt" particles from our roughness estimation, the DLC PET-foil has an average roughness of $R_a = 100\,\text{nm}$, a maximum roughness of $R_{max} = 300\,\text{nm}$ and a correlation length of 2-5 μm. For DCL Al-foils we found $R_a = 15\,\text{nm}$, $R_{max} = 95\,\text{nm}$ and a correlation length of about $1\,\mu\text{m}$. The PET-foil is much rougher than the Al-foil. Using eq. 10.5, we get a negligible enhancement of the losses of $< 1\,\%$. However, the DLC PET-foil shows better storage properties. Therefore it seems that for our DLC coated foils the losses are not dominated by the roughness parameter.

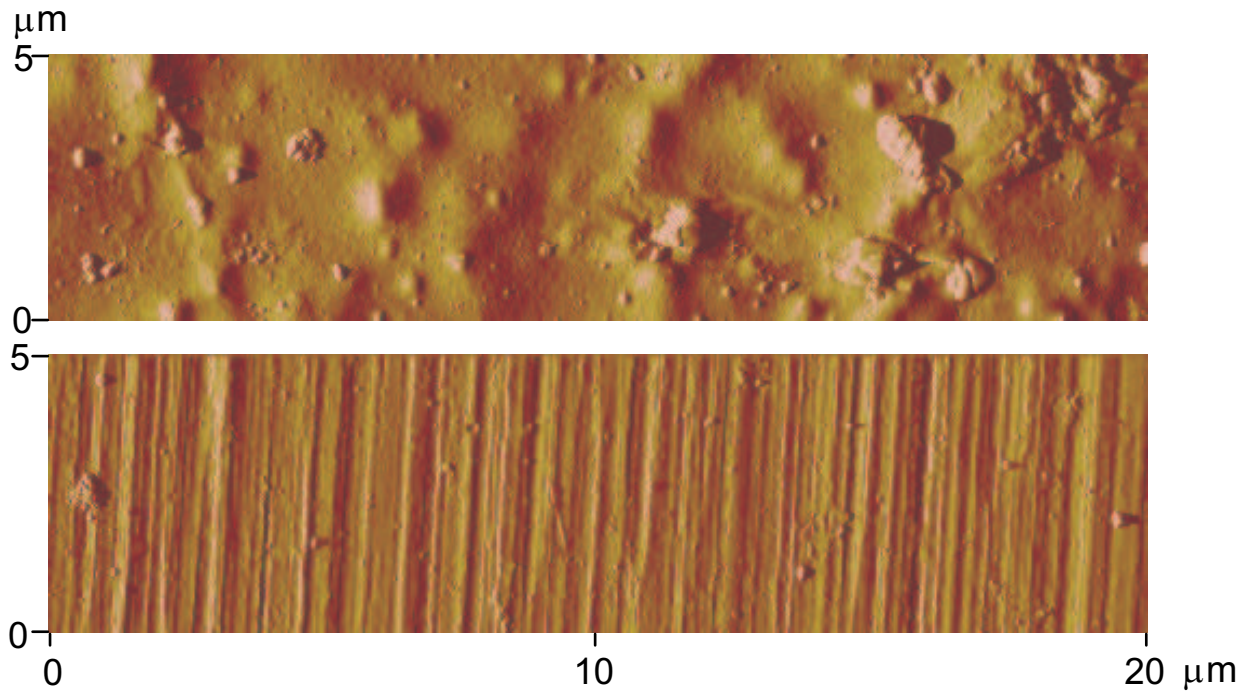

Figure 10.3:

Atomic force microscope pictures of DLC on PET (top) and DLC on Al-foil (bottom). The average roughness over $20\,\mu m$ of the DLC PET-foil is $R_a = 100\,\text{nm}$, for DCL Al-foil $R_a = 15\,\text{nm}$.

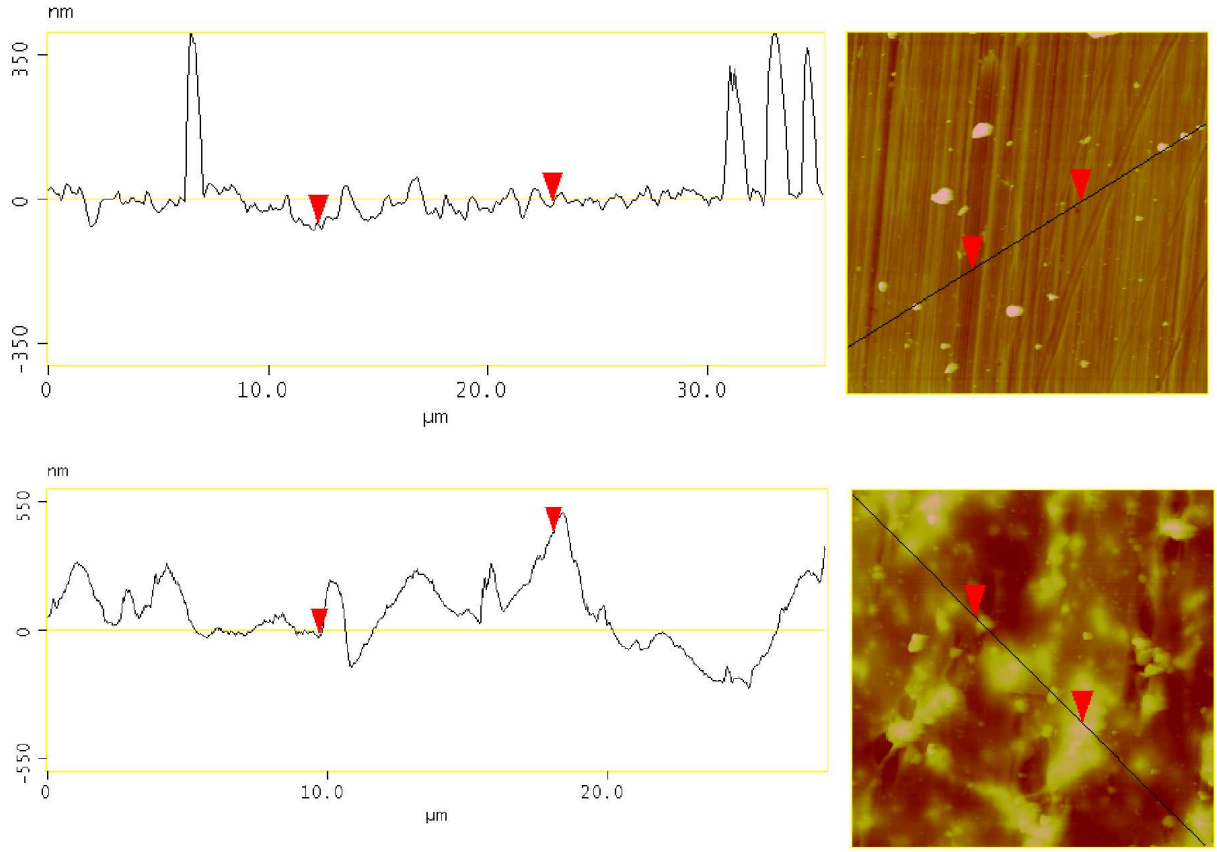

Figure 10.4:

The surface profiles of DLC Al-foil (top) and DLC PET-foil. On the upper picture also the size of the "dirt" particles can be determined.

"Dirt" Particles

A more detailed investigation of fig. 10.2 shows that the DLC Al-foil (upper left) has a large amount of "dirt" particles with a diameter of $\sim 300-1000$ nm (see fig.10.4) and similar height, which are deposited during the coating process. It is therefore most likely that these particles are made of graphite. They cover a surface ratio of $\sim 5 \cdot 10^{-4}$. These particles cause an increased loss coefficient: If these particles are graphite, they have a lower Debye temperature (402 K) and consequently a larger inelastic scattering cross section at room temperature. Additionally, graphite with low density is hydrophilic [98]. Adsorbed and absorbed Hydrogen can cause increased losses here.

The DLC PET-foil does not show "dirt" pieces on the same level, the structure is in general much rougher, and the particles could be embedded in the structure and therefore not so easily visible.

Boron Contamination

Boron is contained in every Carbon material, and is therefore of major concern for our DLC layers. It has an absorption cross section of 767 barn for thermal neutrons, compared to 0.0035 barn for Carbon [87, 88]. An investigation of the Boron content of our DLC foils using SIMS (Secondary Ion Mass Spectroscopy) [99] gives an upper limit of the Boron content < 30 ppm.

Since the absorption cross section is dominating ($\sigma_a = 767$ barn), we only consider absorption. The corresponding loss coefficient for < 30 ppm Boron addition, calculated according to eq. 2.18, is then $< 1 \cdot 10^{-6}$ per wall collision. This value is not of concern for our measurements.

10.2 Depolarization Probabilities

Recent measurements on the depolarization probability per wall collision on various materials of Serebrov et al. [100] and the remeasured values [101] showed a depolarization on the same level, $(1-2) \cdot 10^{-5}$, as it was observed in our measurement for most samples. The remeasured values are larger than the earlier findings. The depolarization of various coatings was measured by storing neutrons in a material trap, see fig. 10.5. A spectrum of neutrons was prepared in a so-called gravitational spectrometer. The neutrons are filled from the spectrometer through a 4.5 T superconducting solenoid into a trap, which contains the sample surface. Only polarized neutrons can pass the solenoid. These neutrons are now stored in the trap. After a storage time in the order of 10^2 s, the neutrons are allowed to exit the trap through the solenoid. Only neutrons that preserved their spin can exit the trap, spin flipped ones stay inside. These neutrons are emptied to a detector. Data from this measurements are shown in tab. 10.3. Water vapor, which was frozen on the graphite coated trap in a special measurement, contributed to the losses, but no influence on the depolarization probability could be observed. The measured values for Be are in agreement with our extracted values.

In an experiment by Makela et al. [102], p. 184ff, measurements based on a different method were performed. Neutrons are polarized and analyzed with a superconducting magnet, the storage volume for the polarized neutrons is coated with the surface to be tested. Emptying of the bottle is done using a spin flipper. In the latter experiment the sample was DLC on a quartz-tube from VT. Preliminary results for DLC coated quartz-tubes seem to be in the order of $1 \cdot 10^{-6}$ per collision. Our DLC coated quartz-tube from VT (which was produced some years later) showed a significantly higher value of of $\beta = 10.9 \pm 3 \cdot 10^{-6}$.

As it is shown for the DLC PET-foil #2 in fig. 10.1, in our measurements no temperature dependence of the depolarization β could be observed. Also no energy dependence was measured on our level of accuracy.

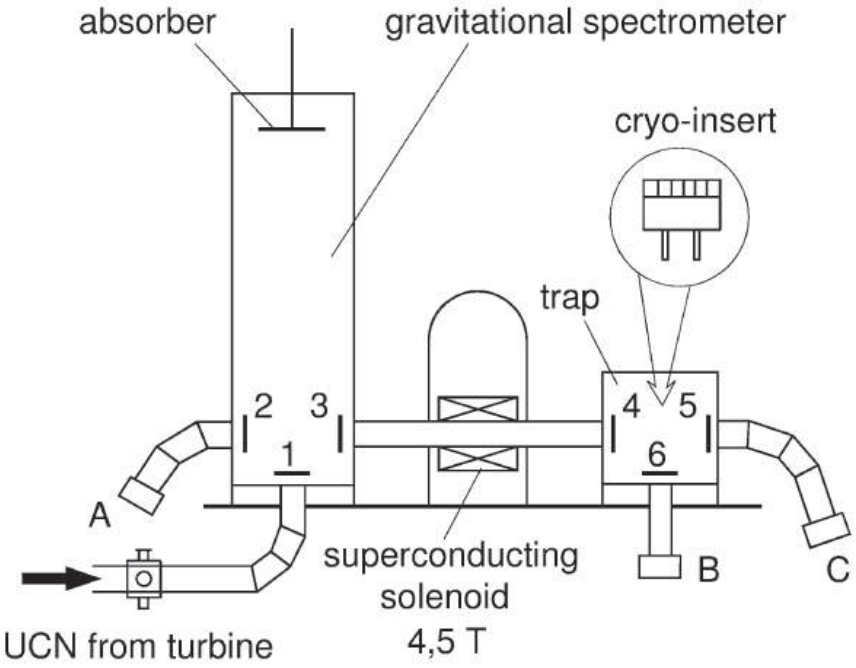

Figure 10.5:

The setup of the experiment by Serebrov et al. [100]. A detailed description is given in the text.

Material	$\beta \times 10^{-6}$
Be - trap	7.2 ± 0.7
Be - trap and foils	10-20
Cu	~ 1
C	6-10
Fomblin, Teflon	6 ± 2
BeO	38 ± 3

Table 10.3:

Some values taken from the first and second measurement of depolarization probabilities from refs. [100, 101].

10.2.1 Origin of the Depolarization

A false effect that could be observed is depolarization during low field transitions. For such an effect an maximal value of $\beta = 1 \cdot 10^{-8}$ per wall collision can be calculated, as it is discussed in sec. 9.3.1.

One physical origin of the depolarization on wall collision is incoherent scattering. The dependence of spin flip on the scattering cross section is given in refs. [50, 103], who predict a 2/3 ratio of the spin flip cross section to the incoherent cross section. From this one would expect a spin flip probability of $1 \cdot 10^{-10}$ per wall collision for Be and even less for Carbon. This number is estimated by the formalism shown below. Some incoherent cross sections related to our samples are given in tab. 10.4.

Isotope	σ_{inc} **[barn]**
^{12}C	0.0
^{13}C	0.034
Be	0.0018
H	80.3
B	1.7
N	0.5

Table 10.4:
Hydrogen shows the only relevant incoherent cross section, the cross section of Boron is small due to the low concentration in Carbon <100 ppm. The values of the cross sections are taken from ref. [88].

Hydrogen

The cross section for incoherent scattering is connected with spin flip, as it is shown in refs. [50, 103]. The cross section for spin flip is

$$\sigma_{fl} = \frac{2}{3}\sigma_{inc} \tag{10.6}$$

and without spin flip

$$\sigma_{nofl} = \sigma_{coh} + \frac{1}{3}\sigma_{inc}. \tag{10.7}$$

From this the probability that a spin flip on incoherent nuclear scattering can occur can be derived [104]:

$$P = \frac{\sigma_{fl}}{\sigma_{fl} + \sigma_{nofl}} = \frac{\sigma_{inc}}{\sigma_{coh} + \sigma_{inc}}. \tag{10.8}$$

If the depolarization is based on Hydrogen, the ratio of the temperature dependent loss coefficient η_T at T = 0 K and the depolarization at room temperature can be estimated following ref. [42],

$$\frac{\beta}{\eta_T} \sim \frac{\sigma_{fl}}{\sigma_{ieH}} = \frac{2/3 \cdot \sigma_{inc}}{\sigma_{ieH}}. \tag{10.9}$$

The ratio depends on the chemical bonds of the protons to the surface, this possible connection of depolarization and losses is discussed below (sec. 10.3).

10.3 A Model to Describe the Measurements

In the following we try to explain the values for the loss coefficient η and the depolarization probabilitiy β in a model. The main problem is the difference in loss and depolarization behaviour of the DLC coated PET-foil, $\eta(300K) = 1.63 \pm 0.1 \cdot 10^{-4}$ and $\beta = 1.5 \pm 0.1 \cdot 10^{-5}$, compared to the DLC coated Al-foil, $\eta(300K) = 3.52 \pm 0.1 \cdot 10^{-4}$ and $\beta = 0.8 \pm 0.1 \cdot 10^{-6}$.

The basic idea is to mix Hydrogen into the DLC layer. Investigations of surfaces, e.g. refs. [31, 34–36], showed Hydrogen concentrations of typically $(2-3) \cdot 10^{16}$ per cm^2 on Beryllium, Copper and stainless steel surfaces, this is again for a penetration depth of typically 5 nm a density of $(2-4) \cdot 10^{22}$ atoms/cm^3, compared to the density of Carbon $> 1 \cdot 10^{23}$ per cm^3, as discussed in sec. 10.1.2.

10.3.1 Hydrogen and Thermal Up-Scattering

In our model we add Hydrogen to the DLC bulk material and calculate a thermal up-scattering cross section, following the approach shown in sec. 10.1.1. This is based on the assumptions listed below, and is speculative.

Graphite and diamond have a crystalline structure and therefore a Debye temperature Θ_d and phonons. Up-scattering occurs when a phonon is absorbed by a neutron during a wall collision. In order to estimate the probability of the interaction with a phonon, several parameters have to be chosen. One major assumption is, that we can interpolate the value of Θ_d between 402 K for graphite (2.25 g/cm^3) and 1860 K for diamond (3.5 g/cm^3) linearly. Further, we assume that also in DLC phonons can be (de-)excitated. The strength of the chemical bond of Hydrogen to the uppermost layers of DLC is not known[1], as it is also stated in literature, see e.g. [36], and the strength of the bond is therefore a free parameter in the model.

10.3.2 Estimated Loss Channels

The loss coefficient η_{tot} is calculated by summing the cross sections due to nuclear absorption of Carbon σ_{aC}, the nuclear absorption of Hydrogen σ_{aH}, the inelastic scattering of of Carbon $\sigma_{ieC}(T)$ and the inelastic scattering of Hydrogen $\sigma_{ieH}(T)$. According to the amount of Hydrogen, also the averaged bound coherent scattering length a_B of the uppermost layers changes, which influences the Fermi potential linearly. The values of σ_{ie} are calculated by integrating eq. 2.26, see sec. 10.1.1. The Debye temperature is related to the sp^3/(sp^2+sp^3) ratio of the surface coating. Then eq. 10.1 becomes

$$\eta_{tot} = \frac{(\sigma_{aC} + \sigma_{aH} + \sigma_{ieC}(T) + \sigma_{ieH}(T)) \cdot k}{4\pi a_B} + \eta_h + \eta_{aloss}. \tag{10.10}$$

The full description of the losses includes also a contribution from pin holes in the coating η_h and a contribution of the "anomalous" losses η_{aloss}, which is taken as known from literature, see e.g. ref. [37]. For the DLC coated PET-foil sample the different channels of the losses are illustrated in fig. 10.6. The coating has an assumed Debye temperature of 1350 K, corresponding to the measured sp^3 ratio of $\sim$0.6. The amount of Hydrogen is $1.6 \cdot 10^{23}$ per cm^3, which amounts to about the same number density as for the DLC within the first 5 nm. The results of this calculation are given in fig. 10.6, together with our experimental results.

10.3.3 Estimation of the Depolarization

In sec. 10.2.1 we show that the depolarization β is related to incoherent scattering. Therefore the amount of Hydrogen determines the value of β. The simultaneous measurement of β and η puts constraints on the possible range of Hydrogen concentration and the strength of the chemical bond.

The value of η caused by Hydrogen, η_T, can be estimated from measured data by extrapolating the value at 300 K and 70 K to T = 0. The values are shown in tab. 10.5.

Using the extrapolated value for η_T, we determine the amount of Hydrogen that produces values for η and β consistent with the measured values. The expected value for β is calulated according to eq. 10.9 by the ratio of $\sigma_{ieH}(300K)$ and σ_{fl}. Here, $\sigma_{ieH}(300K)$ was calculated for the average energy of the UCN in our bottle, 66 neV. The cross section for spin flip is, following sec. 10.2.1, $\sigma_{fl} = 2/3 \times \sigma_{incH}$, where $\sigma_{incH} = 80$ barn:

$$\beta = \frac{2/3\sigma_{incH}(300K)}{\sigma_{ieH}} \cdot \eta_T \tag{10.11}$$

[1] The strength of the chemical bond of Hydrogen to Carbon is discussed in literature, see e.g. ref. [105].

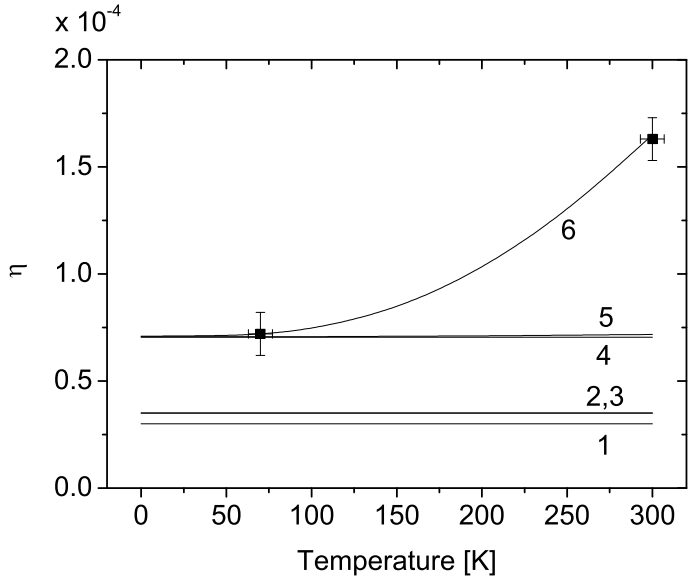

Figure 10.6:

Illustration of the loss channels for DLC on PET-foil. Line [1] shows the contribution of the so-called anomalous losses, i.e. the lowest loss value measured for Beryllium, [2] the contribution from holes in the coating, [3] the absorption from Carbon (not visible on this scale), [4] the absorption of Hydrogen, [5] the inelastic scattering on DLC and [6] inelastic scattering on Hydrogen. The points with error bars are the experimental values.

Sample	**Temperature [K]**	η	β
DLC Al-foil	300	$3.52 \cdot 10^{-4}$	
DLC Al-foil	70	$1.73 \cdot 10^{-4}$	
	contribution of H (η_T)	$1.9 \cdot 10^{-4}$	$0.75 \cdot 10^{-6}$
DLC PET-foil #2	300	$1.63 \cdot 10^{-4}$	
DLC PET-foil #2	70	$0.72 \cdot 10^{-4}$	
	contribution of H (η_T)	$1 \cdot 10^{-4}$	$15.4 \cdot 10^{-6}$

Table 10.5:

Listing of the measured values of η and β. The error bars are neglected here. The values for β are averaged over different measurements of the same sample. The contribution of Hydrogen, η_T, is the extrapolation of the temperature dependent upscattering rate to T = 0.

The Debye temperature Θ_d is assumed linear to the density of the coating, i.e. linear with the sp^3 content of the coating, which is determined using XPS. Free parameters are the strength of the bond of Hydrogen to the matrix atoms, the parameter describing this is the mass ratio of m_H/m_n, and the amount of Hydrogen. The model works for the DLC Al-foil with $\Theta_d = 950\,\mathrm{K}$, corresponding to the measured sp^3 content of 40 % and a mass ratio of $m_H/m_n = 1$. The loss coefficient becomes $\eta(\sigma_{ieH}) = 1.8 \cdot 10^{-4}$ and $\beta = 9.7 \cdot 10^{-7}$, which is in good agreement with the experiment. The DLC PET-foil #2 has a higher density of $\sim 65\,\%$ sp^3, corresponding

to $\Theta_d = 1350\,\mathrm{K}$. Agreement with experiment can only be found if the strength of the bond of Hydrogen is strongly increased in the model. If the mass ratio is $m_H/m_n = 6.5$, the calculated values become $\eta(\sigma_{ieH}) = 9.3 \cdot 10^{-5}$, and $\beta = 13 \cdot 10^{-6}$. The difference of the depolarization for the two samples is also in agreement with recent measurements using SIMS [99], which indicate a ten times higher Hydrogen content in the DLC layer on the PET-foil campared to the Al-foil. The parameters that were used in the model are shown in tab. 10.6.

Sample	Θ_d $[K]$	m_H/m_n	$\eta(\sigma_{ieH})$	β	N_H $[1/cm^3]$
DLC Al-foil	950	1	$1.8 \cdot 10^{-4}$	$0.97 \cdot 10^{-6}$	$3.28 \cdot 10^{22}$
DLC PET-foil #2	1350	6.5	$0.93 \cdot 10^{-4}$	$13 \cdot 10^{-6}$	$1.6 \cdot 10^{23}$

Table 10.6:

The mass ratio m_H/m_n is the parameter for the chemical bond as it is used in the one-phonon model, where Hydrogen is bound to Carbon. The loss coefficient $\eta(\sigma_{ieH})$ is the contribution of the inelastic scattering from Hydrogen to the loss; N_H is the density of Hydrogen atoms.

This estimation indicates that in the DLC Al-foil with lower density the Hydrogen is more losely bound to the Carbon atoms.

To summarize, in our experiment β constrains the possible amount of Hydrogen to a relatively small range, the loss parameter could only be tuned in the same model for different samples by changing the strength of the chemical bond. Qualitatively it seems that the strength of the chemical bonds of Hydrogen in the bulk material is related to the sp^3 ratio of the DLC layer. Furthermore, that with increasing density more Hydrogen is near the surface and therefore depolarization becomes higher.

In a recent review, Korobkina et al. [36] employs two different models, our model and a model using larger clusters of ice. In their case (losses on Copper), the latter model gives better agreement. However, also on a rather speculative level.

Chapter 11

Conclusion

An apparatus for the measurement of the loss- and depolarization probability per wall collision of ultracold neutrons (UCN) in a wide temperature range was built and measurements have been performed. The UCN storage properties of diamond-like Carbon (DLC) were measured for the first time and could be directly compared to Beryllium. The main conclusions from this work are:

- The measurement of the losses of UCN on DLC coatings was performed for the first time. It turned out, that DLC coated foils are a very promising new material for experiments with UCN. The loss coefficient η of a DLC coated polyethylene-foil was found to be $(7\pm1)\cdot 10^{-5}$ per wall collision at 70 K, without any surface treatment before the measurements. This is a factor of 2 worse than the best reported values for Beryllium, which had to undergo long treatment at high temperatures before. In the direct comparison at room temperature the loss probabilities of DLC were less than Beryllium by a factor of 2.6.

  The observed temperature dependence of η indicates a contamination with Hydrogen of a different amount for different samples.

- The value for the depolarization is $\beta = 0.8 \cdot 10^{-6}$ per wall collision for the DLC Al-foil, whereas all other samples showed depolarization at the level of $\beta = 1 \cdot 10^{-5}$ per wall collision, which agrees with literature. The measurement of the depolarization probabilities of different surfaces showed no energy dependence on our level of accuracy. Also no temperature dependence could be observed.

- It was for the first time possible to measure both parameters, loss- and depolarization probability, simultaneously. The ratio of the temperature dependent part of η to β gives credit to the assumption that Hydrogen is responsible for the observed effects. The simultaneous measurement of β allows for estimating the Hydrogen content. The measured results for DLC on PET and Al could be explained consistently in a simple one-phonon Debye model. However, the parameters concerning the Hydrogen content and the strength of the chemical bond to Carbon are quite different for the different samples. The reason for this behaviour is yet unknown.

- The Monte Carlo package used for the simulation of the experiment is included into GEANT4, which is a widely used and standard code in particle physics. The major physics concerning UCN are already implemented. Combined with the physics processes that are implemented in the standard GEANT4 release, the simulation of a wide range of experiments is possible, which makes the code very versatile. The code is being included in the simulation of the neutron EDM experiment at PSI and will be further developed and maintained there.

- The technique of using coated foils from the Fraunhofer IWS as storage volumes for UCN allows for a range of new experiments in this field. In a first large application the walls of the storage volume of the new PSI UCN source will be made of DLC coated stainless steel foils. In ongoing work at PSI the coatings are being further investigated [106].

The apparatus will be used for the investigation of DLC surfaces produced at PSI in the near future. Included in this project is also the measurement of Oxygen layers on the surfaces [107]. The limiting velocity of Oxygen of 85 neV fits nicely to the field barrier of 90 neV. In the anti-ferromagnetic α-phase below 24 K [108], also interesting information concerning depolarization are expected.

Bibliography

[1] Ya. B. Zel'dovich, Sov. Phys.-JETP **9**, 1389 (1959).

[2] V. I. Lushikov, Yu. N. Pokotilovski, A. V. Strelkov, F. L. Shapiro, JETP Letters **9**, 23 (1969).

[3] L. V. Groshev, N. V. Dvoretsky, A. M. Demidov, Yu. N. Panin et al., Phys. Lett. B **34**, 293 (1971).

[4] F. L. Shapiro, Sov. Phys. Usp. **11**, 345 (1968).

[5] R. Golub, J. M. Pendlebury, Contemp. Phys. **13**, 519 (1972).

[6] W. Mampe, P. Ageron, J. C. Bates et al., Nucl. Instr. Meth. A **284**, 111 (1989).

[7] J. D. Jackson, Phys. Rev. **106**, 517 (1957).

[8] J. H. Christensen, J. W. Cronin, V. L. Fitch, R. Turlay, Phys. Rev. Lett. **13**, 138 (1964).

[9] I. B. Khriplovich, S. K. Lamoreaux, CP Violation Without Strangness, Springer-Verlag Berlin Heidelberg (1997).

[10] N. F. Ramsey, Rep. Prog. Phys. **45**, 95 (1982).

[11] E. M. Purcell, N. F. Ramsey, Phys. Rev. **78**, 807 (1950).

[12] I. S. Altarev, Yu. V. Borisov, N. V. Borovikova, A. B. Brandin et al., JETP Letters **44**, 460 (1986).

[13] P. G. Harris, C. A. Baker,K. Green, P. Iaydjiev et al., Phys. Rev. Lett. **82**, 904 (1999).

[14] N. F. Ramsey, Molecular Beams, Oxford University, New York (1956).

[15] I. B. Kriplovich, S. K. Lamoreaux, CP Violation without Strangeness, Springer, (1997).

[16] F. Atchison, K. Bodek, B. Van Den Brandt, M. Daum et al., http://ucn.web.psi.ch/ (2000).

[17] G. Ban, K. Bodek, T. Brys, M. Daum et al., http://nedm.web.psi.ch/ (2005).

[18] R. Golub, D. J. Richardson, S. K. Lamoreaux, Ultra-Cold Neutrons, Adam Hilger (1991).

[19] A. Serebrov, V. Mityukhlyaev, A. Zakharov, A. Karitonov et al., Nucl. Instr. Meth. A **440**, 658 (2000).

[20] C. L. Morris, J. M. Anaya, T. J. Bowles, B. W. Filippone et al., Phys. Rev. Lett. **89**, 272501 (2002).

[21] A. Saunders, J. M. Anaya, T. J. Bowles, B. W. Filippone et al., Phys. Lett. B **593**, 55 (2004).

[22] F. Atchison, B. van den Brandt, T. Brys, M. Daum et al., Phys. Rev. C (accepted), (2005).

[23] F. Atchison, B. van den Brandt, T. Brys, M. Daum et al., Phys. Rev. Lett. (accepted), (2005).

[24] K. Bodek, B. van den Brandt, T. Brys, M. Daum et al., Nucl. Instr. Meth. A **533**, 491 (2004).

[25] K. Kopitzki, Einfuehrung in die Festkörperphysik, Teubner, (2002).

[26] A. Steyerl, B. Yerozolimsky, A. P. Serebrov et al., Euro. Phys. J. B **28**, 299 (2002).

[27] Yu. Pokotilovski, Nucl. Instr. Meth. A **425**, 320 (1999).

[28] R. Golub, J. M. Pendlebury, Rep. Prog. Phys. **42**, 439 (1979).

[29] A. Steyerl, Springer Tracts in Modern Pyhsics **80**, 57 (1977).

[30] V. K. Ignatovich, The Physics of Ultracold Neutrons, Clarendon Press Oxford (1990).

[31] P. Ageron, W. Mampe, A. I. Kilvington, Z. Physik B **59**, 261 (1985).

[32] A. D. Stoika, A. V. Strelkov, M. Hetzelt, Z. Physik B **29**, 349 (1978).

[33] Yu. Yu. Kosvinstev, I. V. Morozov, G. I. Terekhov, JETP Letters **9**, 424 (1982).

[34] W. A. Lanford, R. Golub, Phys. Rev. Lett. **39, 24**, 1509 (1977).

[35] K. Kawabata, M. Utsuro, S. Hayashi, Nucl. Instr. Meth. B **30**, 557 (1988).

[36] E. Korobkina, R. Golub, J. Butterworth, P. Geltenbort et al., Phys. Rev. B **70**, 35409 (2004).

[37] V. P. Alfimenkov et al., JETP Letters **55**, 84 (1992).

[38] V. V. Nesvizhevsky, E. V. Lychagin, A. Yu. Muzychka, G. V. Nekhaev et al., Phys. Lett. B **479**, 353 (2000).

[39] A. P. Serebrov, J. Butterworth, M. Daum, A. K. Fomin et al., Phys. Lett. A **309**, 218 (2003).

[40] E. V. Lychagin, D. G. Kartashof, A. Yu. Muzychka, V. V. Nesvishevsky et al., Phys. At. Nucl. **65,11**, 1995 (2002).

[41] V. V. Nesvishevsky, Phys. At. Nucl. **65,3**, 400 (2002).

[42] Yu. Pokotilovski, JETP Letters **76**, 3 (2002).

[43] T. Brys, M. Daum, P. Fierlinger, M. Gupta et al., PSI Scientific Report , 146 (2004).

[44] M. Makela, M. Pitt, R. B. Vogelaar, J. Yuan et al., Bull. Am. Phys. Soc. **47**, 98 (2002).

[45] C.-Y. Liu, U. Pesavento, J. Yuan, P. Geltenbort et al., Bull. Am. Phys. Soc. **47**, 98 (2002).

[46] M. G. D. Van der Grinten, J. M. Pendlebury, D. Shiers, C. A. Baker et al., Nucl. Instr. Meth. A **423**, 421 (1999).

[47] S. Heule, PhD Thesis, in preparation, (2005).

[48] V. F. Sears, Neutron Optics, Oxford University Press (1989).

[49] S. W. Lovesey, Theory of Neutron Scattering from Condensed Matter, Oxford University Press (1984).

[50] I. I. Gurevich, Low-Energy Neutron Physics, North-Holland Publishing Company, (1968).

[51] E. Segre (editor), Enrico Fermi, Collected Papers, University of Chicago Press, Chicago, IL (1962).

[52] L. Van Hove, Phys. Rev. **95**, 249 (1954).

[53] CODATA recommended values, http://physics.nist.gov/cuu/Constants/value?mn, (2002).

[54] F. Bloch, Phys. Rev. **70**, 460 (1946).

[55] G. Badurek, Physik polarisierter Neutronen, Habilitation Thesis, TU Wien (1983).

[56] D. Tabor, Cambridge University Press (1991).

[57] S. Agostinelli, J. Allison, K. Amako et al. , Nucl. Instr. Meth. A **506**, 250 (2003).

[58] F. Atchison, T. Brys, M. Daum, P. Fierlinger et al., submitted to Nucl. Instr. Meth. A, (2004).

[59] J.D. Jackson, Classical Electrodynamics, John Wiley and Sons, Inc., New York, London, Sydney (1962).

[60] W. H. Press, S. A. Teukolsky, W. T. Vetterling, B. P. Flannery, Numerical Recipies in C++ - The Art of Scientific Computing, Cambridge University Press (2002).

[61] P. A. Seeger, L. L. Daemen, Nucl. Instr. Meth. A **457**, 338 (2001).

[62] Yu. Yu. Kosvintsev et al., Nucl. Instr. Meth. A **143**, 33 (1977).

[63] M. Daum, P. Fierlinger, P. Geltenbort, M. Gupta et al., ILL Proposal 314-158, (2002).

[64] T. Brys, M. Daum, P. Fierlinger, M. Gupta et al., submitted to Nucl. Instr. Meth. A (2005).

[65] P. Ageron, Nucl. Instr. Meth. A **284**, 197 (1989).

[66] A. Steyerl, H. Nagel, F.-X. Schreiber, R. Gähler et al., Phys. Lett. A **116**, 347 (1986).

[67] V. Vrankovich, Private Communication, (2004).

[68] R. F. Holsinger, K. Halbach, Poisson Superfish 7.12, (2004).

[69] M. Negrazus, Private Communication, (2004).

[70] T. Brys, Private communication (2004).

[71] T. Brys, M. Daum, P. Fierlinger, M. Gupta et al., PSI report **1**, 146 (2004).

[72] S. Heule, Private communication (2005).

[73] V. V. Vladimirskii, JETP Letters **12**, 740 (1960).

[74] Yu. G. Abov et al., JETP Letters **44**, 369 (1986).

[75] Yu. Y. Kosvintsev, JETP Letters **22**, 70 (1978).

[76] E. Majorana, Nuovo Cim. **9**, 43 (1932).

[77] S. Eidelman et al. (Particle Data Group), Phys. Lett. B **592**, 1 (2004).

[78] T. Brys, M. Daum, P. Fierlinger, M. Gupta et al., submitted to Phys. Lett. B, (2005).

[79] I. Altarev, Private communication (2005).

[80] Ph. R. Bevington, Data Reduction and Error Analysis for the Physical Sciences, McGraw-Hill, NY, (1969).

[81] Particle Data Group, (2004).

[82] A. P. Serebrov, J. Butterworth, M. Daum, A. K. Fomin et al., Phys. Lett. A **309**, 218 (2003).

[83] V. V. Nesvizhevsky et al., Pis'ma Zh. Eksp. Teor. Fiz. **70**, 175 (1999).

[84] D. Kleppner, H. M. Goldberg, N. F. Ramsey, Phys. Rev. **126**, 603 (1962).

[85] L. D. Shaerer, G. K. Walters, Phys. Rev. A **139**, 1398 (1965).

[86] A. C. Zemach, R. J. Glauber, Phys. Rev. **101**, 118 (1956).

[87] Bound coherent neutron scattering lengths, http://www.ati.ac.at/neutropt/ ScatteringLengthAdvTable.pdf (2005).

[88] Neutron scattering lengths and cross sections, http://www.ncnr.nist.gov/resources/nlength/ (2005).

[89] V. K. Ignatovich, Private communication (2004).

[90] M. Wutz, H. Adam, W. Walcher, Handbuch Vakuumtechnik, Vieweg (1997).

[91] J. P. Bugeat, W. Mampe, Z. Physik B **35**, 273 (1979).

[92] E. Korobkina, Private communication (2005).

[93] T. Brys, M. Daum, P. Fierlinger, A. Fomin, submitted to Nucl. Instr. Meth. A, (2004).

[94] H. Schulz, Private communication (2004).

[95] L. Bondarenko, S. Chrnyavsky, A. Fomin, P. Geltenbort, Physika B **234**, 1189 (1997).

[96] S. Arzumanov, L. Bondarenko, S. Chernyavsky, A. Fomin, ISINN-6 Proceedings , 96 (1998).

[97] V. K. Ignatovich, Eur. Phys. J. B **8**, 1 (1998).

[98] S. L. Kanashenko, A. E. Gorodetsky, V. N. Chernikov, A. V. Markin et al., J. Nucl. Mat. **233**, 1207 (1996).

[99] P. Willich, Fraunhofer Institut Braunschweig, Private communication (2005).

[100] A. Serebrov, M. Lasakov, A. Vasiliev et al., Phys. Lett. A **313**, 373 (2003).

[101] A. Serebrov, A. Vasiliev, M. Lasakov et al., Nucl. Instr. Meth. A **440**, 717 (2000).

[102] M. Makela, PhD Thesis (draft), unpublished, (2005).

[103] V. F. Turchin, Slow Neutrons, Israel Program for Scientific Translations, (1965).

[104] A. Sjoelander, Arkiv Fysik **14**, 315 (1958).

[105] Y. Shirasu, Sh. Yamanaka, M. Miyake, J. Nucl. Mat. **179**, 223 (1991).

[106] B. Blau, T. Brys, M. Daum, P. Fierlinger et al., PSI report **1**, 147 (2004).

[107] R. Henneck, PSI research proposal, Ultracold Neutron losses measured for DLC, Be and solid Oxygen coatings, PSI-1-065, (2004).

[108] G. C. DeFotis, Phys. Rev. B **23**, 4714 (1981).